

**COMPUTATIONAL MODELLING STUDIES OF PtAs₂, PtAsS and
Pd₂As MINERAL SURFACES**

By

NEMUTUDI BRADLEY

RESEARCH DISSERTATION

MASTER OF SCIENCE

in

PHYSICS

in the

FACULTY OF SCIENCE AND AGRICULTURE

(School of Physical and Mineral Sciences)

at the

UNIVERSITY OF LIMPOPO

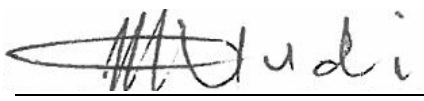
SUPERVISOR: Prof. P.E. Ngoepe

CO-SUPERVISOR: Dr. P.P. Mkhonto

2020

Declaration

I declare that the dissertation “computational modelling studies of PtAs₂, PtAsS and Pd₂As mineral surfaces” hereby submitted to the University of Limpopo, for the degree of Master of Science in Physics has not previously been submitted by me for a degree at this or any other university; that it is my work in design and in execution, and that all material contained herein has been duly acknowledged.



Nemutudi B. (Mr)

26/09/2020

Date

Dedication

This work is dedicated to my beloved family, my parents: Cyril Nemutudi and Constance Nemutudi. My sister Thelma Nemutudi. Lastly, my brothers Lennox and Bruce Nemutudi.

Acknowledgements

Above all I would like to express my sincere gratitude to the almighty God for all the strength and knowledge he has deposited in me during all the years of my studies.

I would like to acknowledge my supervisor Professor P.E. Ngoepe for the guidance during the research. In addition, I would like to thank with great appreciation the guidance, discussion and assistance in the preparation of this work by my co-supervisor Dr P.P. Mkhonto.

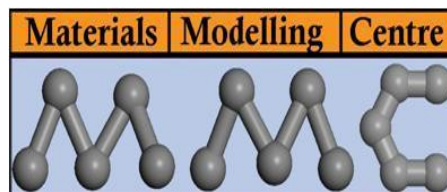
I am grateful to the National Research Foundation (NRF) for the financial support offered for this Master of Science in Physics degree research.

The Centre for High Performance Computing (CHPC) is acknowledged for the provision of computer resources. The whole community of the University of Limpopo for the role played towards education equipment and studying environment. I would like to thank my fellow colleagues in the Materials Modelling Centre (MMC) for their good working relationship during this research.

My heartily gratitude with great appreciation is directed to my family, my father and mother Cyril and Constance, my brothers Lennox and Bruce and my sister Thelma. Thank you for your love, support and encouragement throughout my studies.

Lastly, to all my friends thank you for the support.

My Family



Abstract

Sperrylite (PtAs_2), platarsite (PtAsS) and palladoarsenide (Pd_2As) are platinum group minerals (PGMs) predominantly found in the Platreef Bushveld Complex in South Africa, which is one of the leading countries with highest percentages of platinum group minerals. In this study the density functional theory (DFT), embodied in the Vienna *Ab-initio* Simulation Package (VASP) code, was employed to investigate the structural, thermodynamically, elastic, mechanical, vibrational, electronic and surface properties of cubic PtAs_2 and PtAsS , and monoclinic Pd_2As mineral structures. The PtAsS was investigated from both virtual crystal approximations (VCA) solid solution within the Cambridge Serial Total Energy Package (CASTEP) code and the VASP cluster expansion (CE) approach. The cluster expansion phase stability was employed to generate new stable system of PtAsS model and from the cluster expansion binary ground state diagram we found a greater stability at 50/50 percentage ($x = 0.5$) of PtAsS where As and S atoms were equally distributed with formation of S-As dimer bond at the centre. The calculated lattice parameters were well reproduced and agreed with the available experimental data. The binary ground state diagram also showed that all structures have negative heats of formation (ΔH_f), hence they were thermodynamically stable (miscible constituents). The calculated heats of formation predicted that PtAs_2 was more stable than the PtAsS and the order of stability for cubic structures decreased as: $\text{PtAs}_2 > \text{PtAsS (VCA)} > \text{PtAsS (CE)}$.

The elastic constants indicated mechanically stability for all structures and the phonon dispersion curves showed no soft modes for PtAs_2 , PtAsS (CE) and Pd_2As , suggesting stability. Moreover, the elastic instability (negative C_{ij}) was observed in the PtAsS (VCA) structure. We also observed that the Pd_2As and PtAsS (CE) were ductile, while PtAs_2 and PtAsS (VCA) were brittle. The calculated Young modulus indicated that PtAs_2 was much stiffer compared to PtAsS models. This suggested that PtAs_2 was mechanically stronger among all the cubic structures. The PtAs_2 was a dominant covalently bonded compound whereas PtAsS and Pd_2As were predicted as ionic bonded.

The computed Bader charges for the bulk and surface PtAs_2 , PtAsS (CE) and Pd_2As and Mulliken atomic charges for PtAsS (VCA) showed different behaviour. The Pt and Pd species showed negative charges, while As species showed a positive charge for PtAs_2 and Pd_2As . The PtAsS (CE) showed a negative charge for Pt and S species, while the PtAsS (VCA) showed a negative and a positive charges for Pt and As/S species. The calculated total density of states

(TDOS) for the bulk PtAsS and Pd₂As showed a metallic behaviour since there was no band gap at the Fermi energy (E_F). The PtAs₂ model was observed as a semiconductor with a band gap of 0.104 eV. From the DOS, PtAs₂ was found the most stable since it had less contribution of DOS at the E_F , while PtAsS and Pd₂As structures showed least stability due to highest DOS at the E_F .

The understanding of the aspects of surface stability and preferred surface cleavage were investigated starting from surface terminations and then slab thickness for (100), (110) and (111) surfaces of all mineral structures. We found that (100) surface was the most stable, displaying the lowest positive surface energy for all the PtAs₂, PtAsS and Pd₂As minerals and was considered as the working surface. The order of surface stability decreased as: (100) > (111) > (110) for PtAs₂ and PtAsS (VCA and CE) mineral systems and (100) > (110) > (111) for Pd₂As system. Interestingly we found that the surface energies of the PtAsS (VCA) were smaller than for PtAsS (CE), which indicated that the VCA was more stable than the CE. The (100) surface was the most dominant on the surface morphology as expressed by the morphologies for all the mineral structures. Analysis of the DOS of the most stable (100) surface for PtAs₂, PtAsS and Pd₂As, we found that sperrylite and palladoarsenide showed a metallic behaviour since there was no band gap observed at the E_F , while PtAsS surface structures showed a semiconductor behaviour due to presence of band gaps of 0.142 eV and 0.551 eV for PtAsS (CE) and PtAsS (VCA), respectively. The PtAsS (VCA) was found the most stable, while Pd₂As was found the least stable. In addition, the intermediate stability was found for PtAsS (CE) and PtAs₂ surface structures. These findings gave more insights on the stability of these minerals which may be applicable to their recovery.

Table of contents

CHAPTER 1	1
1. Introduction.....	1
1.1 General background	1
1.2 Literature review	2
1.2.1 Flotation process.....	3
1.3 Structural properties	6
1.3.1 Sperrylite (PtAs ₂).....	6
1.3.2 Platarsite (PtAsS).....	7
1.3.3 Palladoarsenide (Pd ₂ As)	8
1.4 Rationale, Aim and Objectives.....	8
1.4.1 Rationale.....	8
1.4.2 Aim and Objectives	9
1.5 Outline of the dissertation	10
CHAPTER 2	12
2. Methodology.....	12
2.1 Density functional theory (DFT).....	12
2.1.1 Local density approximation	14
2.1.2 Generalized gradient approximations	15
2.1.3 Projector augmented wave method.....	16
2.2 Plane-wave pseudo potential method.....	16
2.2.1 Plane-wave basis.....	16
2.2.2 Pseudopotential method.....	18
2.2.3 Ultrasoft Pseudopotential	20
2.3 K-points sampling	21
2.4 Virtual crystal approximation approach.....	22
2.4.1 Ramer and Rapper VCA approach	23
2.4.2 Bellaiche and Vanderbilt VCA approach	23
2.5 UNiversal CLuster-Expansion	23
2.5.1 Miscible constituents	24
2.5.2 Miscibility gap.....	24
2.6 Plane-wave pseudo potential codes.....	24
2.6.1 VASP implementation.....	25
2.6.2 CASTEP implementation	25

2.9 Theoretical background of calculated properties	26
2.9.1 Heats of formation	26
2.9.2 Elasticity	27
2.9.2.1 Definition of elastic constants	28
2.9.2.2 Calculations of elastic constants	29
2.9.2.3 Elastic constant stability conditions	29
2.9.3 Phonon dispersion curves	32
2.9.4 Density of states.....	33
2.10 Charge population analysis	34
2.11 Cleaving of surfaces	35
CHAPTER 3	39
3. Structural, thermodynamic, mechanical and vibrational properties of PtAs ₂ , PtAsS and Pd ₂ As bulk structures.....	39
3.1 Cluster expansion approach and binary ground state diagram of Pt-As-S model.....	39
3.2 Virtual crystal approximation approach PtAsS bulk model.....	42
3.3 Convergence of the cut-off energy and k-points sampling	43
3.3.1 Cut-off energy variations.....	43
3.3.2 k-points sampling	44
3.4 Structural and thermodynamics properties.....	45
3.4.1 Bulk structure optimization	45
3.4.2 Heats of formation	47
3.5 Elastic properties	48
3.6 Vibrational properties of PtAs ₂ , PtAsS and Pd ₂ As structures.....	51
3.7 Summary	54
CHAPTER 4	56
4. Surface modelling of PtAs ₂ , PtAsS and Pd ₂ As.....	56
4.1 Surface k-point convergence.....	56
4.2 Surface computational methods	57
4.3 Sperrylite (PtAs ₂)	58
4.3.1 Surface terminations	58
4.3.2 Slab thickness determination	59
4.3.3 Analysis of the working surfaces.....	62
4.4 Platarsite (PtAsS) cluster expansion	63
4.4.1 Surface terminations	63
4.4.2 Slab thickness determination	65

4.4.3 Analysis of the working surfaces.....	67
4.5 Platarsite (PtAsS) VCA.....	67
4.5.1 Surface terminations	67
4.5.2 Slab thickness determination	68
4.5.3 Analysis of the working surfaces.....	70
4.6 Determination of working surfaces for platarsite (PtAsS).....	71
4.7 Palladoarsenide (Pd ₂ As).....	71
4.7.1 Surface terminations	71
4.7.2 Slab thickness determination	73
4.7.3 Analysis of the working surfaces.....	76
4.8 Surface morphologies of PtAs ₂ , PtAsS and Pd ₂ As surface structures	77
4.9 Electronic structures of the bulk and clean (100) surface for PtAs ₂ , PtAsS and Pd ₂ As systems	78
4.9.1 Total density of states for PtAs ₂ , PtAsS and Pd ₂ As structures.....	78
4.9.2 Density of states and Bader analysis	79
4.10 Summary	86
CHAPTER 5	87
Summary and conclusions	87
Recommendation and future work.....	89
Appendix A: Explanation data of the project	102
Appendix B: Tables	103
Appendix C: Papers presented at conferences	108

List of figures

Figure 1.1: Schematic diagram of flotation cell [26].	5
Figure 1.2: The crystal structure of sperrylite (PtAs ₂).	7
Figure 1.3: The crystal structures: (a) platarsite (CE) and (b) platarsite (VCA).	7
Figure 1.4: The crystal structure of palladoarsenide (Pd ₂ As) mineral.	8
Figure 2.1: Schematic illustration of a wave in the coulomb all-electron potential of the nucleus (blue dashes lines) and the pseudopotential (red solid lines). The pseudo-wave function, the real and the potentials match the radius r_c above [44].	18
Figure 2.2: A simplified representation of the surface cleavage methodology for PtAs ₂ .	36
Figure 2.3: Representation of the different types of surfaces.	37
Figure 3.1: The cluster expansion binary ground state diagram obtained in determining the lowest ground states of Pt-As-S system.	40
Figure 3.2: Cluster expansion approach on sperrylite with addition of sulphur atom at the same position of arsenic atom: (a) representing PtAs ₂ model, (b) sulphur atom and (c) representing PtAsS model.	40
Figure 3.3: Virtual crystal approximation approach showing: (a) sperrylite bulk model and (b) PtAsS (VCA) model.	42
Figure 3.4: Total energy against kinetic energy cut-off: (a) cubic PtAs ₂ , (b) cubic PtAsS (CE), (c) cubic PtAsS (VCA) and (d) monoclinic Pd ₂ As structures.	43
Figure 3.5: Total energy against k-points mesh: (a) cubic PtAs ₂ , (b) cubic PtAsS (CE), (c) cubic PtAsS (VCA) and (d) monoclinic Pd ₂ As structures.	44
Figure 3.6: The relaxed bulk structures: (a) PtAs ₂ , (b) PtAsS (CE), (c) PtAsS (VCA) and (d) Pd ₂ As models.	46
Figure 3.7: (a) Phonon dispersion for PtAs ₂ , (b) phonon partial density of states for platinum contribution and (c) arsenic contribution. Pt and As contributions towards the vibrations along x, y and z components, respectively.	52
Figure 3.8: (a) Phonon dispersion for PtAsS (CE), (b) phonon partial density of states for platinum contribution, (c) arsenic contribution and (d) sulphur contribution. Pt, As and S contributions towards the vibrations along x, y and z components, respectively.	53

Figure 3.9: (a) Phonon dispersion for Pd₂As, (b) phonon partial density of states for palladium contribution and (c) arsenic contribution. Pd and As contributions towards the vibration along x, y and z components, respectively.53

Figure 4.1: Total energy against k-points mesh (a) cubic PtAs₂ and PtAsS surfaces (b) monoclinic Pd₂As surface structures.56

Figure 4.2: Shows 11 different surface terminations along the three low MI planes (100), (110) and (111) for PtAs₂.58

Figure 4.3: Slab depth vs total energy plot for PtAs₂. (a) The most stable (100), (b) the least stable (110) and (c) the (111) the moderate stable surfaces..... 60

Figure 4.4: The un-relaxed structures of surface layers convergence for PtAs₂ along the low MI plane (100), (110) and (111).61

Figure 4.5: The un-relaxed and relaxed supercell structures of surface layers convergence for PtAs₂, (a) (100), (b) (110) and (c) (111) surface.....62

Figure 4.6: Top-view (left) and side view (Right) of the top three layers (3L) on 2x2 supercell working surface of (100) sperrylite surface. Showing raised As ridges and Pt atoms inhabiting the clefts between ridges (Right), with the resulting bond distances (Left).63

Figure 4.7: Shows 11 different surface terminations along the three low MI planes (100), (110) and (111) for PtAsS (CE) structure.....64

Figure 4.8: Slab depth vs total energy plot for PtAsS (CE). The most stable (100), (b) the least stable (110) and (c) the moderate stable (111) surfaces.66

Figure 4.9: The un-relaxed and relaxed supercell structures of surface layers convergence for PtAsS (CE), (a) (100), (b) (110) and (c) (111) surface.66

Figure 4.10: Top-view (left) and side view (Right) of the top three layers (3L) on 2x2 supercell working surface of (100) PtAsS (CE) surface. Showing raised As and S ridges and Pt atoms inhabiting the clefts between ridges (Right), with the resulting bond distances (Left).67

Figure 4.11: Slab depth vs total energy plot for PtAsS (VCA). (a) The most stable (100), (b) the least stable (110) and (c) the moderate stable (111) surfaces.68

Figure 4.12: The un-relaxed and relaxed supercell structures of surface layers convergence for PtAsS (VCA), (a) (100), (b) (110) and (c) (111) surface.....69

Figure 4.13: Top-view (left) and side view (Right) of the top three layers (3L) on 2x2 supercell working surface of (100) PtAsS (VCA) surface. Showing raised As/S ridges and Pt atoms inhabiting the clefts between ridges (Right), with the resulting bond distances (Left).70

Figure 4.14: Shows 18 different surface terminations along the three low MI planes (100), (110) and (111) for Pd ₂ As model.	72
Figure 4.15: Shows surface terminations Type 1 and Type 2 along (100) and (110) surfaces for Pd ₂ As model.....	73
Figure 4.16: The un-relaxed structures of surface layers convergence for Pd ₂ As along the low MI plane (100), (110) and (111).	74
Figure 4.17: Slab depth vs total energy plot for Pd ₂ As. (a) The most stable (100), (b) the moderate stable (110) and (c) the least stable (111) surfaces.	74
Figure 4.18: The un-relaxed and relaxed supercell structures of surface layers convergence for Pd ₂ As, (a) (100), (b) (111) and (c) (110) surface.....	75
Figure 4.19: Top-view (left) and side view (Right) of the top three layers (3L) on 2x2 supercell working surface of (100) palladoarsenide surface. Showing raised As ridges and Pd atoms inhabiting the clefts between ridges (Right), with the resulting bond distances (Left).	77
Figure 4.20: The calculated equilibrium surface morphologies: (a) PtAs ₂ , (b) PtAsS (CE), (c) PtAsS (VCA) and (d) Pd ₂ As surface structures.....	78
Figure 4.21: Comparison of the total density of states for PtAs ₂ , PtAsS and Pd ₂ As structures.	79
Figure 4.22: TDOS and PDOS of the bulk structure and top most platinum and arsenic atoms: (a) Bulk PtAs ₂ and (b) PtAs ₂ (100) surface.	80
Figure 4.23: TDOS and PDOS of the bulk structure and top most platinum, arsenic and sulphur atoms on (a) PtAsS (CE) and (b) PtAsS (CE) (100) surface.	81
Figure 4.24: TDOS and PDOS of the bulk structure and top most platinum, arsenic and sulphur atoms on (a) PtAsS (VCA) and (b) PtAsS (VCA) (100) surface.....	82
Figure 4.25: TDOS and PDOS of the bulk structure and top most palladium and arsenic atoms on (a) Pd ₂ As and (b) Pd ₂ As (100) surface.	83

List of tables

Table 3.1: The progress of iterative procedure listing stable structures consisting of many pure phases.....	41
Table 3.2: The thermodynamic stable structures that summarizes the ground state line.	42
Table 3.3: The equilibrium calculated and experimental lattice parameters and cell volumes for PtAs ₂ , PtAsS (CE), PtAsS (VCA) and Pd ₂ As structures.	47
Table 3.4: The calculated heats of formation (ΔH_f) for PtAs ₂ , PtAsS (CE), PtAsS (VCA) and Pd ₂ As structures.	48
Table 3.5: The elastic constants, bulk modulus (B), tetragonal shear modulus (C'), isotropic shear modulus (G), Young's modulus (E), anisotropic factor (A), Poisson's ratio (ν), bulk to shear modulus (B/G) and Cauchy pressure ($C_{12} - C_{44}$) of PtAs ₂ , PtAsS (CE) and PtAsS (VCA) structures.	49
Table 3.6: The calculated elastic constants C_{ij} (in GPa) of Pd ₂ As monoclinic structure.	49
Table 3.7: Summarized the bulk (B), shear (G) and Young's modulus (E), Poisson's ratio (ν), Cauchy pressure ($C_{12} - C_{44}$) and the shear anisotropic factors (A_1 , A_2 and A_3) of the monoclinic Pd ₂ As.....	50
Table 4.1: Different terminations, number of atoms, number of layers, total energy and surface energy for (100), (111) and (110) PtAs ₂ surfaces.	59
Table 4.2: Surface layers convergence of (100), (111), and (110) surface slab, number of atoms per slab, total energy (eV) and surface energies (J/m ²) for PtAs ₂	60
Table 4.3: Supercell optimization of (100), (111), and (110) surface layers convergence, number of atoms per slab, total energy (eV) and surface energies (J/m ²) for PtAs ₂ system. ..	61
Table 4.4: Different terminations, number of atoms, number of layers, total energy and surface energy for (100), (111) and (110) surfaces for the structure PtAsS (CE).....	64
Table 4.5: Surface layers convergence of (100), (111) and (110) surface, number of atoms per slab, total energy (eV) and surface energies (J/m ²) for PtAsS (CE) structure.	65
Table 4.6: Supercell optimization of (100), (111), and (110) surface layers convergence, number of atoms per slab, total energy (eV) and surface energies (J/m ²) for PtAsS (CE).....	66
Table 4.7: Different terminations, number of atoms, number of layers, total energy and surface energy for (100), (111) and (110) surfaces for PtAsS (VCA).	68
Table 4.8: Surface layers convergence of (100), (111) and (110) surfaces, number of atoms per slab, total energy (eV) and surface energies (J/m ²) for PtAsS (VCA) mineral.....	69

Table 4.9: Supercell optimization of (100), (111), and (110) surface layers convergence, number of atoms per slab, total energy (eV) and surface energies (J/m ²) for PtAsS (VCA) mineral.	70
Table 4.10: Bulk and surface coordination, supercell optimization of (100), (111) and (110) surfaces showing number of atoms per slab and surface energies (J/m ²) for PtAsS systems.	71
Table 4.11: Different terminations, number of atoms, number of layers, total energy and surface energy for (100), (111) and (110) surfaces for Pd ₂ As.	72
Table 4.12: Surface layer convergence of (100), (111) and (110) surfaces, number of atoms per slab, total energy (eV) and surface energies (J/m ²) for Pd ₂ As system.	75
Table 4.13: Supercell optimization of (100), (111) and (110) surface layers convergence, number of atoms per slab, total energy (eV) and surface energies (J/m ²) for Pd ₂ As system.	76
Table 4.14: Bulk and surface coordination, supercell optimization of (100) surface showing number of atoms per slab and surface energies (J/m ²) for Pd ₂ As system.	77
Table 4.15: The calculated Bader analyses for the bulk and relaxed (100) surface of PtAs ₂ , PtAsS (CE) and Pd ₂ As.	84
Table B1.1: The atomic positions (Wyckoff notation) in sperrylite (PtAs ₂) crystal structure [66].	103
Table B1.2: The atomic positions (Wyckoff notation) in platarsite (PtAsS) CE structure [66].	104
Table B1.3: The atomic positions (Wyckoff notation) in platarsite (PtAsS) VCA structure [66].	105
Table B1.4: The atomic positions (Wyckoff notation) in palladoarsenide (Pd ₂ As) crystal structure [66].	106
Table B1.5: The ground state enthalpies of formation as derived by DFT and CE in eV/atom at the final iteration for Pt-As-S system.	107

List of Abbreviations

PGEs	Platinum Group Elements
PGMs	Platinum Group Minerals
BMS	Base Metal Sulphides
VCA	Virtual Crystal Approximation
DFT	Density Functional Theory
GGA	Generalised Gradient Approximations
GGA-PW91	Generalised Gradient Approximations Perdew-Wang (1991)
GGA-PBE	Generalised Gradient Approximations Perdew-Burke-Ernzerhof
LSDA	Local Spin Density Approximation
LDA	Local Density Approximation
H-K	Hohenberg-Kohn
K-S	Kohn-Sham
VASP	Vienna <i>Ab-initio</i> Simulation Package
CASTEP	Cambridge Serial Total Energy Package
PAW	Project Augmented Wave
PW	Plane-Wave
WDA	Weighted Density Approximation
MD	Molecular Dynamics
UNCLE	UNiversal CLuster Expansion
CE	Cluster Expansion
SCC	Self-Consistent Redistribution of Charges
DOS	Density of States
TDOS	Total Density of States

PDOS	Partial Density of States
PPDOS	Phonon Partial Density of States
VB	Valence Band
CB	Conduction Band
E_F	Fermi Energy
eV	Electron Volte
Å	Angstrom
MI	Miller Index
OH ⁻	Hydroxide
H ₂ O	Water
LO	Longitudinal Optical
TO	Transverse Optical
LA	Longitudinal Acoustic
TA	Transverse Acoustic
Pt	Platinum
Pd	Palladium
As	Arsenic
S	Sulphur

CHAPTER 1

1. Introduction

In this dissertation, we reported the structural, elastic, mechanical, vibrational, electronic and surface properties of sperrylite (PtAs_2), platarsite (PtAsS) and palladoarsenide (Pd_2As) structures. In this introductory chapter, we review briefly from literature the previous theoretical and experimental studies and related methods that were used to study the platinum group minerals (PGM). Furthermore, the flotation process necessary for minerals separation were discussed. The structural properties of the sperrylite (PtAs_2), platarsite (PtAsS) and palladoarsenide (Pd_2As) minerals were reviewed, the rationale and objectives of this study were stated and finally, the outline of the study was given.

1.1 General background

The mineralogy of the ore and their stability plays an important role in understanding the floatability of the minerals. Platinum is usually found in different mineralogy and this is dependent on the geological area. There are two main minerals (sulphides and arsenides) that usually host the valuable minerals such as platinum (Pt) and palladium (Pd). The sulphide minerals have been found amiable to flotation, while the arsenides were indicated as hard to float, thus there is a need to find better way to float the arsenide minerals in order to increase their recovery. The greatest challenges associated with mineral processing industry are separating the valuable platinum group minerals (PGMs) from the worthless rock or other material (gangue ore) [1]. Majority of the world's supply of platinum and palladium are within the four layered igneous intrusion such as Bushveld complex in South Africa, the Stillwater complex in USA, the Great Dyke in Zimbabwe and the Noril'sk-Talnakh complex in Russia [2]. In South Africa most PGMs are mined in Mogalakwena mine and Ivanplants Platreef mine in Mokopane of Limpopo province. The sperrylite, platarsite and palladoarsenide are mostly found in the Platreef Bushveld complex in South Africa, which is one of the leading countries with highest percentage of PGMs [2]. More than 75% of platinum and 35% of palladium in the world are produced in South Africa and they have originated in the ore bodies [3]. The primary platinum ores are mined from Merensky reef, Upper Group 2 (UG2) reef and Platreef [4], with

the Platreef containing the most complex ores, while the UG2 is complex due to the chromite in the reef. The platinum industry is challenging because Pt is extremely rare in the earth's crust and the average value of PGMs deposits tend to be clustered at around an average of 75 percent in the world's, with the largest reserves in the Bushveld region of South Africa with the concentration of PGEs reaching as high as 1-2 ppm [5]. The PGMs are extracted from ores but, because of their high value, they are also recovered from industrial residues of variable composition. Most interestingly, the development of new technology for the extraction, recovery and separation of the PGMs is therefore of special interest.

The PGMs are the most important source of platinum and palladium [6], with platinum extremely resistant to physical and chemical degradation and has exceptional catalytic properties. These properties have led to extensive utilization of jewellery, high temperature industrial and automobile markets. The PGEs are present as discrete in PGMs attached to the sulphides and arsenides or in solid solution [7]. In addition, the sulphur and arsenide mixed system platarsite as one of the platinum bearing mineral, possesses properties that makes it relevant in the extraction of platinum and is of great importance to the mining industry [8]. The platarsite mineral is associated with other sulphide minerals and valuable metals such as copper, silver and gold. Most importantly, the reactions that occur at the surfaces of PtAsS mineral play an important role in the release of S, As and Pt during oxidation.

1.2 Literature review

The oxidation of minerals is important in order to understand their behaviour during flotation; in particular platarsite which is easily oxidized at a low pH, similar to arsenopyrite [9]. The oxidation begins by physisorption of oxygen on the mineral surfaces forming a complex and the chemisorption forming peroxides. This process has been previously reported to depress sulphide minerals [10]. Furthermore, it has been indicated that the atmospheric oxidation of minerals either by weathering or aging involves physical and chemical adsorption of oxygen on the surface and this forms various peroxides and hydroxides [11]. As such, oxidation of PGMs, in particular arsenides minerals surface is of outstanding practical importance and requires theoretical fundamental understanding of surface chemistry during mineral flotation.

PGMs are found in conjunction with a large number of base metal sulphides (BMS), including pentlandite $(\text{Fe,Ni})_9\text{S}_8$ [12], which has been found to contain up to 12.1 wt % of Pd [13]. The complex mineralogy of PGMs and their various associations makes broad spectrum

recovery of PGMs challenging. The sperrylite is the most common PGM, which tends to be poorly recovered by flotation process. The adsorption of collectors can be promoted by low to moderate levels of oxidation. Previous studies have laid foundation in understanding the flotation behaviour of arsenides minerals [14].

Control of the chemistry occurring within the flotation process can allow enhanced recovery of a particular mineral over others. This is achieved by the addition of collector ligands, which are small organic molecules that adsorb preferentially on the surfaces of targeted minerals and modulate their surface hydrophobicity by presenting a chain aliphatic tail into solution, which in turn promotes mineral attachment to air bubble and improves recovery [1]. The OH⁻ and H₂O molecules are studied as they are both present in the flotation system at elevated pH as surface adsorption competitors for collector ligands.

Although there is limited work on the PGMs recovery from computational methods, a similar structure of pyrite (FeS₂) has been extensively investigated. This has been used to test a wide range of collectors that could be possibly used for the PGMs. Previously Hung et al. investigated the pyrite structure and laid a foundation on the surface cleavage and terminations of pyrite surfaces [15, 16]. Then later the adsorption of xanthate collectors were investigated on pyrite surface and gave useful findings on collector adsorption [15]. Later on Chen et al. also investigated the comparison adsorption of xanthate, dithiophosphate and dithiocarbamate on pyrite and galena [17]. Waterson et al. used computational method to investigate the binding dithio ligands on sperrylite, pentlandite and platinum surfaces [1]. These investigation have shown that computational methods offer an effect tool to investigate collector adsorptions on mineral surfaces and design of collectors with less amount of time.

In this study a computational simulation method was used to study the stability configurations of a bulk PtAs₂, PtAsS and Pd₂As and their surfaces. These will mainly be determined from structural, thermodynamic, elastic, mechanical, vibrational, electronic and surface stability (surface energies) of PtAs₂, PtAsS and Pd₂As.

1.2.1 Flotation process

The flotation of arsenides minerals ore remains a challenge due to the arsenides being hard to float, while those of sulphides are amiable to flotation. This is due to the formation of platinum and palladium hydroxide on the surfaces which create a barrier for collector attachment during flotation. Wang *et al.* reported, that platinum arsenides and sulphides are associated with pentlandite [18]. Froth flotation is one of the processes used to separate

valuable minerals from the gangue waste materials. This is a physicochemical process designed to separate one or more finely ground mineral particles from a complex mixture according to their wettability. It is widely used in industry to separate higher value minerals from the vast excess of gangue minerals [19, 20]. It has been reported that the hydrophobic character of a variety of base-metal sulphides were examined in the presence of ligands such as potassium ethyl xanthate [21]. It was also used in the PGM mining applied to the raw mineral ore feed after crushing and grinding processes. The flotation method is used in several processing industries and historically this was firstly used in the mining industries [22, 23]. This method is one of the most versatile and flexible of all mineral separation processes due to the fact that reasonable outcomes are fairly easy to obtain. However, the flotation processes are complex and thus a better understanding of these processes may lead to higher yields and less damage to the environment. An outstanding performance is achieved by a frequent monitoring of the process and the understanding of the mineral ore. Some of the variables that affect the operation and control of a flotation process are chemical components such as collectors, frothers, activators, depressants and pH modifiers together with the operation components such as mineralogy, particle size, pulp density and temperature [24].

Firstly, the chemical components affecting the flotation process are collectors. The collectors are small organic molecules designed to adsorb on the surface of the targeted minerals. They create a hydrophobic mineral and promote their attachment to the air bubbles. Collectors can be considered in terms of ionic and non-ionic. Ionic collectors are weak acids, bases and salts consisting of a charged head group attached to a hydrocarbon with short chain. The charged head group adsorbs on the target mineral surface and presents the hydrophobic tail into solution. Non-ionic collectors contain molecules with head groups that are uncharged. The second chemical component are the frothers. These are compound which stabilizes in the dispersion of the air bubbles in the mixture of flotation [19] and helps in the formation of a stable surface froth. The other chemical component includes the modifiers such as pH control agents, activators and depressants. Modifiers are used to modify the chemistry of flotation pulp which do not collect minerals or support the froth phases. The pH control agents are used to maintain the optimum pH window for the particular flotation application under use. The range of pH for most flotation applications is between pH 7-11 because of instability of many species at lower pH. The second modifiers are activators which enhances the ability of a collector to adsorb onto a mineral surface. Lastly, the depressants, this attaches to the unwanted material and renders them hydrophilic and thus depresses to the tailings.

For froth flotation to be carried out, a number of steps have to be performed. Firstly, the grinding of the ore to fine enough material so that valuable mineral particles become liberated from the waste rock and the size range suitable to be floated are between 10 - 200 microns. Secondly, mixing the grinded ore with water to create a slurry, however; the ratio of water to solids is very important [25]. Thirdly, the conditions must be made favourable for the desired mineral particles to adhere to air bubbles; this is done by stage-adding of collectors. The collector should attach through its polar sulphur atoms to only valuable mineral particles so that water is repelled and air bubbles can become attached upon collision [24]. Lastly, a rising current must be created, this is done by blowing air into the flotation cell which creates air bubbles that acts like 'hot-air balloons' providing the necessary buoyancy to carry selected minerals to the pulp surface [24]. After all these results in formation of a mineralized froth on the surface of the ore pulp which is skimmed off from the flotation cell or vessel. A typical flotation cell and the processes that occur in it are presented in Figure 1.1.

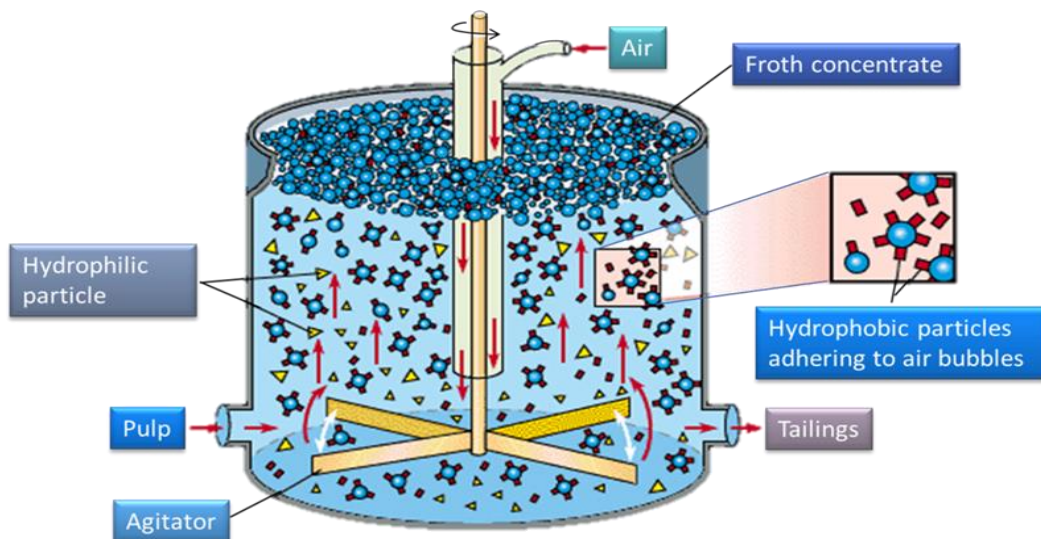


Figure 1.1: Schematic diagram of flotation cell [26].

The polar (ionic) sulphur atoms on the non-polar (hydrophobic) hydrocarbon thiol collector interact with the metals on the surface; surrounding the metals in a vertical orientation with the tails of the collectors being hydrophobic. This causes the mineral to adhere to the air bubble which causes the mineral to move to the pulp surface [25]. In order to understand the physical and chemical properties of the platinum and palladium mineral surfaces, it is necessary to know the properties of the bulk material; the former is merely a breach of the translational symmetry of the latter.

1.3 Structural properties

Generally, a mineral is a solid, naturally occurring inorganic substances with a defined crystal structure which has been formed as a results of a geological processes [27]. In addition, a mineral species is defined mainly on the basis of its chemical composition and crystallographic properties. If a mineral is found with composition or crystallographic properties different from any existing mineral species, a possibility is that it may be a new mineral species [28]. Platinum is the most abundant element constituting the PGMs, mainly in the sulphides and arsenides minerals. Furthermore, palladium is known to be the succeeding most dominant PGE [29]. In the next section we give a brief discussion on platinum group minerals namely, sperrylite, platarsite and palladoarsenide in terms of their crystal system.

1.3.1 Sperrylite (PtAs_2)

Sperrylite (PtAs_2) crystallizes in the isometric system with the pyrite-type group structure. Interestingly, PtAs_2 is the most common Pt bearing mineral in the world [13]. Sperrylite possess a space group of Pa-3 (#205) with lattice parameter of $a = 5.967 \text{ \AA}$ [30]. Since PtAs_2 , FeS_2 and CoAsS have the same total number of valence electrons per formula unit, one would expect the formation of a semiconductor gap in PtAs_2 as it was observed in FeS_2 and CoAsS minerals [31]. PtAs_2 is commonly associated with base metal sulphides minerals, which are believed to have crystallized from magmatic sulphide melts [32]. Those includes pyrrhotite, pentlandite and chalcopyrite. However, sperrylite is thought to have formed by crystallization from a sulphide melt or by exsolution from sulphide minerals. Furthermore, the sperrylite is also formed by crystallization from silicate magma, where it is associated with oxide and silicate minerals [32].

There is only one kind of metal atom in the PtAs_2 structure, that is Pt atom, which occupies four octahedral sites M(O) within the arsenic framework [33]. Note that the parameters in Table B1.1 of the appendix B are for the un-relaxed PtAs_2 structure. Sperrylite is formed by contact metamorphism and the grains are mostly anhedral but few euhedral grains could be encountered [34]. The grains are surrounded by later veins of pyrite. The bulk structure of PtAs_2 consist of 12 atoms. The As1 forming a dimer are 4-coordinated and As2 which are linked arsenic are 3-coordinated (Figure 1.2).

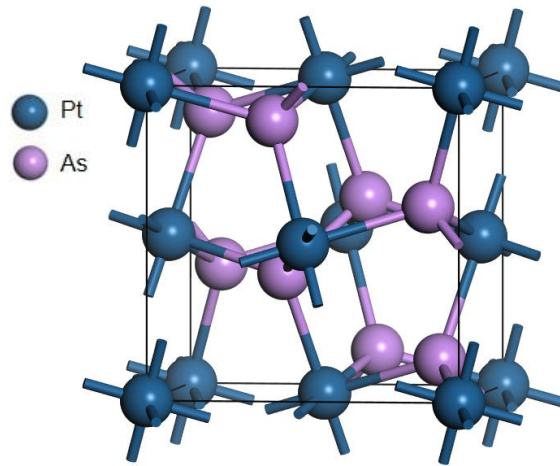


Figure 1.2: The crystal structure of sperrylite (PtAs_2).

1.3.2 Platarsite (PtAsS)

Platarsite (PtAsS) is an isometric diploidal gray mineral and is metallic. The mineral exist in nature and it is studied in different types of structures, the binary phase being the stable PtAsS as solid solution ($\text{PtAs}_{2-x}\text{S}_x$ where $x = 0-1\%$) which requires that arsenides and sulphurs occupies the same lattice position in the structure and the other phase of PtAsS is random atom configuration where As and S are evenly distributed in the crystal structure lattice. The crystal structure of PtAsS is also cubic with a space group of Pa-3 (#205) with lattice parameters $a = 5.428 \text{ \AA}$ [35], a hardness of 7.5 and a specific gravity of 8.0. For PtAsS mineral structure, there is also one kind of metal atom (Pt), which occupies one octahedral site M(O) and the tetrahedral site M(T) is occupied by the sulphur and arsenic atoms [33] as shown in Table B1.2 and B1.3 of the appendix B.

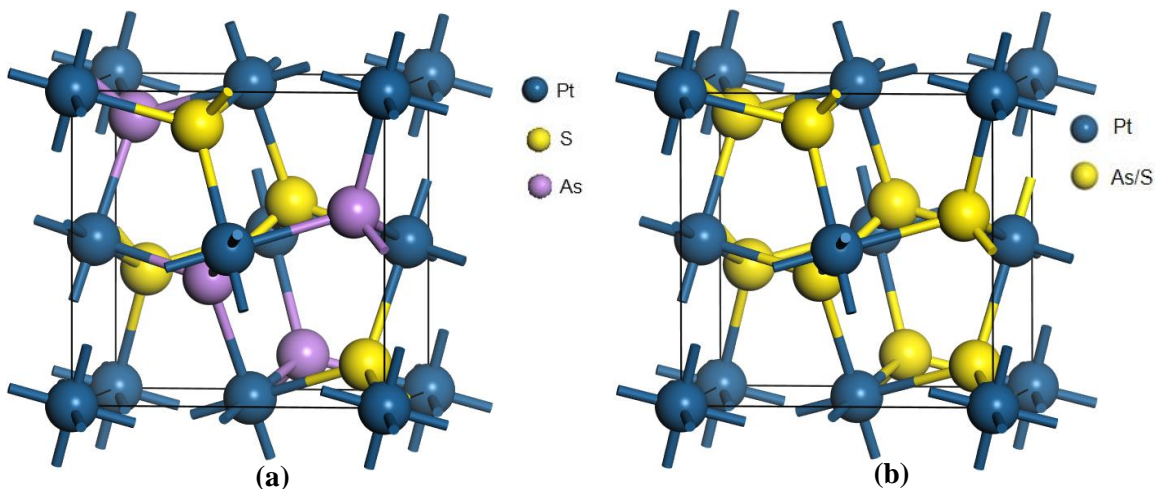


Figure 1.3: The crystal structures: (a) platarsite (CE) and (b) platarsite (VCA).

The As1 and S1 that forms a dimer are 4-coordinated and linked arsenic and sulphur are 3-coordinated as shown in Figure 1.3. The bulk structure of PtAsS (CE and VCA) consist of 12 atoms. The crystal structures of platarsite (CE and VCA) are shown above in Figure 1.3.

1.3.3 Palladoarsenide (Pd₂As)

Palladoarsenide (Pd₂As) is a monoclinic structure which usually in association occurs with chalcopyrite and occurs in the form of long, veinlet-like vermiform and irregular deposits [36]. The crystal structure of Pd₂As has been refined in a space group of P-62m (#189) [37], where $a = b = 6.650 \text{ \AA}$ and $c = 3.583 \text{ \AA}$. Refer to Table B1.4 of the appendix B, there are two kinds of metal atoms in the structure, which occupy three octahedral site M(O), and three of the tetrahedral sites M(T), within the arsenic framework [33]. The M(O) are coordinated to the face-capping arsenic, while the M(T) are coordinated to the linked and face-capping arsenic. The As(f) are 8-coordinated while the As(l) are 2-coordinated. Table B1.4 of the appendix B shows the un-relaxed parameters of Pd₂As mineral.

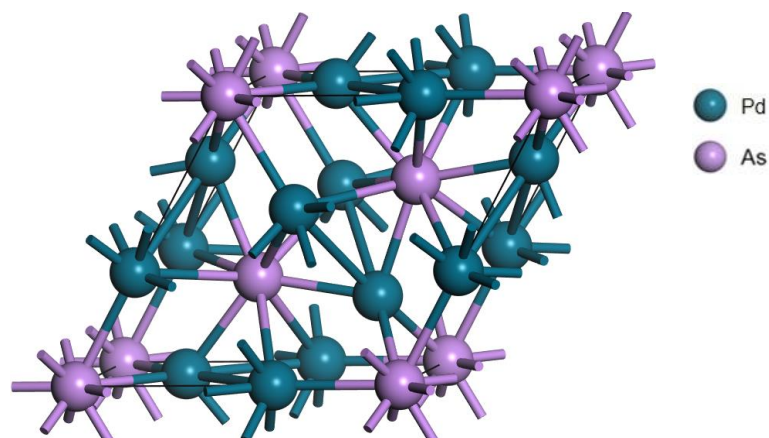


Figure 1.4: The crystal structure of palladoarsenide (Pd₂As) mineral.

1.4 Rationale, Aim and Objectives

1.4.1 Rationale

The project focused on the platinum group minerals, namely the sperrylite (PtAs₂), platarsite (PtAsS) and palladoarsenide (Pd₂As). The PGMs are predominantly found in the Platreef Bushveld Complex, and the most common are Pt and Pd which are found in the form of PtAs₂,

PtAsS and Pd₂As minerals. The stability from solid solution approach and cluster expansion approach for the PtAsS system were investigated using computational DFT method.

The recent computational approaches and algorithms that have been developed provide alternative means to investigate the complex mineral surfaces at low cost and efficiency. These methods allow for investigation of flotation processes such as hydroxide adsorption, hydration and interaction of collectors on surfaces which are limited in literature computationally. The experimental techniques can be costly and presents a number of challenges in securing the desired reagents and running a large number of time-consuming and expensive tests. However, computational modelling is an attractive option to screen potential collector molecules using minimal time and resources prior to beginning full laboratory testing. Hence the study will generate structural, thermodynamic, elastic, mechanical, vibrational, electronic and surface stability of PtAs₂, PtAsS and Pd₂As.

We introduce cluster system and cluster expansion formalism by reviewing applications of cluster expansion in computational material science. The stability will be conducted through heats of formation, elastic constants, phonon dispersion curves and density of states. In addition, an approach to surface calculations that includes generalized surface terminations, surface slab construction and surface energy convergence with respect to slab thickness were investigated. Along with describing slab creation and convergence, supercell calculations were reviewed and discussed. The surface properties will be investigated which will give better reactive properties of these mineral surfaces and to better understand the surface reaction for flotation and extraction that experiments might not easily accomplish. The PtAsS compound will be obtained through transformation from PtAs₂ to solid solution approach and cluster expansion approach. The surface stability was investigated from the surface energies on different surface slab and termination. These are significant to distinguish the preference of surface cleavage for possible maximum recovery.

1.4.2 Aim and Objectives

The aim of the study is to investigate the stability of PtAs₂, PtAsS and Pd₂As minerals and their surfaces.

The objectives of the study are to:

- i. determine the suitable cut-off energy and k-point mesh parameters for sperrylite, platarsite and palladoarsenide minerals,

- ii. perform the full geometry optimisation of the bulk and surface structures,
- iii. investigate the solid solution structure using virtual crystal approximation (VCA), on $\text{PtAs}_{2-x}\text{S}_x$ where $x = 0 - 1.0\%$,
- iv. generate new stable system using cluster expansion for PtAsS ,
- v. determine the PtAs_2 , PtAsS and Pd_2As bulk structures stability from: lattice constants, heats of formation, elastic constants, phonon dispersions and density of states,
- vi. cleave the low index surfaces at different terminations and vary slab thickness,
- vii. determine the most stable surface termination that is less reactive from surface energy (working surface),
- viii. calculate electronic properties for the stable surfaces (working surface).

1.5 Outline of the dissertation

The dissertation gives the study of the structural, thermodynamic, elastic, mechanical, vibrational, electronic and surface properties of sperrylite (PtAs_2), platarsite (PtAsS) and palladoarsenide (Pd_2As) minerals, using *ab-initio* DFT method. In addition, the PtAsS cluster expansion was investigated for generation of new stable PtAsS system. The dissertation is divided into six chapters:

Chapter 1 presented the general background based on the theory. The literature review, flotation process, the structural properties, rationale, the aim and objectives of this work are stated.

Chapter 2 deals with the methods that have been used in the current study: DFT, plane-wave (PW) and projector-augmented-wave (PAW) pseudopotential methods, Vienna *Ab-initio* Simulation Package (VASP) code and Cambridge Serial Total Energy Package (CASTEP) code. Firstly, the chapter introduces various first principle techniques. Secondly, the DFT for calculating geometry optimization is described. Thirdly, approximation method such as LDA and GGA are described. Fourthly, the UNiversal CLuster Expansion (UNCLE), the plane-wave pseudopotential codes, VASP and CASTEP, surface preparations and energy calculations are presented. Lastly, theoretical background of calculated properties: heats of formation, elasticity, phonon dispersion curves and density of states. In addition, the charge population analysis and the cleaving of different surface terminations are described.

Chapter 3 is concerned with the discussion of the results of the bulk PtAs₂, PtAsS and Pd₂As systems. Firstly, cut-off energy and the number of k-points (convergence test) and then computational method details used. Secondly, the cluster expansion simulation using UNCLE code and structural properties (lattice parameters) and thermodynamic properties (heats of formation). Thirdly, elastic and mechanical properties (elastic constants and modulus. Lastly, the vibrational properties (phonon dispersions).

Chapter 4 is concerned with the discussion of the surface modelling. Firstly, construction of the PtAs₂, PtAsS and Pd₂As mineral surface and surface k-point convergence. Secondly, surface computational method details and cleaving of the (100), (110) and (111) low Miller index planes and relaxations of different surface terminations are discussed. Thirdly, slab thickness determination and various layers are analysed and the analysis of working surfaces are discussed. Lastly, electronic properties (density of states) and the Bader charges are discussed.

Chapter 5 gives the summary and conclusion.

Lastly the bibliography which helps give insight to the analysis of the work is listed and papers presented in conferences are given in Appendices.

CHAPTER 2

2. Methodology

This chapter gives details of the methods of calculations employed in this study. Computational simulations investigate different structural, elastic, mechanical, vibrational, electronic and surface properties of materials theoretically. The approach has been used in solid state physics, chemistry and materials science, to predict the real situation by presenting physical systems as models of different systems. All calculations will be carried out using first principle quantum mechanical density functional theory (DFT) [38] to study structural, elastic, mechanical, vibrational, electronic and surface properties and model the structures of PtAs₂, PtAsS (CE and VCA) and Pd₂As. The theory solves Schrödinger equation and applies the plane-wave (PW) and projector-augmented-wave (PAW) pseudopotential methods. The plane-wave and projector augmented wave pseudopotentials are necessary for performing full geometry optimisation of the structures.

In the next section we discuss the quantum mechanical DFT for describing the many-body problem by approximation methods.

2.1 Density functional theory (DFT)

Density functional theory (DFT) is a computational quantum mechanical modelling method used to investigate the electronic structure of many-body systems, in particular atoms, molecules and condensed phases [39]. DFT can also be an approach for describing the ground state properties of metals, semiconductors, and insulators. DFT has become the most commonly used method of calculating accurately the physical properties of vast range materials. Within the DFT, the properties of a many electron system can be determined using functional, i.e. function of another function, which in this case is the spatially dependent electron density. These theory has been very popular for calculations since the 1970s [40]. It is used for calculations in solid state physics.

Although DFT has its theoretical backgrounds in the Thomas-Fermi model, the theoretical basis were confirmed by the two Hohenberg-Kohn (H-K) theorems [41]. The first H-K theorem demonstrates that the ground state properties of a many-electron system are uniquely determined by an electron density that depends on only three spatial coordinates. This gives

the possibility for reducing the many-body problem of N electrons with $3N$ spatial coordinates to 3 spatial coordinates, through the use of functionals of the electron density. This theorem can be extended to the time-independent domain to develop time-dependent density functional theory, which can be used to describe excited states [41]. The first Hohenberg-Kohn theorem demonstrates that the density of any system determines all ground-state properties of the system, that is:

$$E = E[\rho], \quad 2.1$$

where E is the ground state energy and ρ is the ground-state density of the system.

The second H-K theorem shows that there exists a variational principle for the above energy density functional $E[\rho]$. If ρ' is not the ground state density of the above system, then:

$$E[\rho'] > E[\rho], \quad 2.2$$

The second H-K theorem defines energy functional for the system and proves that the correct ground-state electron density minimizes this energy functional. Within the framework of Kohn-Sham (K-S) DFT, the intractable many-body problem of interacting electrons in static potentials is reduced to a tractable problem of non-interacting electrons moving in an effective potential [42]. The effective potential includes the external potential and the effects of the Coulomb interactions between the electrons, that is the exchange and correlation interactions. Modelling the latter two interactions is impossible within K-S DFT. The LDA is based upon exact energy for a uniform electron gas, which can be obtained from the Thomas-Fermi model, and from fits to the correlation energy for a uniform electron gas. Non-interacting systems are relatively easy to solve as the wave function can be represented as a Slater determinant of orbitals [43].

The Kohn-Sham total energy functional for a set of doubly occupied electronic states can be written as:

$$E = \sum_i \int \left(\frac{\hbar^2}{2m} \nabla^2 \psi_i \right) d^3r + \int V_{\text{ion}}(\mathbf{r}) n(\mathbf{r}) d^3r + \frac{e^2}{2} \int \frac{n(\mathbf{r})n(\mathbf{r}')}{|\mathbf{r}-\mathbf{r}'|} d^3r d^3r' + E_{\text{xc}}[n(\mathbf{r})] + E_{\text{ion}}(\{\mathbf{R}_I\}), \quad 2.3$$

and E_{ion} is the Coulomb energy associated with interactions among the ions at positions $\{\mathbf{R}_I\}$, V_{ion} is the static total electron-ion potential, $\rho(\mathbf{r})$ is the electronic density given by:

$$\rho(\mathbf{r}) = 2 \sum_i |\psi_i(\mathbf{r})|^2, \quad 2.4$$

where $E_{XC}[n(\mathbf{r})]$ is the exchange-correlation functional. It is necessary to determine the set of wave functions ψ_i that minimizes the Kohn-Sham energy functional. These are given by the self-consistent solutions to the Kohn-Sham equations:

$$\left[\frac{-\hbar}{2m} \nabla^2 + V_{\text{ion}}(\mathbf{r}) + V_{\text{H}}(\mathbf{r}) + V_{\text{xc}}(\mathbf{r}) \right] \psi_i(\mathbf{r}) = \varepsilon_i \psi_i(\mathbf{r}), \quad 2.5$$

and ψ_i is the wave function of electronic state i , ε_i is the Kohn-Sham Eigen value and V_{H} is the Hartree potential of the electrons [44]. The exchange-correlation as a function of the electron spin (up and down) density $n(\mathbf{r})$ must be approximated within K-S DFT [41]. The ground state energy of the system can be written as:

$$E_0 = \min_{\rho} \rightarrow N (F[\rho] + \int \rho(\vec{r}) V_{\text{Ne}} d\vec{r}), \quad 2.6$$

where $F[\rho]$ is the universal function that contains the contributions of the kinetic energy, classical coulomb interaction and non-classical portion:

$$F[\rho] = T[\rho] + J[\rho] + E_{\text{nc}}[\rho] \quad 2.7$$

$J[\rho]$ is known, then the expressions $T[\rho]$ and $E_{\text{nc}}[\rho]$ has to be found. Thomas-Fermi model provides an example of density functional theory. Then its performance is bad because of the poor approximation of kinetic energy. Kohn and Sham suggested to calculate the kinetic energy of the non-interacting system with the same density as the interacting [42] one using the equation below:

$$T_{\text{S}} = -\frac{1}{2} \langle \sum_i^N \psi_i | \nabla^2 | \psi_i \rangle \quad \text{and} \quad \rho_{\text{S}}(\vec{r}) = \sum_i^N \sum_s |\psi_i(\vec{r}, s)|^2 \rho(\vec{r}) \quad 2.8$$

Hence, ψ_i is the non-interacting orbitals of the system. T_{S} is not equal to the system of the true kinetic energy. According to Kohn and Sham, the separation of the functional $F[\rho]$ was introduced:

$$F[\rho] = T_{\text{S}}[\rho] + J[\rho] + E_{\text{xc}}[\rho], \quad 2.9$$

E_{xc} is the exchange correlation energy, which can be defined by,

$$E_{\text{xc}}[\rho] = (T[\rho] - T_{\text{S}}[\rho]) + (E_{\text{ee}}[\rho] + J[\rho]) \quad 2.10$$

2.1.1 Local density approximation

The local density approximation (LDA) is the basis of all approximate exchange-correlation functionals. The functional only depend on the local density at a given point, while the GGA depends on the local density and its gradient [45]. Within the LDA, electrons move on a

positive background charge distribution. The center of this model contain uniform electron gas. The LDA well describe the ground state properties (lattice constants and bulk moduli, etc.). The Hohenberg-Kohn theorem provides some motivation for using approximate methods to describe the exchange-correlation energy as a function of the electron density. LDA is the simplest exchange-correlation used for describing the energy of electronic system [44]. According to Dirac, the exchange functional was introduced to the slater exchange. The central idea of LDA is the assumption that we can write E_{XC} in the following form of:

$$E_{XC}^{LDA}[\rho] = \int \rho(\vec{r}) \varepsilon_{xc}(\rho(\vec{r})) d\vec{r} \quad 2.11$$

Hence, $\varepsilon_{xc}(\rho(\vec{r}))$ is the exchange-correlation energy per particle of a uniform electron gas of density $\rho(\vec{r})$ and the probability $\rho(\vec{r})$ weights with the energy per particle showing an electron at the position. The quantity $\varepsilon_{xc}(\rho(\vec{r}))$ can be further split into exchange and the contributions of correlations:

$$\varepsilon_{xc}(\rho(\vec{r})) = \varepsilon_x(\rho(\vec{r})) + \varepsilon_c(\rho(\vec{r})) \quad 2.12$$

The local density approximation is a first-principle approach in the sense that the quantum mechanical problem is solved without any arbitrary or system dependent parameters [46]. The LDA assumes that the exchange-correlation energy functional is purely local.

2.1.2 Generalized gradient approximations

The GGA Modify K-S energy partitioning to obtain a non-local Hamiltonian but it is still local [47]. The first logic step to go the LDA is by supplementing the density with the gradient of charge density information, $\nabla \rho(\vec{r})$ to account for non-homogeneity of true electron density. Then the exchange-correlation energy termed generalized gradient approximation can be written as:

$$E_{XC}^{GGA}[\rho, \alpha, \rho, \beta] = \int f(\rho, \alpha, \rho, \beta, \nabla \rho, \alpha, \nabla \rho, \beta) d\vec{r} \quad 2.13$$

Hybrid functional was successfully introduced by Alex Becke in 1993 as to improve the results within the exchange functional GGA:

$$E_{XC}^{hyb} = \alpha E_X^{KS} + (1 - \alpha) E_{XC}^{GGA}, \quad 2.14$$

where E_X^{KS} is the exchange calculated with the wave function KS, E_{XC}^{GGA} is an appropriate GGA, and α is a fitting parameter [48]. The exchange-correlation energy for the generalized

gradient approximation improves upon the local spin density approximations (LSDA) description of solids and atoms. It improve total energies and structural energy differences and it expands and weakens the bonds [47]. The functions of GGA are accurate and give very good results for molecular geometries and ground-state energies and are expressed in terms of Perdew-Wang, they are potentially more accurate than the GGA functional and meta-GGA functions [49]. Hybrid Meta GGA, hybrid and double functional are other important DFT functionals. GGA-PBE is one of the important exchange-correlation functional for calculating solids [50].

2.1.3 Projector augmented wave method

This work employs the projector augmented wave (PAW) method within the framework of DFT as implemented in the CASTEP and VASP codes that has been shown to yield reliable results for the structural, electronic and surface properties of various solids. The PAW method is successful and has been used effectively; and in many ways functions like pseudopotentials. The method has a strong relationship with the ultrasoft pseudopotentials, but it also allows the full wave functions including the core electron wave functions to be calculated. In this method, the full wavefunctions are transformed onto auxiliary wavefunctions. The auxiliary functions can be expanded relatively easily in a plane wave basis, while the full wavefunctions are augmented with atomic wavefunctions. It assumes the frozen-core approximation but is significantly more transferable than pseudopotentials [44].

2.2 Plane-wave pseudo potential method

The plane-wave pseudopotential technique is a good method used to calculate with accuracy the variational self-consistent solution to the density functional theory. It is applicable in large systems that are subjected to 3D periodic boundary conditions. In this method the wave function is expanded in terms of plane-wave basis and giving a good pseudopotential representation of the ions in the crystal.

2.2.1 Plane-wave basis

The use of plane wave basis set offers a number of advantages, including the simplicity of the basis function in which there is no preconceptions considering the form of the solution, the absence of basis set superposition errors and the ability to efficiently calculate the forces on the atoms [51]. It requires the expansion of electronic wave function of the system. The plane-

wave pseudopotential method is a reliable tool to study the properties of material. A good description of a plane-wave basis method is by use of Bloch's theorem [52] which simply allows electronic wave functions to be expanded in terms of the plane wave. The expression of electronic wave functions for periodic solids and the problem such as atoms and surfaces according to Bloch's theorem can be as follows:

$$\psi_i(\mathbf{r}) = e^{i\mathbf{k}\cdot\mathbf{r}}F_i(\mathbf{r}) \quad 2.15$$

This allows us to expand the crystal wave functions in terms of plane waves $F_i(\mathbf{r})$, written as:

$$F_i(\mathbf{r}) = \sum_{\mathbf{G}} C_{i,\mathbf{G}} e^{i\mathbf{G}\cdot\mathbf{r}}, \quad 2.16$$

where \mathbf{G} is the reciprocal lattice vectors of the periodic cell. Then each electronic wave function can be written as follows:

$$\psi_{\mathbf{k}_i}(\mathbf{r}) = \sum_{\mathbf{G}} C_{i,\mathbf{K}+\mathbf{G}} e^{i(\mathbf{k}+\mathbf{g})\cdot\mathbf{r}}, \quad 2.17$$

where $C_{i,\mathbf{K}+\mathbf{G}}$ are the coefficients of plane waves and depend entirely on the specific kinetic energy,

$$\left(\frac{\hbar^2}{2m}\right)|\mathbf{K} + \mathbf{G}_c|^2. \quad 2.18$$

The parameter above controls the convergence of expansion by selecting the cut-off of the kinetic energy. The plane-wave basis set is restricted to a sphere in reciprocal space shown in terms of energy cut-off, E_{cut} and for all values of \mathbf{G} , the kinetic energies are less than or equal to a particular cut-off energy as follows:

$$\left(\frac{\hbar^2}{2m}\right)|\mathbf{K} + \mathbf{G}_c|^2 \leq E_{\text{cut}} \quad 2.19$$

Energy cut-off is chosen by increasing its magnitude until the total energy is converged to require accuracy [53]. When the plane wave number is increased, one can describe more rapidly varying features and an infinitely large number of basis set could simply be achieved. Finite bases set are obtained when finite cut-off energy is introduced to the discrete plane-wave basis set. To avoid errors in the computation of the total energy; cut-off energy should be increased until the calculated energy has converged. Denser set of \mathbf{k} -points must be used to reduce errors and ensure good convergence.

2.2.2 Pseudopotential method

The pseudopotential method is an effective potential method constructed to replace the atomic all-electron potential such that core states are eliminated and the valence electrons described by pseudo-wave function. The important feature of valence electron moving through a crystal including a relativistic effects are described weak pseudopotential that replace the electron core and the attractive coulomb potential inside the ionic core [54]. The pseudo-valence electron and the pseudo-ion cores replaces the original solid. The pseudo electron have a weaker potential inside the core region but experiences same potential outside the core region as the original electron. The ionic potential (Z/r), valence wave function (ψ_v), the corresponding pseudopotential V_{pseudo} and pseudo wave function (ψ_{pseudo}) are shown indicated in Figure 2.1 [44]. The utilization of the pseudopotential approximation method had an advantage, since it allows the electronic wave function to expand using a smaller number of a plane-wave basis states.

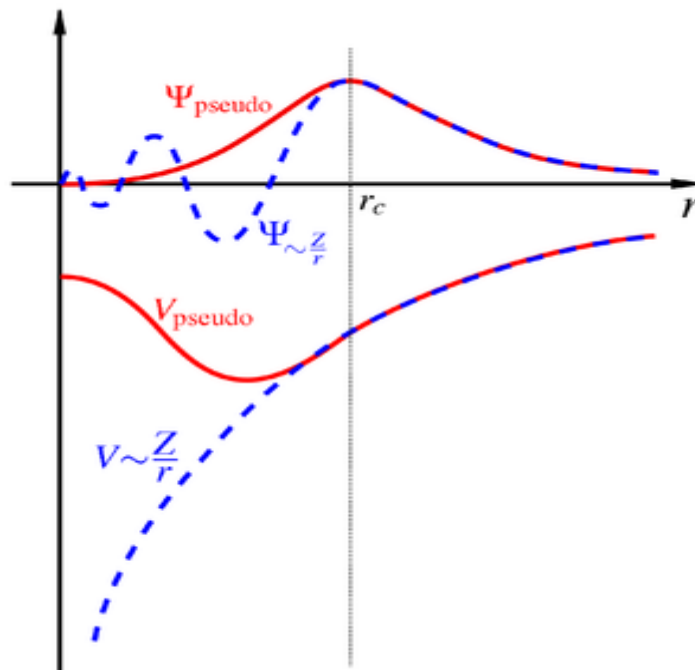


Figure 2.1: Schematic illustration of a wave in the coulomb all-electron potential of the nucleus (blue dashes lines) and the pseudopotential (red solid lines). The pseudo-wave function, the real and the potentials match the radius r_c above [44].

Although Bloch's theorem states that the electronic wave function can be expanded using a discrete set of plane waves, a plane-wave basis set is usually very poorly suited to expanding electronic wave functions because a very large number of plane waves are needed to expand the tightly bound core orbitals and to follow the rapid oscillations of the wave function and the

valence electrons in the core region. It is well known that most physical properties of solids are dependent on the valence electrons to a much greater extent than on the core electrons.

The pseudopotential approximations exploits this by removing the core electrons and by replacing them and the strong ionic potential by a weaker pseudopotential that acts on a set of pseudo wave functions. An ionic potential, valence wave function and the corresponding pseudopotential and pseudo wave function are illustrated schematically in Figure 2.1. The valence wave functions oscillate rapidly in the region occupied by the core electrons due to the strong ionic potential in this region. These oscillations maintain the orthogonality between the core wave functions and the valence wave functions, which is required by the exclusion principle. The pseudopotential is constructed ideally, so that its scattering properties or phase shifts for the pseudo wave functions are identical to the scattering properties of the ion and the core electrons for the valence wave functions, but in such a way that the pseudo wave functions have no radial nodes in the core region.

In the core region, the total phase shift produced by the ion and the core electrons will be greater by π , for each node that the valence functions had in the core region, than the phase shift produced by the ion and the valence electrons. Outside the core region, the two potentials are identical and the scattering from the two potentials is indistinguishable. The phase shift produced by the ion core is different for each angular momentum component of the valence wave function, and so the scattering from the pseudopotential must be angular momentum dependent.

The most general form of pseudopotential is:

$$V_{NL} = \sum_{lm} |lm\rangle V_i \langle lm| \quad 2.20$$

where $|lm\rangle$ and $\langle lm|$ are the spherical harmonics and V_i is the pseudopotential for angular momentum l , acting on the electronic wave function with this operator decomposes the wave function into spherical harmonics, each of which is then multiplied by the relevant pseudopotential V_i . Local pseudopotential uses the same potential for all the components of angular momentum.

The plane-wave calculation uses the ultrasoft pseudopotential introduced by Vanderbilt [55] and the norm-conserving pseudopotentials. The pseudo-wave functions are allowed to be soft within the core region in this scheme. In this report we use the ultrasoft pseudopotential (USP) for the total energy calculations with in the CASTEP code [56] and norm-conserving non-local pseudopotentials using VASP code [57].

The final building block in terms of plane wave basis sets is atomic pseudopotentials. However, chemical bonding occurs from the overlap of the outer valence electrons between atoms. Core electrons (those which are not actively involved in bonding) are chemically inert, however as they are electrons in their own right they require modelling. In fact, due to their relative proximity to the nucleus, core electrons are actually more expensive to model than valence electrons as their kinetic energies are much higher, and so they require a higher kinetic energy cut-off. The solution to this problem is to remove electrons altogether and replace them with a potential which stimulates their effect on the valence electrons. The pseudopotential must recreate an all-electron model beyond a particular cut-off distance (r_{cut} , the distance cut-off from the atomic core defining the core/valence divide), but within that radius the pseudopotential has smooth, continuous character in contrast to the rapidly oscillating character of an all-electron basis set. Similarly the periodic potential, V , (felt only by the core electrons within r_{cut}) experiences an exponential decay approaching the nucleus. This is costly to model and so is replaced by a smooth function. These concepts are depicted in Figure 2.1. This work makes an extensive use of ultrasoft pseudopotentials as proposed by Vanderbilt [55]. These pseudopotentials adopt a large value for r_{cut} , thus leaving fewer, lower energy electrons in the valence region to be modelled by plane waves which thus have the benefit of requiring a much lower kinetic energy cut-off than older (e.g. low r_{cut} norm-conserving pseudopotentials [58]). The one electron Schrodinger equation is replaced by pseudopotential equation as follows:

$$\frac{p^2}{2m} + V_{\text{pseudo}}(r) \psi_{\text{pseudo}}(r) = \epsilon \psi_{\text{pseudo}}(r), \quad 2.21$$

where $\psi_{\text{pseudo}}(r)$ is the pseudo wave function and $V_{\text{pseudo}}(r)$ is the exact pseudopotential as presented in Figure 2.1.

2.2.3 Ultrasoft Pseudopotential

Ultrasoft pseudopotential (USP) covers a wide range of atoms including the transition metals. In 1990, Vanderbilt developed a pseudopotential known as ultrasoft pseudopotential. Many of the modern pseudopotential calculations uses the generalisation of the Kleinman-Bylander [55]. The approach is a radical departure from norm-conserving pseudopotentials, since ultrasoft pseudopotential attain much smoother pseudo wavefunctions. In this approach, the pseudo wavefunctions are required to be equal to all electron wavefunctions outside the radius, as with the norm-conserving pseudopotentials, but inside the radius are allowed to be as soft as possible. Again the norm conserving constraint is removed, but this also introduces

some complications. However, the ultrasoft pseudopotential still be able to reduce the plane cut-off needed in calculations, particularly since large values of radius can be used in their scheme.

The complications that results are two-fold. First of all, since the pseudo wavefunctions are equal to all-electron wavefunctions (and have the same norm) in the interstitial, but have a different norm inside the topological complexity they are necessarily not normalised. Secondly, the pseudo charge density is not obtained by computing $\sum \varphi^* \varphi$ as with norm-conserving pseudopotential, this will lead to the incorrect total charge. A third, but less important complications is that, by relating the norm-conservation, the resulting pseudopotentials can become less transferrable. However, Vanderbilt pseudopotentials were proposed for use in large scale calculations, for which the costs of generating pseudopotentials is negligible as compared to the cost of the calculations [55]. The electron density is subdivided into a smooth part that extends throughout the unit cell and a hard part localised in the core region. The ultrasoft pseudopotential have advantage over the norm-conserving pseudopotential.

2.3 K-points sampling

Electronic states are allowed at asset of k-points determined by the boundary conditions that apply to the bulk solid. The density of allowed k-points is proportional to the volume of the solid. The infinite numbers of electrons in the solid are accounted for by an infinite number of k-points and only a finite number of electronic states are occupied at each k-point.

The Bloch theorem changes the problem of calculating an infinite number of electronic wavefunctions to one of calculating a finite number of k-points. The occupied states at each k-point contribute to the electronic potential in the bulk solid so that in principle an infinite number of calculations are needed to compute this potential. Furthermore, the electronic wavefunctions at k-points that are very close are identical. Hence it is possible to represent the electronic wavefunctions over a region of k space by the wavefunctions at a single k-point. In this case the electronic states at only a finite number of k-points are required to calculate the electronic potential and hence determine the total energy of the solid.

Methods have been devised for obtaining very accurate approximations to the electronic potential from a filled electronic band by calculating the electronic wavefunctions at special sets of k-points. The two most common methods are those of Chadi and Cohen [59] and Monkhorst and Pack [60]. Using these methods, the electronic potential and the total energy of an insulator can be obtained by calculating the electronic states at a very small number of k-

points. A denser set of k-points are required to calculate the electronic potential and the total energy of a metallic system in order to define the Fermi surface precisely.

However, the computational costs of performing a very dense sampling of k space increase linearly with the number of k-points in the Brillouin zone (BZ). Density functional codes approximate these k space integrals with a finite sampling of k-points. Special k-points schemes have been developed to use the fewest possible k-points for a given accuracy, thereby reducing the computational cost. The most commonly used scheme is that of Monkhorst and Pack [60].

2.4 Virtual crystal approximation approach

The virtual crystal approximation (VCA) approach is a tractable way of studying configurationally disordered systems and the potentials which represents atoms of two or more elements that are averaged into a composite atomic potential. In addition, this approach deals with disorder in first principle calculations implemented within CASTEP code. This approach has the advantage that a single configuration with smaller unit cell represents the disordered system. Due to the different local environment of the virtual atom, some properties may not be reproduced [61]. The material properties of solid-solutions and alloys have been widely studied in both computational and experimental approach. Specifically, ferroelectric ceramics correspond to a typical material class for which most of the realistic applications are implemented by solid solutions.

However, there exists two ways such as the supercell and virtual crystal approximation approach with regard to the advantages and shortcomings to treat such material systems within first principle methods. The former can give more correct results but requires much of computational resources compared with the latter. It is genuine that the effectiveness of the calculation is connected with the reality that the supercell may hold many unit cells compared with the primitive unit cell of the VCA method. In the year 2000, several modern VCA approaches were developed within their own advantages and shortcomings. Moreover, the main two issues are considered; capability of treating the heterovalent atoms and accuracy of the calculation. VCA method originated from tight binding methods by replacing atoms with effective atoms and choosing the parameterization to return alloy properties. The advantage is the simplicity but it is not sufficiently accurate in some cases.

2.4.1 Ramer and Rapper VCA approach

The reason of the incorrectness is mixing of only the potentials. Ramer and rapper developed more accurate VCA approaches through performing the averaging at the level of atomic calculation, where the averaging of eigenvalues of valence orbitals [61], Coulomb nuclear potentials, core charge densities and wave functions are performed.

2.4.2 Bellaiche and Vanderbilt VCA approach

The weighted averaging method of Bellaiche and Vanderbilt [62] gives another capability to realize effective virtual crystal approximation approach. The basic ideas of the viable VCA implementation for the DFT methods can be expressed as:

$$V_{ext}(r, r') = \sum_i \sum_{\alpha} \omega' v_{ps}^{\alpha} (r - RI\alpha^{r'} - RI\alpha), \quad 2.22$$

where, the total external potential V_{ext} is the sum of the non-local potentials of each atomic species, α , taken with the weights, ω , of the components atoms in the mixture atom. Interestingly, this approach can be used to study any composition in a solid solution [62]. Its advantages are the ability to treat heterovalent systems and to apply all kinds of first principles pseudo potentials. Furthermore, this method can be considered also as a kind of simple mixing of the pseudopotentials in norm-conserving type, though the additional averaging process is performed in the case of the ultrasoft pseudopotential.

2.5 UNiversal CLuster-Expansion

In order to minimize the sensitivity of the cluster expansion (CE) to the user choices, and to make cluster expansion applicable beyond simple bulk binary systems, a new program package under the name UNiversal CLuster Expansion (UNCLE) [63] has been developed by the group of S. Muller, at the Technical University of Harburg-Hamburg. In addition, cluster expansion is a method that describes the energy of a system as a function of occupation variables for a lattice position [64]. The UNCLE code is able to perform a complete CE fit using a genetic algorithm. It also predict the ground states of systems containing up to three and more elements. The cluster expansion method constructs an Ising-like Hamiltonian for the energies of different atomic configurations. Moreover, structures with negative heats of formation (ΔH_f) are thermodynamically stable (miscible constituents), while all structures with positive ΔH_f are thermodynamically unstable (miscibility gap), they need phase separation. The energy of the

structures close to the ground state line are most accurate and ground state structures can be efficiently and reliably identified. In this study, the cluster expansion technique was investigated for the system platarsite (PtAsS) to generate new stable systems.

2.5.1 Miscible constituents

A system has miscible constituents, if all structures have negative ΔH_f and all the ordered structures are thermodynamically stable. However, structures with energies close to the ground states, that is those with the lowest ΔH_f at a given concentration, are the most important ones and the cluster expansion should be most accurate for those structures. To accomplish this, the structures predicted by the cluster expansion to be more favourable and are not yet part of the training set is added to the training set. This is done until no new structures are predicted by the cluster expansion to be more favourable (with a lower ΔH_f) than those already included in the training set. At this point the cluster expansion has converged. From all structures considered by the cluster expansion the thermodynamically stable ones have been identified.

2.5.2 Miscibility gap

If the system has miscibility gap, there are no stable ordered structures that exist apart from the two pure phases and all structures are of equal importance to the cluster expansion. Therefore, the selection process of structures to be added to the training set has to improve the quality of the cluster expansion for all structures considered, irrespective of their formation energies ΔH_f . To determine how good (or bad) the energies of the structures are predicted by the cluster expansion the stochastic nature of the genetic algorithm is used. CE approach was performed using the PtAs₂ as our initial starting point and the sulphur atom was added at the same position as arsenic atom. The energy of all considered structures are then predicted by these multiple J 's and a standard deviation of the predicted energies is evaluated. Structures with the highest standard deviation are those whose description by the cluster expansion is the worst. However, these are added iteratively to the training set.

2.6 Plane-wave pseudo potential codes

In this dissertation we have employed two plane wave pseudopotential codes i.e. VASP and CASTEP codes. The VASP code has been used to determine the equilibrium lattice parameters, the phonon dispersion, the elastic constants, the heats of formation and the density of states for PtAs₂, PtAsS (crystal structure and cluster expansion) and Pd₂As structures. The same code

was used to determine the surface properties for all the systems. In addition, CASTEP code was used to investigate the same properties for the PtAsS solid solution structure since VASP code cannot handle disordered systems. All the results computed will be presented in the next chapters.

2.6.1 VASP implementation

The Vienna *Ab-initio* Simulation Package (VASP) [57] is a leading electronic structure code for solids, surfaces and interfaces. VASP also performs *ab-initio* quantum mechanical molecular dynamics (MD) using Vanderbilt pseudopotentials or projector augmented wave (PAW) method and a plane wave basis set. The interaction between ions and electrons is described using ultrasoft Vanderbilt pseudopotentials (US-PP) or the projector augmented wave method [65]. The methodology behind this is DFT, but the codes allows the use of post-DFT corrections such as the hybrid functionals mixed with DFT and Hartree-Fock exchange, many-body perturbation theory and dynamical electronic correlations within the random phase approximation [66].

The techniques also allow a considerable reduction of the necessary number of plane waves per one atom for transition metals and the elements in the first row. Forces and stresses can be easily calculated with VASP and used to relax atoms into their instantaneous ground state. The PAW method, developed by Blöchl [65], is a very powerful tool for performing electronic structure calculations within the framework of density functional theory [41, 42], combining some of the best features of pseudopotential and all-electron approaches. VASP uses efficient matrix diagonalization schemes and an efficient Pulay/Broyden charge density mixing, these techniques avoid all problems occurring in the original Car-Parinello method, based on the simultaneous integration of electronic and ionic equations of motion.

The structural relaxation, structural properties, elastic and mechanical properties, vibrational properties, electronic properties and surface properties for the PtAs₂, PtAsS (CE) and Pd₂As bulk structures were calculated self consistently using DFT within GGA functional. The electronic wave functions were expanded in a plane-wave basis set with periodic boundary conditions.

2.6.2 CASTEP implementation

The Cambridge Serial Total Energy Package (CASTEP) [56] is a first principles quantum mechanical code that explores the properties of crystals and surfaces. Within density functional

formalism it can be used to simulate wide range of materials that include surfaces, crystalline solids, molecules, liquids and amorphous materials. The CASTEP code was originally developed by Payne and Co-workers in the late 1980's and early 1990's [44]. The code became widely used for electronic structure calculations. In addition, the new CASTEP code has been designed for parallel computers, allowing much larger problems to be approached.

The code is capable of calculating the physical properties of materials including: calculations of total energies, forces, stresses and elastic constants; electronic structures: electronic charge densities, orbitals, electrostatic potentials, band structures, total and partial density of states, Mulliken population analysis and optical properties; geometry optimisation: optimisation of atomic position and unit cell parameters, either constrained or unconstrained and under external pressure and stresses; transition states: the LST/QST methods are utilized when finding transition states and exchange correlation: the well-known LDA and GGA functionals are included (such as PW91, PBE and RPBE functionals), furthermore non-local functionals such as the weighted density approximation (WDA), Hartree-Fock and screened exchange are also available and many other physical properties of materials.

Ab-initio quantum-mechanical density functional theory [38] calculations were performed to investigate the stability of the structural, thermodynamic, elastic, mechanical and electronic properties of PtAsS (VCA) structure. However, the program is capable of performing the single-point energy calculations as well as the geometry optimization calculations.

2.9 Theoretical background of calculated properties

2.9.1 Heats of formation

The heat of formation (ΔH_f) is defined as the heat released or absorbed during the formation of a pure substance from its element. ΔH_f provide a fundamental understanding on stabilities of compound phase diagram construction. The standard enthalpy of formation or standard heat of formation of a compound is the change in enthalpy that accompanies the formation of a mole of a substance in its standard state from its composite elements in their standard states. The equilibrium total energies of the discharge products arsenic and sulphur are calculated using CASTEP and VASP. The heats of formation will be used for predicting the stability trend of PtAs₂, PtAsS and Pd₂As structures. They will be calculated as follows:

$$\Delta H_f(PtAsS) = \frac{1}{N} [E_{PtAsS} - (E_{Pt} + E_{As} + E_S)] \quad 2.23$$

$$\Delta H_f(PtAs_2) = \frac{1}{N} [E_{PtAs_2} - (E_{Pt} + 2E_{As})] \quad 2.24$$

where, N is the total number of atoms in the unit cell, E_{PtAs_2} and E_{PtAs_2} are the total energy of the system and E_{Pt} , E_{As} and E_S are the elemental individual total energies of platinum, arsenic and sulphur, respectively. The same will be done for Pd_2As structure. The heats of formation results will be discussed in the chapter 3.

2.9.2 Elasticity

The elastic constants (C_{ij}) consist of some of the paramount information that can be easily obtained from the ground state total energy calculations from the viewpoint of material physics. A given crystal structure cannot exist in a stable or metastable phase unless its elastic constants obey certain relationships. However, elastic constants contain some of the vital information regarding the strength of the materials against an extremely applied strain and act as stability criteria to study mechanical stability structural transformation [67, 68]. Elastic properties are more important in understanding solid state physical, chemical and mechanical properties. They relate to diverse fundamentals solid state properties including, equation of states, interatomic potentials, phonon spectra and lattice constants.

Interestingly, elastic constants of a material describes its response to the external applied strain required to maintain a deformation and provides useful information of the strength of material characterised by the bulk modulus (B), Young's modulus (E), isotropic shear modulus (G), tetragonal shear modulus (C'), Poisson's ratio (ν) and shear anisotropy factor (A). All elastic constants can be determined by direct computation since first principle calculations that uses periodic boundary conditions assumes the occurrence of a single crystal. The elastic constants calculations were inaugurated by Born [69]. The criteria of Born stability are a set of condition on the C_{ij} that are related to the second order change in the internal energy of a crystal under formation. Furthermore, it was later revealed that the ranges of Born stability are sensitive to choice of coordinates [70].

Born conditions were found effective only for unstressed system and not effective for the stressed system [71]. Barron and Klein indicated that the normal definition of the elastic constants derived from Helmholtz free energy cannot be directly applied to the study of the stress-strain relationship of a stressed system [72]. However, the elastic constants cannot be used as stability criteria for a stressed system as demonstrated by Wang and Co-workers [71].

They suggested using the elastic stiffness coefficients as stability criteria for isotropic stress. For anisotropic stress, they obtained a more general form from path-dependent finite displacements. The stability criteria is framed in terms of elastic stiffness coefficients which govern the proper relations of stress and strain at finite strain by considering both the internal and the external work done during the deformation process [73]. This is an indication that the stability analysis can predominantly be determined by an appropriate generalization of the zero-stress elastic constants which valid for arbitrary stress.

Bulk modulus [74] is one of the important parameters that characterise the physical property of a material system, since it also measures the degree of stiffness or the energy required to produce a given volume deformation. Shear modulus [75] describes the resistance to shape change caused by shearing force and the Young's modulus reflects the resistance of materials against uniaxial tensions [76]. The bulk modulus depicts the bonding characters in the material and it is used as an indicator for the strength and hardness of materials [77]. In addition, Pugh introduced the ratio of bulk to shear modulus (B/G) of a material. The ratio express that the shear and bulk moduli signifies the resistance to deformation of plastic and a resistance to fracture. A high B/G value is associated with ductility, whereas a low B/G value represents brittleness. The value separating brittleness and ductility is 1.75 [78].

2.9.2.1 Definition of elastic constants

To determine elastic constants of a crystal, a deformation of the unit cell is created by changing the Bravais lattice vectors $\mathbf{R} = (\mathbf{a}, \mathbf{b}, \mathbf{c})$ of the undisturbed unit cell $\mathbf{R}' = (\mathbf{a}', \mathbf{b}', \mathbf{c}')$ using a strain matrix e

$$R' = R \begin{pmatrix} 1 + e_{xx} & \frac{1}{2}e_{xy} & \frac{1}{2}e_{xz} \\ \frac{1}{2}e_{yx} & 1 + e_{yy} & \frac{1}{2}e_{yz} \\ \frac{1}{2}e_{zx} & \frac{1}{2}e_{zy} & 1 + e_{zz} \end{pmatrix} \quad 2.25$$

The deformation leads to a change of the total energy of the crystal

$$U = \frac{E_{tot} - E_0}{V_0} = \frac{1}{2} \sum_{i=1}^6 \sum_{j=1}^6 C_{ij} e_i e_j \quad 2.26$$

where E_0 is the total energy of the unstrained lattice, V_0 is the volume of the undistorted cell and the C_{ij} are the elements of the elastic constant matrix with a notation that follows standard

convention. Both i and j run from 1 to 6 in the sequence {xx, yy, zz, yz, xz, xy}. The tensor of elasticity has 36 elements, the elastic constants, but maximally 21 of these are independent.

2.9.2.2 Calculations of elastic constants

The simplest case by far is the cubic system where there are only three independent constants, C_{11} , C_{12} and C_{44} . We use this case to illustrate the manner in which the stiffness matrix elements may be determined from strain fields of the form (2.25). If the applied strain is $e_{xx} = e$ with all other e_i equal to zero, the energy change $U = C_{11}e^2/2$ is. This allows a unique determination of C_{11} . If $e_{yz} = e_{zy} = e/2$, with all other strain components zero, then $U = C_{44}e^2/2$ and we have an independent determination of C_{44} . The bulk modulus, B , is the response to a uniform compression so applying the strain field $e_{xx} = e_{yy} = e_{zz} = e$ allows the computation of B via the relation $U = Be^2/2$. Similarly, the shear modulus can be calculated by using the strain field $e_{zz} = e; e_{xx} = e_{yy} = -e/2$, whereupon $U = 3C'e^2/2$. Finally, the off-diagonal stiffness matrix element C_{12} can be calculated using one or other of the relations.

$$B = \frac{1}{2}(C_{11} + 2C_{12}) \quad 2.27$$

$$C' = \frac{1}{2}(C_{11} - C_{12}) \quad 2.28$$

Using both of these relations provides a useful independent check on the accuracy of the computation. A symmetry-general formulation of the calculation of elastic constants from total energy calculations is given by Le Page and Saxe [79].

2.9.2.3 Elastic constant stability conditions

The elastic properties of single crystals are described by the elements C_{ij} of the elasticity tensor. For each material, both stress and strain have three tensile and three shear components, giving six components in total. According to the theory of elasticity, a 6 x 6 symmetry matrix with 36 elements is thus needed to describe the relationship between stress and strain. The structural symmetry of crystal makes some of the matrix elements equal and others fixed at zero.

For the cubic, tetragonal, orthorhombic and monoclinic crystals, there are three (C_{11} , C_{12} , C_{44}), six (C_{11} , C_{12} , C_{13} , C_{33} , C_{44} , C_{66}), nine (C_{11} , C_{22} , C_{33} , C_{12} , C_{13} , C_{23} , C_{44} , C_{55} , C_{66}) and thirteen (C_{11} , C_{22} , C_{33} , C_{12} , C_{13} , C_{23} , C_{44} , C_{55} , C_{66} , C_{15} , C_{25} , C_{35} , C_{46}) independent elastic constants. Applying two kinds of strains (ϵ_1 and ϵ_4) can give stresses relating to these three elastic

coefficients, yielding an efficient method for obtaining elastic constants for the cubic system. This method has been successfully used to study the elastic properties of a range of materials including metallic systems [80]. The mechanical stability criteria of cubic systems as outlined elsewhere [81] and are given as follows:

$$C_{44} > 0, C_{11} > |C_{12}| \text{ and } C_{11} + 2C_{12} > 0, \quad 2.29$$

C_{11} , C_{12} and C_{44} are the only three independent elastic constants. Based on these three independent single crystal elastic constants of a cubic crystal, the elastic moduli are determined using the following expressions:

$$B = \left(\frac{C_{11} + 2C_{12}}{3} \right), C' = \frac{C_{11} - C_{12}}{2}, A = \frac{2C_{44}}{C_{11} - C_{12}}, \quad 2.30$$

where B is the bulk modulus, C' tetragonal shear modulus and anisotropic factor A . It is acknowledged that the bulk modulus B is a measure of resistance to volume changed by applied pressure, whereas the elastic anisotropy A has an important implication in engineering science since it is highly correlated with the possibility of inducing micro-cracks in materials [82]. If the material is completely isotropic, the value of A will be 1, while values smaller or larger than 1 measure the degree of elastic anisotropy. The positive C' indicates the mechanical stability of the crystal, otherwise unstable. The corresponding mechanical stability criteria for tetragonal crystal read as

$$(C_{11} - C_{12}) > 0, (C_{11} + C_{33} - 2C_{13}) > 0, (2C_{11} + C_{33} + 2C_{12} + 4C_{13}) > 0, \\ C_{11} > 0, C_{33} > 0, C_{44} > 0, C_{66} > 0, \quad 2.31$$

While the requirement for mechanical stability in an orthorhombic crystal leads to the following restrictions on the elastic constants [83]:

$$C_{11} + C_{12} + C_{33} + 2C_{12} + 2C_{13} + 2C_{23} > 0, C_{22} + C_{33} - 2C_{13} > 0, \\ C_{11} > 0, C_{22} > 0, C_{33} > 0, C_{44} > 0, C_{55} > 0, C_{66} > 0, \quad 2.32$$

A monoclinic phase is considered stable if the following mechanical stability criteria are satisfied. On the other hand, the Born mechanical stability criteria for monoclinic system [84] is given by:

$$[C_{11} + C_{22} + C_{33} + 2(C_{12} + C_{13} + C_{23})] > 0, (C_{33}C_{55} - C_{35}^2) > 0, (C_{44}C_{66} - C_{46}^2) > 0,$$

$$(C_{22} + C_{33} - 2C_{23}) > 0, [C_{22}(C_{33}C_{55} - C_{35}^2) + 2C_{23}C_{25}C_{35} - C_{23}^2C_{55} - C_{25}^2C_{33}] > 0,$$

$$\{2[C_{15}C_{25}(C_{33}C_{12} - C_{13}C_{23}) + C_{15}C_{35}(C_{22}C_{13} - C_{12}C_{23}) + C_{25}C_{35}(C_{11}C_{23} - C_{12}C_{13})] - [C_{15}^2(C_{22}C_{33} - C_{23}^2) + C_{25}^2(C_{11}C_{33} - C_{13}^2) + C_{35}^2(C_{11}C_{22} - C_{12}^2)] + gC_{55}\} > 0, \quad 2.33$$

$$g = C_{11}(C_{22}C_{33} - C_{11}C_{23}^2 - C_{22}C_{13}^2 - C_{33}C_{12}^2 + 2C_{12}C_{13}C_{23}), [85]$$

The calculated elastic constants for monoclinic phase allow us to obtain their macroscopic mechanical parameters, namely isotropic bulk (B) and shear moduli (G) in the Voigt (V) approximation. The Young's modulus and a Poisson's ratio of a crystal can be given from the following equations:

$$E = \frac{9BG}{3B + G}, \quad \nu = \frac{1}{2} \left[\frac{B_x - (2/3)G_x}{B_x - (1/3)G_x} \right] \quad 2.34$$

$$\Delta_P = \frac{C_{33}}{C_{11}}, \quad \Delta_{S1} = \frac{C_{11} - C_{13}}{2C_{44}}, \quad \Delta_{S2} = \frac{2C_{44}}{C_{11} - C_{12}} \quad 2.35$$

$$B_V = \frac{1}{9}(C_{11} + C_{22} + C_{33}) + \frac{2}{9}(C_{12} + C_{23} + C_{13})$$

$$G_V = \frac{1}{15}(C_{11} + C_{22} + C_{33}) - \frac{1}{15}(C_{12} + C_{23} + C_{13}) + \frac{1}{5}(C_{44} + C_{55} + C_{66}) \quad 2.36$$

$$\frac{1}{B_R} = (S_{11} + S_{22} + S_{33}) + 2(S_{12} + S_{23} + S_{13})$$

$$\frac{1}{G_R} = \frac{4}{15}(S_{11} + S_{22} + S_{33}) - \frac{4}{15}(S_{12} + S_{23} + S_{13}) + \frac{1}{5}(S_{44} + S_{55} + S_{66})$$

Where B_V , B_R , G_V and G_R are Voigt bulk modulus, Reuss bulk modulus, Voigt shear modulus and Reuss shear modulus respectively. However S_{ij} is the elastic compliance constants and can be obtained from elastic constants.

The Hill approach is approximated as the average of the Voigt and Reuss. The bulk modulus and shear modulus of materials with Voigt-Reuss-Hill approximation [86] can be expressed as:

$$B_H = \frac{1}{2}(B_R + B_V) \text{ and } G_H = \frac{1}{2}(G_R + G_V) \quad 2.37$$

For an elastically isotropic monoclinic crystal, the three anisotropy ratios (A_1 , A_2 and A_3) must be simultaneously equal to unity [87]. Many low-symmetry crystals exhibits a high degree

of elastic anisotropy [88]. The shear anisotropic factors in different crystallographic planes provide a measure of the degree of elastic anisotropy of atomic bonding in different planes. The shear anisotropic factors for non-cubic phases are given by:

$$A_1 = \frac{4C_{44}}{C_{11} + C_{33} - 2C_{13}}, \quad 2.38$$

$$A_2 = \frac{4C_{55}}{C_{22} + C_{33} - 2C_{23}}, \quad 2.39$$

$$A_3 = \frac{4C_{66}}{C_{11} + C_{22} - 2C_{12}}, \quad 2.40$$

for the (100), (010) and (001) planes respectively. The elastic anisotropy A has an important implication in engineering science since it is highly correlated with the possibility of inducing microcracks in materials [89]. If the material is completely isotropic, the value of A will be equal to unity, whereas values smaller or larger than 1 measure the degree of elastic anisotropy.

The Young's modulus E is defined as the ratio between stress and strain and is used to provide a measure of the stiffness of the solid, i.e. the larger the value of E , the stiffer the material. Poisson's ratio (ν) refers to the ratio of transverse contraction strain to longitudinal extension strain during stretching, thus reflecting the stability of the crystal against shear. Hence, the higher the Poisson's ratio is, the better ductility the crystalline metal has at low temperatures. However, it is acknowledged that the bulk modulus B is a measure of resistance to volume changed by applied pressure. Thus the macroscopically measurable quantities obtained for materials are the shear modulus, which represents the isotropic response for shearing, Young's modulus corresponding to the stress-strain ratio in the case of tensile forces, bulk modulus, Poisson's ratio and the anisotropy constant. These are all important for technological and engineering applications.

2.9.3 Phonon dispersion curves

The phonon dispersion curves are defined as the k wave vector dependence of the frequencies $\omega(k, j)$ of the normal modes for all branches of and selected directions in the crystal. They have an essential role in several physical properties of condensed matter physics and these include mechanical stability, electrical conductivity and thermal conductivity. These properties indicate an excited state in the quantum mechanical quantization of the vibration modes of the elastic structures of interacting particles. The phonon dispersion behaviour

branches reflects specific features of the crystal structure and the interatomic interactions. However, these gives the most comprehensive and detailed information about the dynamical properties of a crystals.

The phonon vibrations frequencies are calculated as follows [90, 91]:

$$\omega = v_s q \quad 2.41$$

where v_s is the speed and q is the wave-vector of the lattice vibrations.

In crystal where there are two or more types of atoms, two types of modes of vibrations are displayed *i.e.* optical and acoustic modes. Optical phonons arise from the vibration out of phase between neighbouring atoms within the unit cell, whereas acoustic phonons gives rise to in phase vibrations. In addition, the acoustic modes have zero frequencies at $q = 0$ (the center of the Brillouin zone (Γ), while the optical modes have non-zero. The acoustic and optical modes split into longitudinal and transverse modes. They are abbreviated as longitudinal acoustic (LA), transverse acoustic (TA), longitudinal optical (LO) and transverse optical (TO).

A linear relationship between frequency and long wavelengths phonon wave-vector is displayed in the acoustic mode. Positive vibrational frequencies indicate stability of the system, while negative vibrational frequencies (soft modes) shows mechanical instability.

2.9.4 Density of states

The density of states (DOS) of a system describes the number of states per interval of energy at each energy level that are available. The DOS indicates how densely packed quantum states are in a system. Integration of DOS over a range of energy yields a number of states;

$$N(E) = \int_E^{\Delta E} g(E) dE \quad 2.42$$

where $N(E)$ denotes the carrier density and $g(E)dE$ represents the number of states between E and dE . The density of states permits integration to be done with respect to the electron energy instead of the integration over the Brillouin zone. It is often used for quick visual analysis of the electronic structure. Characteristics such as the width of the valence band, the energy gap in insulators and the number of intensity of the main features are helpful in interpreting experimental spectroscopic data. The most accurate methods used are based on linear or quadratic interpolations of band energies between the reference points in the Brillouin zone. The most popular and reliable technique is based on the tetrahedron interpolation. The most

popular and reliable technique is based on the tetrahedron interpolation. However, it is not well suited to the Monkhorst-Pack grid of special points [60]. VASP code uses a simplified linear interpolation scheme. The method is based on linear interpolation in parallelepipeds formed by the points of the Monkhorst-Pack set, which is followed by the histogram sampling of the resultant set of band energies.

In the study of complex minerals there can be a formation of pseudo gap in the electronic density of states at the Fermi energy (E_F) and the relation of this feature to the stability of the particular structure. Pierce *et al.* [92] and Matsuda *et al.* [93] have suggested the role of pseudo gap in the structural stability by the experimental observation of very high resistivity in structurally well-ordered stable quasicrystals. Several contexts have proposed the direct relations between the formation of a pseudo gap and stability of the structure [93]. Literature reveals that densities of states are also essential in determining the stability trend of structures with same composition with respect to the E_F . The theory suggests that the element with highest density of states around the E_F is considered the least stable, while the element with the lowest density of states is the most stable [94, 95]. Moreover, the element with greater contribution at the E_F is the most active or reactive element.

2.10 Charge population analysis

The properties of chemicals and materials are often described in terms of charge transfer between atoms and the presence of ionic charges or electric multipoles on atoms or molecules. Theoretical calculations producing estimates of the electronic charge distribution in the system can, in principle, provide this type of information but it is not clear how to extract it. However, the atomic charges in molecules or solids are not observables and therefore not defined by quantum mechanical theory. The output of quantum mechanical calculations is a continuous electronic charge density and it is not clear how one should partition electrons amongst fragments of the system such as atoms or molecules.

Many different schemes have been proposed, some are based on electronic orbitals (such as Mulliken Population Analysis) and others based on only the charge density such as Bader's atoms in molecules method. The Mulliken analysis is the most commonly used orbital based method. It can be applied when basis functions centered on atoms are used in the calculation of the electronic wave functions of the system. The charge associated with the basis functions centered on a particular atom is then assigned to that atom. This can be a fast and useful way of determining partial charges on atoms but it has the major drawback that the analysis is

sensitive to the choice of basis set. A different approach is to focus on the charge density that has been proposed by Bader [96].

The space is then divided into regions by surfaces that run through minima in the charge density. More precisely, at a point on a dividing surface the gradient of the electron density has no component normal to the surface. The regions bounded by such dividing surfaces are referred as Bader regions. Because this analysis is based solely on the charge density, it is rather insensitive to the basis set used in the electron wave function calculation and can be used to analyse plane wave based calculations as well as calculations using atomic basis functions. In addition, a common complaint about Bader analysis is the computational effort and complexity of the algorithms that have been developed [97, 98]. A commonly used implementations [96, 99, 100] involve finding the critical points of the charge density where $\Delta\rho = 0$, followed by the construction of the zero-flux surfaces which intersect these points and then integration of the electronic density within each region. Several refinements have been made since the initial implementation of the method [96, 97, 101]. Most recently Malcolm and Popelier [102] have used dynamic grid techniques introduced by Silvi and co-workers [103, 104] in order to effectively treat complicated bonding topology. The current implementations of Bader's analysis are based upon a grid of charge density values where only steepest ascent trajectories confined to the grid points are used to identify the Bader regions [105, 106, 107].

2.11 Cleaving of surfaces

The modelling of mineral surfaces is a process of exposing surface which is similar to liberation of particles experimentally during ore or mineral grinding. The surface modelling was achieved by generating two dimensional slabs of a mineral within a three dimensional unit cell [108]. This was done by cleaving the mineral bulk along the low Miller index plane to generate a bulk-termination surface which extends indefinitely in two dimensions whilst simultaneously extending a vacuum layer along the third dimension, as presented in Figure 2.2. Moreover, this emulated the crushing of the rock ore, where different surfaces are exposed. In principle, different minerals prefers to cleave or break a certain planes which are thermodynamically stable, in particular those with interplanar spacing and larger bonds [108].

Gibbs [109] developed the concept that the equilibrium structure of a crystal will possess the minimum possible excess energy for a given volume, and as volume and surface area are inseparably linked, the crystal face with the lowest surface energy will predominate. However,

finding the surface structure with the lowest surface energy for each metal or mineral under study offers the best chance of defining a broadly representative working surface.

Consideration must be given to the large number of both Miller index planes and, within each plane, all possible bulk terminations that exist.

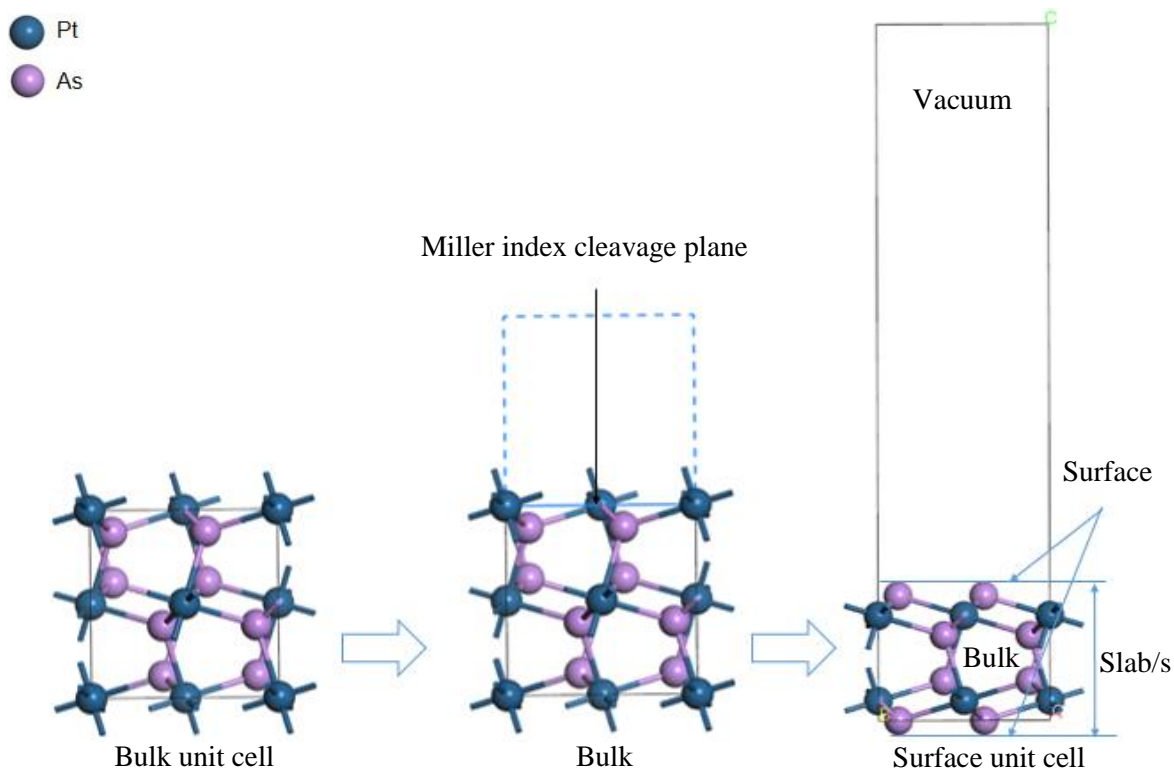


Figure 2.2: A simplified representation of the surface cleavage methodology for PtAs₂.

Due to the periodic boundaries, and as indicated in Figure 2.2, both top and bottom faces of the mineral slab are bulk termination and hence exposed surfaces. The geometry of the top surface is determined by which Miller index plane and surface terminations is chosen. The bottom surface is determined by the slab depth. Slab depth is an important factor when modelling surfaces in this way, as shallow slabs may be a poor mimic of a solid-state interface system [108]. However, the principal concern is that the slab depth is sufficient such that both surfaces act as if above an effectively infinite amount of the bulk solid (i.e. the surfaces do not interact with one another through the solid). Ideally to achieve this a large slab depth would be used but the computational cost of modelling very deep slabs was avoided.

The initial trial in surfaces cleavage was to obtain the most preferred surfaces termination that possesses no dipole. If a surface termination possesses a dipole it may be corrected by reconstruction. There are different types of surfaces as discussed by Tasker [1] as shown in Figure 2.3. It is shown that Type I surface has a repeat unit cell where all the anions and cations in the same plane are in stoichiometric ratio. Type II surface has a stacking sequence of charged

planes, but the repeat unit consists of several planes, which when considered together have no dipole moment perpendicular to the surface. Type III surface are made up of a stack of alternately charged planes and produce a dipole moment perpendicular to the surface if cut between any planes. In nature these surfaces are stabilized by defects and/or adsorbed species. To be able to simulate Type III the dipole needs to be removed, hence the reconstructed Type III surface.

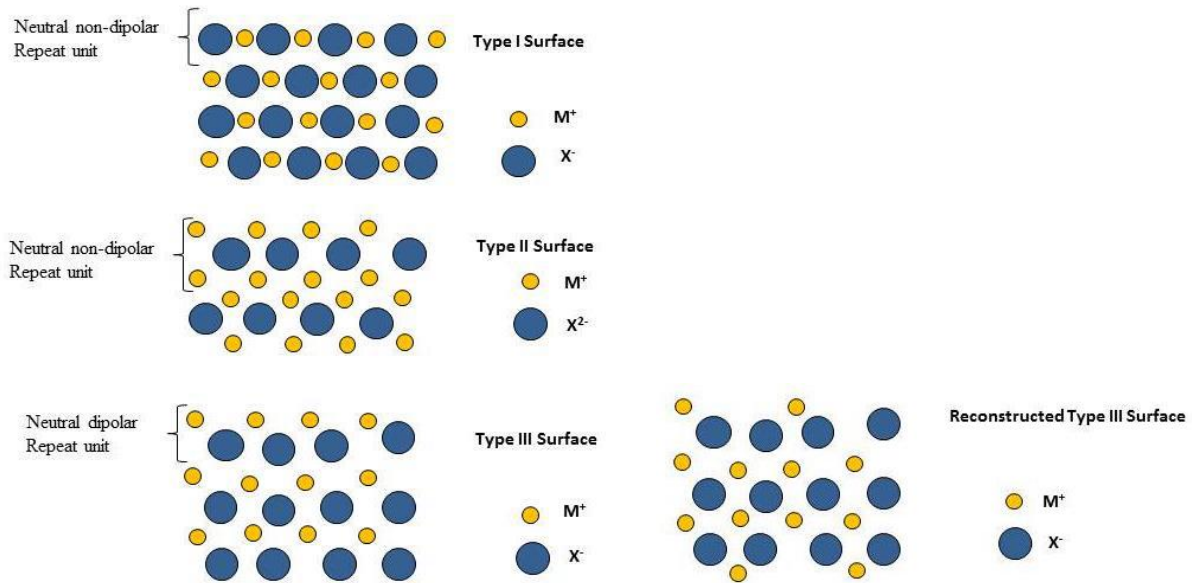


Figure 2.3: Representation of the different types of surfaces.

The geometry of the top termination surface was determined by which miller index plane and surface termination was chosen, the bottom termination surface was determined by the slab depth. The bottom termination of the slab must be symmetric to the top termination for a stable surface slab. It is clear that the most stable surface with no dipole are stoichiometric (must be bulk equivalent) and symmetric (both top and bottom must be mirror image).

The stability of the surface terminations and slab thickness can be measured computationally by calculating the surface energy, a measure of the excess energy per unit area induced by cleaving a bulk model, where a small, positive number indicates a stable surface as shown in Equation 2.4.3.

$$E_{\text{surface}} = \left(\frac{1}{2A} \right) [E_{\text{slab}} - n(E_{\text{bulk}})], \quad 2.4.3$$

where $E_{(\text{slab})}$ is the energy of the surface, $E_{(\text{bulk})}/\text{atom}$ is the energy of the bulk per total number of atoms in the bulk and $n_{(\text{slab})}$ is the number of atoms of the surface and A is the surface area.

This formula is used in order to account for the number of atoms in the surface and normalize it to the bulk.

Lastly, in order to reduce the search for most stable surfaces to a computationally tractable problem, whilst also ensuring that the most likely surfaces were surveyed, only the bulk terminations on the three low miller index (100), (110) and (111) were considered unless literature suggested otherwise.

CHAPTER 3

3. Structural, thermodynamic, mechanical and vibrational properties of PtAs₂, PtAsS and Pd₂As bulk structures

In this chapter, we discussed DFT results for the bulk structures PtAs₂, PtAsS and Pd₂As. For each mineral studied, a single point energy calculation was performed, followed by a geometry optimization of all the structures. We firstly discuss the Universal CLuster Expansion of Pt-As-S system and a detailed description on PtAsS virtual crystal approximation (VCA) approach. Secondly, we discuss the convergence test variation of the total energy cut-off and the k-points sampling. Thirdly, the structural and thermodynamic properties such as lattice parameters and heats of formation will be evaluated and discussed. Furthermore, the equilibrium cell volume together with the heats of formation will be correlated. We also investigate the elastic, mechanical and vibrational properties of PtAs₂, PtAsS (CE) and Pd₂As minerals using VASP code. The elastic and mechanical properties of PtAsS (VCA) were investigated using CASTEP code. Lastly, we have evaluated the elastic and mechanical properties and discussed the phonon dispersion curves along high symmetry directions within the first Brillouin zone direction and partial phonon density of states.

3.1 Cluster expansion approach and binary ground state diagram of Pt-As-S model

For the cluster expansion method we started by searching for the ground state of the PtAsS system of the DFT energy formation. Our initial starting point was PtAs₂, where the sulphur atoms were added at the same position as arsenic atoms. The X, Y and Z parameters were also fitted to be equivalent for both As and S atoms. The binary ground state diagram (Figure 3.1) showed that all structures have negative heats of formation (ΔH_f), hence they are thermodynamically stable (miscible constituents). Moreover, the cluster expansion showed a greater stability at 50/50 ($x = 0.5$) percentage, where arsenic and sulphur atoms are equally distributed in the structure with formed S-As dimer bond at the centre. We found that all structures between PtS₂ and PtAs₂, i.e. phases of PtAsS are more stable than PtS₂ and PtAs₂

and it was therefore conceivable that a number of phases can form. Moreover, some stoichiometries have multiple DFT inputs and only three stable structures of PtS_2 , PtAsS and PtAs_2 were shown in Figure 3.1. When no new ground states structures were found by the cluster expansion, the system was considered to have converged. The final DFT ground state line, CE predictions and DFT input are shown in Figure 3.1.

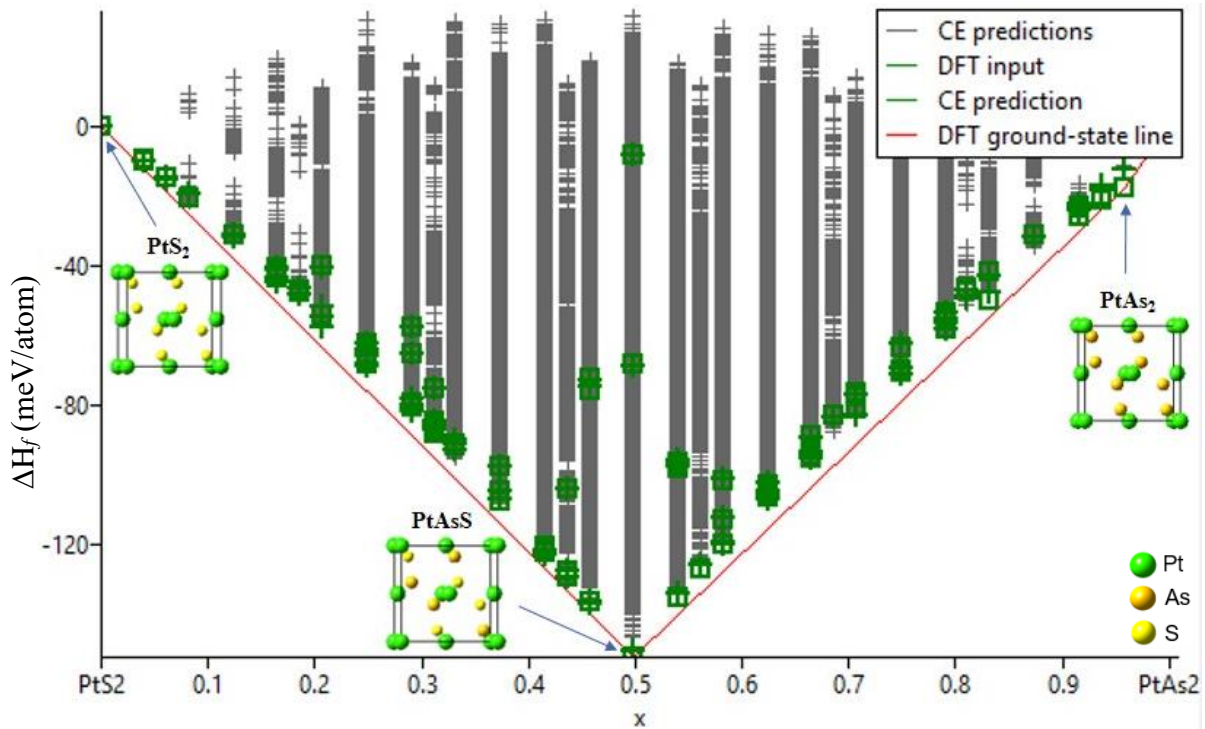


Figure 3.1: The cluster expansion binary ground state diagram obtained in determining the lowest ground states of Pt-As-S system.

The two structures, PtAs_2 and sulphur (Figure 3.2) were used to generate the stable PtAsS phases from the cluster expansion method as shown by the binary ground state diagram in Figure 3.1 and the obtained model for PtAsS is shown in Figure 3.2(c).

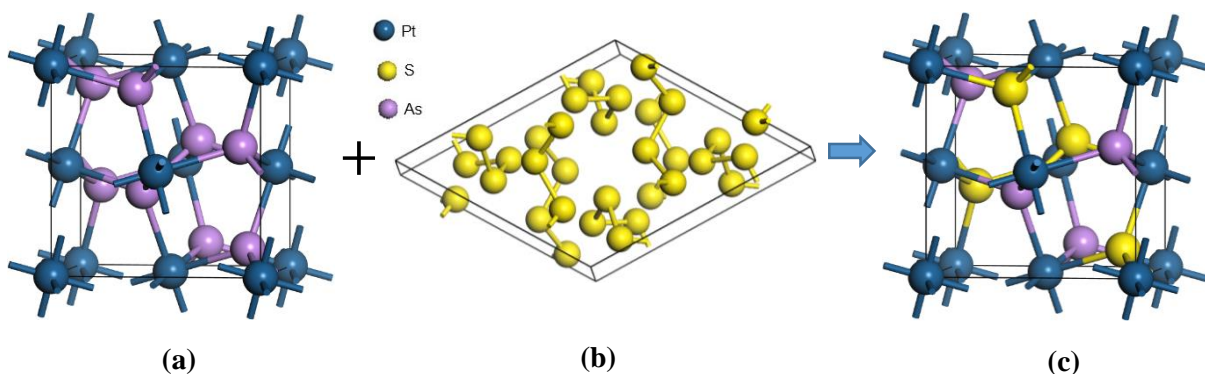


Figure 3.2: Cluster expansion approach on sperrylite with addition of sulphur atom at the same position of arsenic atom: (a) representing PtAs_2 model, (b) sulphur atom and (c) representing PtAsS model.

The cluster expansion model of the Pt-As-S sites remains inactive since the occupancy was unchanged (default). According to the ground state enthalpies of formation as derived by density functional theory and cluster expansion, the predicted structure shows formation enthalpies which are near the ground state line. However, Table B1.5 presented in appendix B showed 102 stable structures generated by cluster expansion. The system has successfully converged since there are no new structures on the last iteration after running for only 20 iterations (Table 3.1).

The actual structures and predicted values might be different in our calculation because of the stochastic process involved (see Table B1.5 in appendix B). However, the values on the second column gave the concentration of PtS₂ on the first line, PtAsS from line 2 to line 101 and PtAs₂ on the last line (line 102). The third column shows the vacancy of all the generated stable structures. The energy difference (4th column, D(E_DFT, E_CE)) compares the DFT input energy (3rd column, E_DFT) with the predicted energy (5th column, E_CE). Interestingly, the heat of formations for DFT (6th column, DHf_DFT) and the predicted values (7th column, DHf_CE) were negative and thus this indicated that structures with arsenic and sulphur vacancies are energetically favourable than pure PtAsS model.

Table 3.1: The progress of iterative procedure listing stable structures consisting of many pure phases.

Iteration	no. of struc.	no. of new struc.	CVS [meV/pos.]	% struc. with SD below 5 meV	new structures
0	0	2	-	-	ce1 ce22
0	0	7	-	-	ce382778 ce1792128 ce25726 ce1675835 ce1859856 ce1 ce22
1	7	5	0.069	-	ce2902869 ce2010853 ce596364 ce4224 ce6413
2	12	5	0.028	-	ce6750 ce4149 ce2698233 ce3035270 ce651526
3	17	5	0.0018	-	ce23 ce10219 ce701620 ce9836 ce270550
4	22	5	0.022	-	ce711429 ce10211 ce2050374 ce58 ce6234
5	27	5	0.0057	-	ce3024686 ce710142 ce1827040 ce4319 ce21737
6	32	5	0.86	-	ce463502 ce428 ce2693643 ce8423 ce3030270
7	37	5	0.69	-	ce2112830 ce2112096 ce10206 ce2113678 ce704296
8	42	5	0.88	-	ce166686 ce10190 ce1479445 ce312 ce749341
9	47	5	0.31	-	ce2847074 ce2868 ce632877 ce723456 ce3035143
10	52	5	1	-	ce461214 ce24 ce10082 ce18385 ce711426
11	57	5	0.89	-	ce10185 ce4199 ce70 ce695233 ce2113765
12	62	5	1.1	-	ce474560 ce4732 ce14304 ce731428 ce759509
13	67	5	1.2	-	ce3045133 ce2112050 ce711387 ce707467 ce711985
14	72	5	1.2	-	ce8399 ce632866 ce11964 ce2556 ce1018
15	77	5	1	-	ce5 ce1644619 ce32 ce2112359 ce526834
16	82	5	1	-	ce10110 ce53197 ce10191 ce414744 ce3404
17	87	5	1.2	-	ce4228 ce515032 ce711351 ce2111887 ce4227
18	92	5	1.2	-	ce710136 ce53213 ce4252 ce711321 ce632546
19	97	5	1.2	-	ce917 ce8374 ce23863 ce14892 ce18090
20	102	0	1.2	-	ce917 ce8374 ce23863 ce14892 ce18090

Considering Table 3.1, the values will differ in the calculation due to stochastic process involved in the CE. From the last line (20th iteration), we can discern that the final cluster expansion contains 102 structures in the training set and has a Cross Validation Score (CVS) of 1.2 meV/pos which is very good for the system. The following column stayed empty indicating that the optimized scheme never switched to the miscibility gap mode. Hence, the system have stable structures.

Table 3.2: The thermodynamic stable structures that summarizes the ground state line.

The structures constituting the DFT ground state line, their compositions x and formation energies DHf are:

#	$x(1:k,1:nC)$	DHf / atom [eV]	structure title	cell formula	space group
0.0000000000	1.0000000000	0.0000000000	ce22	Pt4S8	Pa-3
0.5000000000	0.5000000000	-0.1525456250	ce5	Pt4As4S4	P2_13
0.9583333333	0.0416666667	-0.0175684688	ce2111887	Pt12As23S	P3
1.0000000000	0.0000000000	0.0000000000	ce1	Pt4As8	Pa-3

In Table 3.2 we show the pure phases (Ce1 and Ce22) that possessed the Pa-3 space group, while the mixed phase of PtAsS (Pt₄As₄S₄) has P2_13 and P3 space group. We have considered the PtAsS (Pt₄As₄S₄) phase with P3 space group as it had a CVS of 1.2 meV/pos and thus preferred phases. Besides the pure phases Ce1 and Ce22, a total of two stable structures are shown to exist on the convex ground state line within the studied concentration range. This revealed that the structure of PtAsS model is quite complex with various stable compounds existing at different arsenic and sulphur concentrations.

3.2 Virtual crystal approximation approach PtAsS bulk model

The virtual crystal approximation within the CASTEP code is a tractable way of studying configurationally disordered systems. Our initial starting point was sperrylite whereby we have added the sulphur atom and mixed at the same lattice position of arsenic with both atoms having the same composition of 50% each. In this case two atoms that are sulphur and arsenic occupied the same lattice position as shown in Figure 3.3. The probabilistic occupations of each lattice site were selected as: 50% of As, 50% of S.

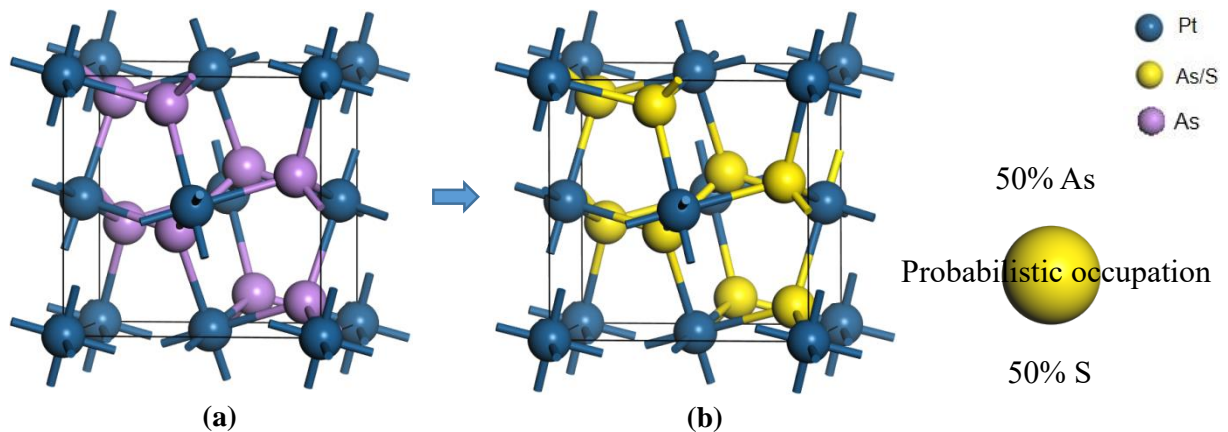


Figure 3.3: Virtual crystal approximation approach showing: (a) sperrylite bulk model and (b) PtAsS (VCA) model.

3.3 Convergence of the cut-off energy and k-points sampling

The cut-off energy and the k-points mesh are necessary as they determine the number of plane-waves required to perform the calculations. The accurate ground state total energy of PtAs₂, PtAsS and Pd₂As models were obtained by performing the convergence test on the cut-off energy with respect to the k-points mesh.

3.3.1 Cut-off energy variations

We employed the projector-augmented-wave plane-wave pseudopotential methods within the VASP code [57] for PtAs₂, PtAsS (CE) and Pd₂As models and CASTEP code [56] for PtAsS (VCA).

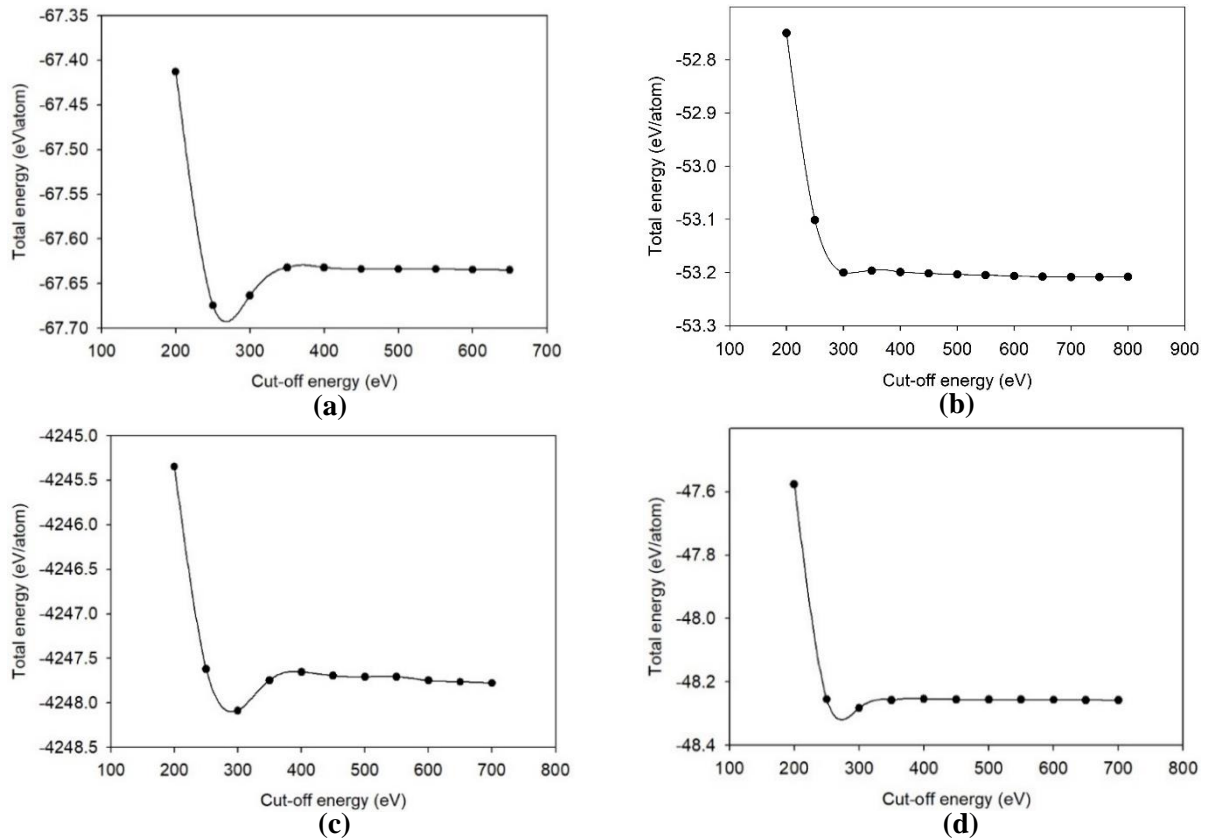


Figure 3.4: Total energy against kinetic energy cut-off: (a) cubic PtAs₂, (b) cubic PtAsS (CE), (c) cubic PtAsS (VCA) and (d) monoclinic Pd₂As structures.

Before any properties of a system are calculated, the cut-off energy must be varied in order to ensure good accuracy of the total energy. Structural optimization energy calculations were performed at different cut-off energy within the GGA-PBE [50] until a constant minimum energy is reached to within 0.01 eV/Å. The cut-off energy for the PtAs₂ PtAsS and Pd₂As

models were fully determined from a plot of a total energy against cut-off energy as shown in Figure 3.4. The plot showed almost zero slope starting from 450 eV for PtAs₂ and PtAsS, indicating that the variation of the total energy cut-off was negligible at these points (Figure 3.4a, Figure 3.4b and Figure 3.4c). The PtAs₂ and PtAsS (CE) curve smooths out from 450 eV with no additional drop. There does appear to be a small slope from 550 - 600 eV for PtAsS (VCA) as shown in Figure 3.4c. We considered the zero slopes between 450 and 550 eV to avoid computational costs. Furthermore, for the Pd₂As system, same zero slope was noted from 400 eV (Figure 3.4d). Thus the cut-off energy of 500 eV for PtAs₂ and PtAsS and 450 eV for Pd₂As were considered sufficient to converge the total energy of the bulk models.

3.3.2 k-points sampling

The number of k-points to be used in the plane-wave pseudopotentials must also be varied in addition to the cut-off energy. Several methods have been suggested for special sampling of k-points in the Brillouin zone [50, 60, 110, 111]. This method helps in k-points sampling in the Brillouin zone and ensure accuracy of the total energy.

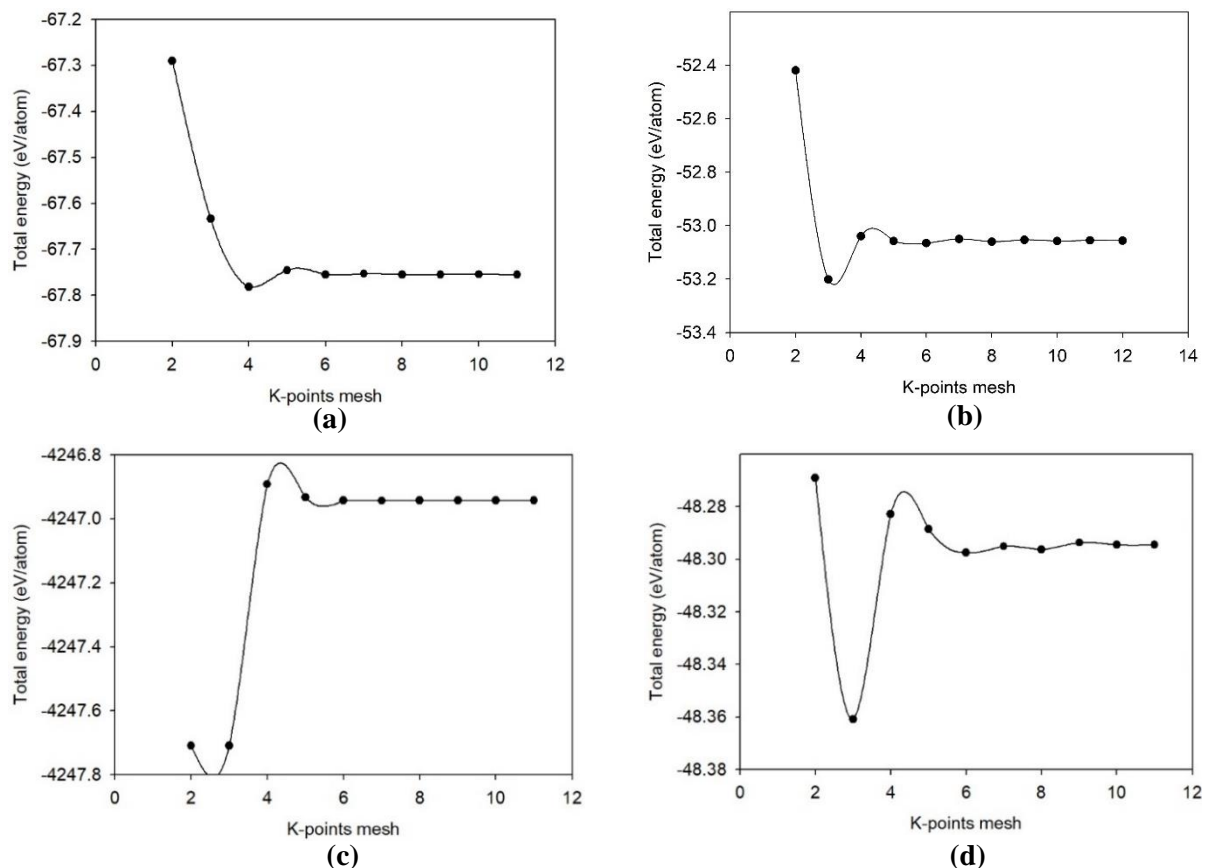


Figure 3.5: Total energy against k-points mesh: (a) cubic PtAs₂, (b) cubic PtAsS (CE), (c) cubic PtAsS (VCA) and (d) monoclinic Pd₂As structures.

The Monkhorst-Pack scheme [60] was employed to select the optimal set of k-points such that the greatest possible accuracy is achieved from the number of k-points used. Different number of k-points were varied from 2x2x2 to 11x11x11 for cubic PtAs₂ and PtAsS structures (Figure 3.5a, Figure 3.5b and Figure 3.5c) and from 2x2x4 to 11x11x22 for monoclinic Pd₂As structure (Figure 3.5d) until the total energy change is negligible and converged to within 1.0 meV. A k-point grid of 6x6x6 for the bulk PtAs₂ and PtAsS was chosen, while for Pd₂As model, a k-point mesh of 7x7x14 were used at fixed 500 eV and 450 eV cut-off energy, respectively (as found in section 3.3.1).

3.4 Structural and thermodynamics properties

In this section we investigated the structural properties such as lattice constants, heats of formation and cell volume for PtAs₂, PtAsS and Pd₂As structures. These properties play an important role in determining the structural stability of the system. They were determined by performing geometry optimization on the structure, allowing the cell volume and lattice to change. Furthermore, this was done also to allow the system to reach the ground state before any properties can be calculated. The equilibrium lattice constants were determined from the relaxed structures. Moreover, the experimental results of the lattice constants were also listed. In the next section we present, the lattice constants, cell volume and heats of formation of all the studied structures.

3.4.1 Bulk structure optimization

We have employed the VASP and CASTEP DFT codes using the plane-wave with PBE [50] exchange-correlation functional. The plane-wave basis set with an energy cut-off of 500 eV was set, which demonstrated convergence to within 0.2 meV/atom for both codes. The projector augmented wave pseudopotentials [65] were used and the electron configurations considered are: [Xe]4f¹⁴5d⁹6s¹ for Pt, [Kr]4d¹⁰ for Pd, [Ar]3d¹⁰4s²4p³ for As and [Ne]3s²3p⁴ for S atom. The smearing used was first order Methfessel-Paxton with a width of 0.2 eV and k-point grid of 6x6x6 for the bulk were generated using the Monkhorst-Pack [60] scheme. The size of the k-point grid used were not greater than 0.05 Å⁻¹. The convergence tolerances for force, ionic displacement and energy were 0.05 eVÅ⁻¹, 0.001 Å and 0.01 meV/atom, respectively.

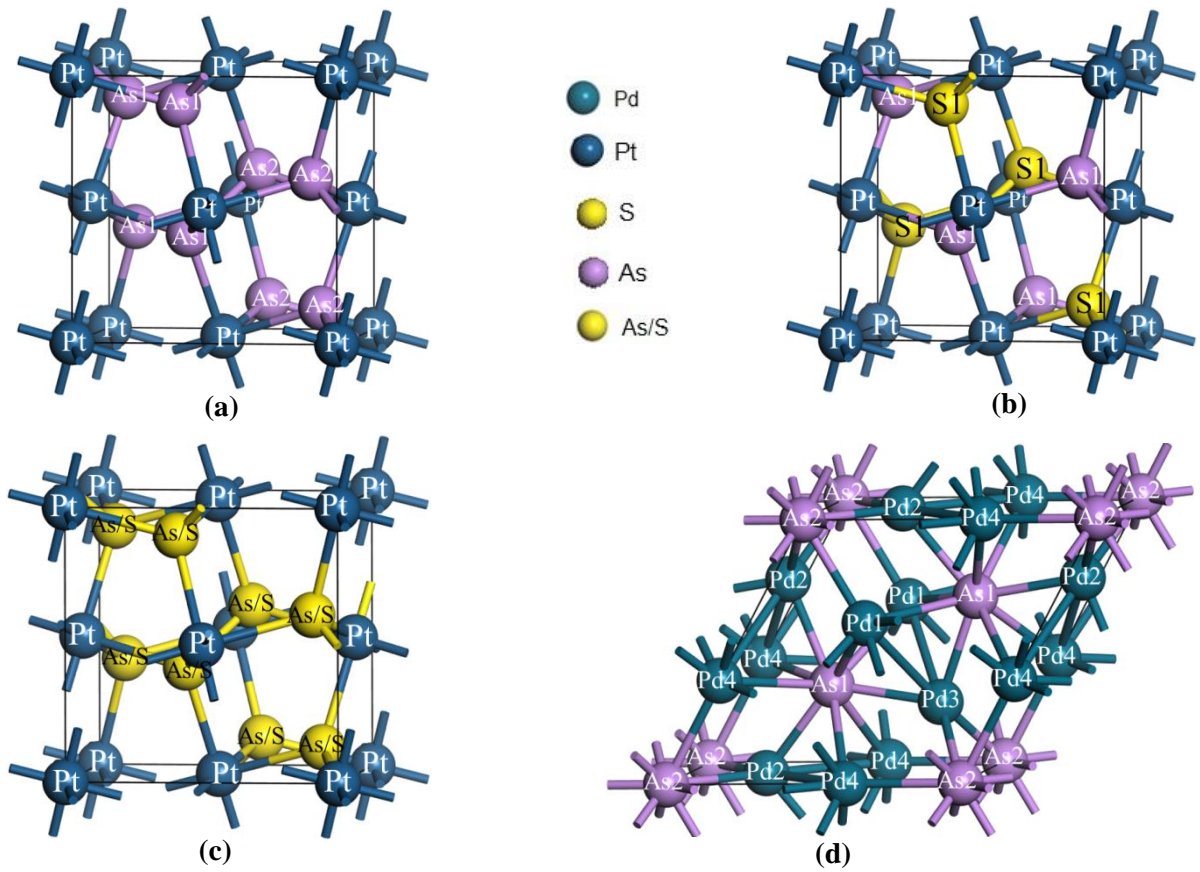


Figure 3.6: The relaxed bulk structures: (a) PtAs₂, (b) PtAsS (CE), (c) PtAsS (VCA) and (d) Pd₂As models.

Table 3.3 displayed the calculated lattice parameters with experimental values for comparisons and their cell volume. We found that, the computed and experimental lattice parameters yielded an acceptable agreement between them. The full structural relaxation was performed for PtAs₂ and PtAsS structures. The experimental study of the lattice parameters were reported for comparison. Our calculations result gave lattice structural parameters of $a = b = c = 6.061 \text{ \AA}$, whereas the experimental parameter were $a = b = c = 5.970 \text{ \AA}$ [112]. This showed good agreement between calculated and experimental lattice parameters values. The calculated lattice parameters were observed larger than the experimental lattice parameters as shown in Table 3.3. The equilibrium cell volume of $18.552 \text{ \AA}^3/\text{atom}$ was also calculated for sperrylite. The bulk structural properties of PtAsS (CE) model gave the most stable at 50/50 % of arsenic and sulphur. The calculated bulk parameters were found as $a = b = c = 6.024 \text{ \AA}$ and experimental value of $a = b = c = 5.790 \text{ \AA}$ [35], which also showed good agreement. However, the larger value suggested that GGA-PBE overestimated the lattice parameters. The optimized lattice parameters for PtAsS (VCA) bulk structure were calculated to be $a = b = c = 5.895 \text{ \AA}$ and the experimental value was $a = b = c = 5.790 \text{ \AA}$ [35]. This gave a good agreement between

the calculated and the experimental values, which shows that the VCA is able to predict the lattice form of PtAsS than the cluster expansion. In addition, the structures were found to have an equilibrium cell volume of 18.219 Å³/atom for PtAsS (CE) and 17.076 Å³/atom for PtAsS (VCA).

Table 3.3: The equilibrium calculated and experimental lattice parameters and cell volumes for PtAs₂, PtAsS (CE), PtAsS (VCA) and Pd₂As structures.

Structure	Lattice Parameters (Å)		Volume (Å ³ /atom)
	Calculated	Experimental	
PtAs ₂	a = 6.061	a = 5.970 [112]	18.552
PtAsS (CE)	a = 6.024	a = 5.790 [35]	18.219
PtAsS (VCA)	a = 5.895	a = 5.790 [35]	17.076
Pd ₂ As	a = 6.737	a = 6.620 [113]	16.004
	c = 3.664	c = 3.600 [113]	

The full structural relaxation of Pd₂As was also performed. The experimental lattice parameters were also reported for comparison. Our calculations results gave lattice parameters of a = b = 6.737 Å and c = 3.664 Å, whereas the experimental lattice parameters were found to be a = b = 6.620 Å and c = 3.600 Å. This showed that there is a good agreement between the calculated and experimental lattice parameters, which suggested that computational density functional theory was able to predict the lattice parameters of Pd₂As. The calculations predicted an equilibrium cell volume of 16.004 Å³/atom. Figure 3.6 presented the bulk structures of PtAs₂, PtAsS (CE), PtAsS (VCA) and Pd₂As.

3.4.2 Heats of formation

The heats of formation (ΔH_f), which is the enthalpy change when one mole of a compound is formed from the elements in their stable states are extremely important in determining structural stabilities of different crystal structures. The lower the heat of formation the more stable is the structure. Furthermore, the heats of formation were calculated by subtracting the elemental total energies from that of the compound. For example, PtAsS can be calculated as:

$$\Delta H_f(PtAsS) = \frac{1}{N} [E_{PtAsS} - (E_{Pt} + E_{As} + E_S)] \quad 3.1$$

where, N is the total number of atoms in the unit cell, E is the total energy of the system PtAsS. E_{Pt} , E_{As} and E_S are the elemental total energies of platinum, arsenic and sulphur, respectively. The same was performed for PtAs₂ and Pd₂As bulk structures.

Table 3.4: The calculated heats of formation (ΔH_f) for PtAs₂, PtAsS (CE), PtAsS (VCA) and Pd₂As structures.

Structure	Heats of formation ΔH_f (eV/atom) Calculated
PtAs ₂	-4.751
PtAsS (CE)	-1.286
PtAsS (VCA)	-2.161
Pd ₂ As	-4.041

The calculations were performed using optimized lattice constants in the framework of VASP code for PtAs₂, PtAsS (CE) and Pd₂As structures. The CASTEP code was used for the solid solution PtAsS (VCA) structure. We observed that the heats of formation calculations divulge that all structures have negative heats of formation. We found that PtAs₂ gave the lowest heat of formation energy (most negative) of -4.751 eV/atom. Most interestingly, PtAsS (CE) was less stable than PtAsS (VCA). This have shown that the binary phase solid solution is more stable than the cluster expansion. The heats of formation values suggested that PtAs₂ structure was the most stable i.e. energetically favourable than PtAsS. The PtAsS (VCA) and Pd₂As structures were intermediately metastable. The stability trends for these cubic systems are summarized as follows: PtAs₂ > PtAsS (VCA) > PtAsS (CE) as shown in Table 3.4.

3.5 Elastic properties

The calculations of elasticity are paramount for gaining insights into mechanical stability and elastic properties of materials. The elastic constants and moduli of sperrylite (PtAs₂), platarsite (PtAsS) and palladoarsenide (Pd₂As) structures were investigated, in order to obtain the relationship between the transformation behaviour and elastic constants. The elastic constants, the bulk modulus (B), tetragonal shear modulus (C'), isotropic shear modulus (G) and Young's modulus (E) were calculated and are all shown in Table 3.5 for PtAs₂ and PtAsS, Table 3.6 and 3.7 for Pd₂As. Furthermore, the anisotropic factor (A), Poisson's ratio (ν), the bulk to shear (B/G) and the Cauchy pressure $C_{12} - C_{44}$ were calculated.

A cubic crystal has only three independent elastic constants (C_{11} , C_{12} and C_{44}). The mechanical stability criteria of a cubic system are given as follows [114]: $C_{11} > 0$, $C_{12} > 0$, $C_{11} - C_{12} > 0$, $C_{44} > 0$, $C_{11} + 2C_{12} > 0$ and $C_{11} > \text{Bulk} > C_{12}$. On the other hand, the Born mechanical stability criteria for monoclinic system [84] are given by:

$$[C_{11} + C_{22} + C_{33} + 2(C_{12} + C_{13} + C_{23})] > 0, (C_{33}C_{55} - C_{35}^2) > 0, (C_{44}C_{66} - C_{46}^2) > 0,$$

$$(C_{22} + C_{33} - 2C_{23}) > 0, [C_{22}(C_{33}C_{55} - C_{35}^2) + 2C_{23}C_{25}C_{35} - C_{23}^2C_{55} - C_{25}^2C_{33}] > 0,$$

$$\{2[C_{15}C_{25}(C_{33}C_{12} - C_{13}C_{23}) + C_{15}C_{35}(C_{22}C_{13} - C_{12}C_{23}) + C_{25}C_{35}(C_{11}C_{23} - C_{12}C_{13})] - [C_{15}^2(C_{22}C_{33} - C_{23}^2) + C_{25}^2(C_{11}C_{33} - C_{13}^2) + C_{35}^2(C_{11}C_{22} - C_{12}^2)] + gC_{55}\} > 0, \quad 3.2$$

$$g = C_{11}(C_{22}C_{33} - C_{11}C_{23}^2 - C_{22}C_{13}^2 - C_{33}C_{12}^2 + 2C_{12}C_{13}C_{23}), [85]$$

Table 3.5: The elastic constants, bulk modulus (B), tetragonal shear modulus (C'), isotropic shear modulus (G), Young's modulus (E), anisotropic factor (A), Poisson's ratio (ν), bulk to shear modulus (B/G) and Cauchy pressure ($C_{12} - C_{44}$) of PtAs₂, PtAsS (CE) and PtAsS (VCA) structures.

Moduli	PtAs ₂ (GPa)	PtAsS (CE) (GPa)	PtAsS (VCA) (GPa)
C₁₁	299.52	193.30	29.27
C₁₂	52.92	89.35	156.44
C₄₄	69.56	40.51	-75.76
B	135.12	124.00	114.05
C'	123.30	51.98	-63.59
G	87.65	44.76	-70.63
E	216.15	119.87	-266.99
A	0.39	0.78	1.19
V	0.23	0.34	0.89
B/G	1.54	2.77	-1.61
C₁₂ - C₄₄	-16.64	48.84	232.20

Table 3.6: The calculated elastic constants C_{ij} (in GPa) of Pd₂As monoclinic structure.

Phases (GPa)	C ₁₁	C ₁₂	C ₁₃	C ₁₅	C ₂₂	C ₂₃	C ₂₅	C ₃₃	C ₃₅	C ₄₄	C ₄₆	C ₅₅	C ₆₆
Pd ₂ As	191.50	137.56	124.87	0.00	191.50	124.87	0.00	147.93	0.00	24.52	0.00	24.52	26.97

The cubic systems PtAs₂ and PtAsS (CE) were found mechanically stable since their values of C₁₁, C₁₂ and C₄₄ were all positive and greater than zero. The Pd₂As structure was mechanically stable as well since all the mechanical stability criteria for a monoclinic structure were satisfied. Furthermore, C₁₁, C₂₂, C₃₃, C₁₂, C₁₃, C₂₃, C₄₄, C₅₅ and C₆₆ for Pd₂As were found to be positive, while C₁₅, C₂₅, C₃₅ and C₄₆ for Pd₂As possess values of 0, suggesting stability.

The PtAsS (VCA) structure did not satisfy the necessary conditions of a cubic structure, since C_{11} was much less than C_{12} . In addition, C_{44} and C' were negative and this suggested instability.

From the calculated elastic constants, the mechanical parameters that is the bulk, shear, Young's modulus and Poisson's ratio were determined using the Voigt- Reuss- Hill [86]. The modulus are used to describe the elastic behaviour of materials, and were found higher for PtAs₂, PtAsS (CE) and Pd₂As structures. In addition, the PtAsS (VCA) showed negative values of shear and Young's modulus.

Table 3.7: Summarized the bulk (B), shear (G) and Young's modulus (E), Poisson's ratio (ν), Cauchy pressure ($C_{12} - C_{44}$) and the shear anisotropic factors (A_1 , A_2 and A_3) of the monoclinic Pd₂As.

Phases (GPa)	B	G	E	B/G	ν	$C_{12} - C_{44}$	A_1	A_2	A_3
Pd ₂ As	142.26	24.56	69.66	5.79	0.42	113.04	1.09	1.09	1.00

Pugh introduced the ratio of bulk to shear modulus (B/G) of a material, which expresses that the shear and bulk moduli signifies the resistance to deformation of plastic and a resistance to fracture [78]. A higher B/G value than 1.75 is associated with ductility, whereas a lower value represented brittleness [78]. Our results showed that the B/G ratio for PtAs₂, PtAsS (CE), solid solution PtAsS (VCA) and Pd₂As are 1.54, 2.77, -1.61 and 5.79, respectively. This showed that the PtAsS (CE) and Pd₂As were all ductile because of the highest values of B/G , with the Pd₂As structure being more ductile. The PtAsS (VCA) and PtAs₂ were brittle since they had a low B/G values.

As it can be seen from the Table 3.5 and 3.7, for all the examined system the values of the bulk modulus B were found greater than the isotropic shear modulus G . This implied that the parameter limiting the mechanical stability of these structures was the shear modulus. In the cubic system, the bulk modulus and shear modulus predicted that the PtAs₂ was the hardest material, since it had the highest values. In addition, the monoclinic Pd₂As had the superior bulk modulus indicating that it was the hardest material but having less value of shear modulus. The stiffness level of a material was described by the resistance force against distortion (i.e. stress to strain) using the Young's modulus, i.e. if the value of E is larger, the material is considered to be stiffer. The calculated Young's modulus indicated that PtAs₂ was much stiffer, since it had the largest value of elastic constant (Table 3.5). This suggested that PtAs₂ structure was mechanically stronger as compared to the cubic PtAsS (CE) and PtAsS (VCA) structures.

Another important parameter that correlates with the possibility of the microcracks appearance in material is the elastic anisotropy of crystals [115]. To evaluate the chemical and physical characteristics, it is important to calculate the elastic anisotropy of the crystals. There are various ways to represent elastic anisotropy of a crystal, such as using the calculated values of the elastic constants C_{ij} . A measure of the degree of anisotropy in the bonding between atoms in different planes can be identified by calculating the shear anisotropic factors [116, 117]. However, crystals with isotropic elastic properties of $A = 1$, or greater or smaller than the unity, measures the degree of elastic anisotropy. From the Table 3.5, we showed the calculated anisotropic ratio for PtAs₂ and PtAsS structures. Table 3.7 showed the calculated shear anisotropic factor (A_1 , A_2 and A_3) values of Pd₂As model. These indicated that the structures PtAsS (VCA) and Pd₂As were isotropic elastically since their values are equal or greater than 1. The PtAsS (CE) has a value of 0.78 which is less than 1. The mineral PtAs₂ has the lowest anisotropic factor of 0.39 indicating that its properties are not elastically isotropic.

The types of bonding in a solid can be predicted by knowing the sign of a Cauchy pressure ($C_{12} - C_{44}$). The sign of Cauchy pressure also provides information about the bond sorting. The dominant covalently bonded compounds are negative whereas the dominant ionic bonded compounds are positive [74]. The sperrylite showed covalently bonded compound since the Cauchy pressure ($C_{12} - C_{44} < 0$) was negative. On the other hand, PtAsS structures and Pd₂As predicted an ionic bonds because the Cauchy pressure ($C_{12} - C_{44} > 0$) were positive. The bond sorting can also be found from the value of a Poisson's ratio. For a covalently bonded compounds, the value of the Poisson's ratio is lower than 0.25, while the typical ionic compounds, it is nearly 0.25 or higher [118]. The large Poisson's ratio indicate good plasticity. The calculations showed Poisson's ratio values of $\nu = 0.89, 0.42, 0.34$ and 0.23 for the cubic PtAsS (VCA), monoclinic Pd₂As, cubic PtAsS (CE) and PtAs₂, respectively (see Table 3.5 and 3.7). The values of the Poisson's ratio suggested that PtAsS (VCA), Pd₂As and PtAsS (CE) structures exhibit ionic bonds, but it is noticeable that the poisson's ratio of PtAs₂ phase was 0.23 which indicated a dominant covalent bond. And these results were consistent with the results predicted by the Cauchy pressure sign.

3.6 Vibrational properties of PtAs₂, PtAsS and Pd₂As structures

The vibrational stabilities were carried out using *ab-initio* PHONON code [119]. The vibrational properties of PtAs₂, PtAsS (CE) and Pd₂As structures with respect to the phonon

dispersion and phonon densities of states were analysed. Figure 3.7 displayed the phonon dispersion curve and the phonon partial density of states (PPDOS) for PtAs₂. We observed that there are positive frequencies in all the Brillouin zone directions. The phonon partial density of states showed that platinum (Pt) and arsenic (As) were responsible for positive frequencies (Figure 3.7(b) and 3.7(c)). The acoustic and optical band emanated from the Pt and As atoms contribution. The lower band of acoustic branches were due to the contribution of Pt atom along the x, y and z components, while the upper optical branches were due to As atom mainly along x, y and z directions. In addition, the PtAs₂ structure was stable since no soft modes were observed.

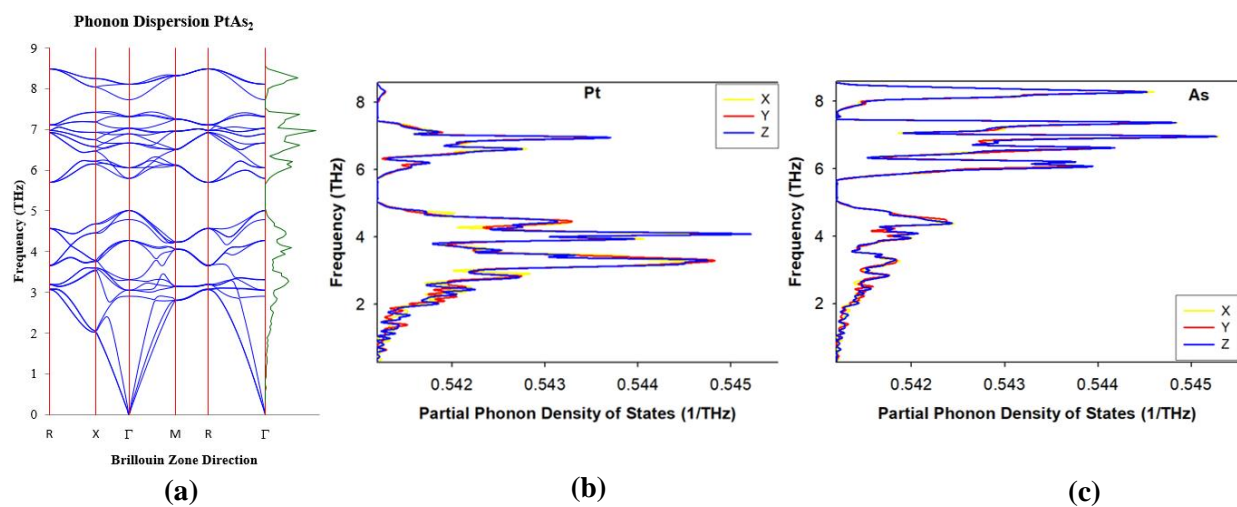


Figure 3.7: (a) Phonon dispersion for PtAs₂, (b) phonon partial density of states for platinum contribution and (c) arsenic contribution. Pt and As contributions towards the vibrations along x, y and z components, respectively.

In Figure 3.8 we showed the phonon dispersion curve of PtAsS (CE), plotted along with the phonon partial density of states depicting the contributions of each atom. However, the phonon dispersion curve and the PPDOS indicated that there were no negative vibrations in all the Brillouin zone directions. The PPDOS showed that the lower bands of the acoustic mode emanated from Pt atoms and the upper optical bands emanated from As and S atoms as shown in Figure 3.8(b), 3.8(c) and 3.8(d). The Pt atoms vibrations in the x, y and z components dominated the acoustic mode, while the As and S atoms vibrations in the x, y and z components dominated the optical modes. Thus the PtAsS (CE) structure was stable since no soft modes were observed.

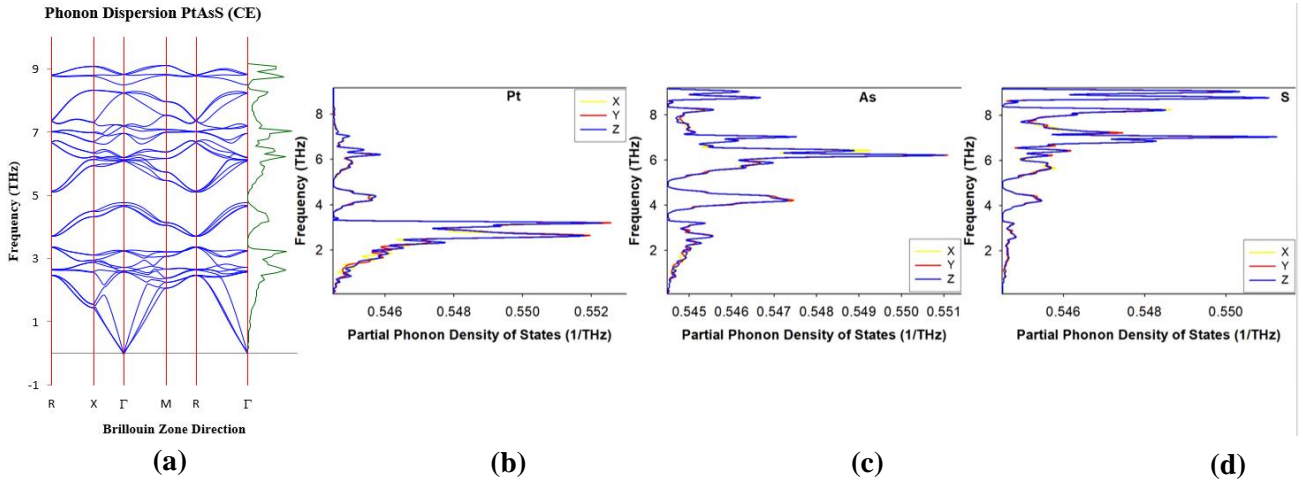


Figure 3.8: (a) Phonon dispersion for PtAsS (CE), (b) phonon partial density of states for platinum contribution, (c) arsenic contribution and (d) sulphur contribution. Pt, As and S contributions towards the vibrations along x, y and z components, respectively.

In Figure 3.9 we showed that the phonon dispersion curve and the PPDOS for the Pd₂As had positive frequencies in all the Brillouin zone directions. The phonon partial density of states showed that the palladium (Pd) and arsenic (As) atoms were responsible for positive frequencies. The As atoms vibrations in the x, y and z components dominated the optical mode and the Pd atoms vibrations in the x, y and z components dominated the acoustic mode (Figure 3.9(b) and 3.9(c)). Thus, the Pd₂As structure was stable since no phonon soft modes were observed in all the Brillouin zone directions.

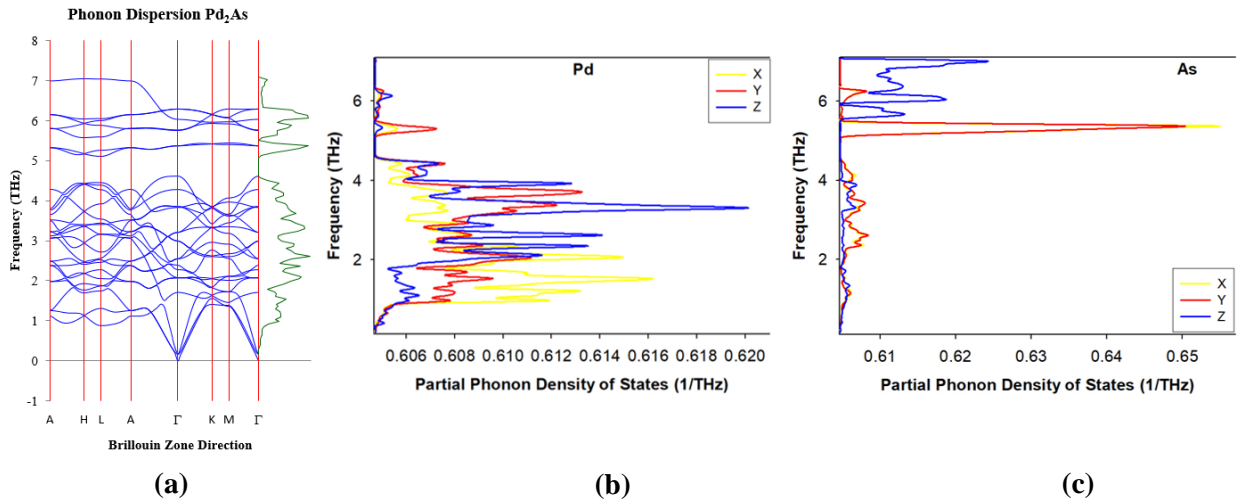


Figure 3.9: (a) Phonon dispersion for Pd₂As, (b) phonon partial density of states for palladium contribution and (c) arsenic contribution. Pd and As contributions towards the vibration along x, y and z components, respectively.

3.7 Summary

In this chapter we have determined the cut-off energy suitable to converge the total energy of the systems to be 500 eV for the bulk PtAs₂, PtAsS and 450 eV for the bulk Pd₂As. The number of k-points mesh of 6x6x6 for (PtAs₂ and PtAsS) and 7x7x14 for Pd₂As were sufficient to converge the bulk structures. We performed the geometry optimization for all the structures to compare their structural properties. The lattice parameters for these systems were allowed to vary, thereby minimizing the structures to their stable form. In addition, the cluster expansion was performed to generate new stable structures for PtAsS structure. The binary ground state diagram showed that all structures had negative heats of formations (ΔH_f), hence they were thermodynamically stable (miscible constituents). Moreover, the cluster expansion showed a greater stability at 50/50 percentage ($x = 0.5$), where As and S atoms are equally distributed in the structure with S-As dimer bond formed at the centre. The probabilistic occupations of each lattice site were selected as: 50% by As, 50% by S for PtAsS (VCA) model. However, in this case two atoms (i.e. S and As) occupied the same lattice position.

It was found that the lattice parameters for the cubic PtAs₂ and PtAsS (CE) were slightly larger, which showed that the GGA-PBE overestimated the lattice parameters. However, for PtAsS (VCA) and Pd₂As, there was a good agreement between the calculated lattice parameters and experimental values. This showed that for PtAsS (VCA) and Pd₂As structures, the DFT was able to predict the lattice parameters. The heats of formation divulge that all the structures have negative heats of formation. In addition, heats of formation values suggested that the PtAsS (VCA) structure was the most stable i.e. energetically favourable than PtAsS (CE).

We evaluated and discussed the elastic constants, the phonon dispersion curves, phonon partial density of states, the density of states and atomic charges for all the structures. The elastic constants for the cubic structures, PtAs₂ and PtAsS and monoclinic structure Pd₂As, the bulk modulus (B), tetragonal shear modulus (C'), isotropic shear modulus (G) and Young's modulus (E) were calculated. Furthermore, the anisotropic factor (A), Poisson's ratio (ν), the bulk to shear (B/G) and the Cauchy pressure ($C_{12} - C_{44}$) were also calculated. The cubic systems PtAs₂ and PtAsS (CE) were mechanically stable since their values of C_{11} , C_{12} and C_{44} were all positive and greater than zero. In addition, Pd₂As structure was mechanically stable since all the mechanical stability criteria for a monoclinic structure were satisfied. The PtAsS (VCA) did not satisfy the necessary conditions of a cubic structure, since C_{11} was much lesser than C_{12} and C_{44} and C' being negative. Our results showed that the PtAsS (CE) and Pd₂As structures were all ductile because of the high values of B/G whereas the PtAsS (VCA) and PtAs₂ were

brittle since they had a low B/G values. The calculated Young's modulus indicated that PtAs₂ was much stiffer than PtAsS structures, since it had the highest value of elastic constant. This suggested that PtAs₂ structure was mechanically stronger among the PtAsS structures. We observed that the PtAs₂ was a dominant covalently bonded compound since the Cauchy pressure ($C_{12} - C_{44} < 0$) was negative. On the other hand, the PtAsS structures and Pd₂As predicted that the ionic bonds were dominant because the Cauchy pressure ($C_{12} - C_{44} > 0$) were positive. This was also confirmed from the Poisson's ratio values, which showed that the PtAsS (CE), PtAsS (VCA) and Pd₂As structures exhibited ionic bonds, but it was noticeable that the Poisson's ratio of PtAs₂ phase was 0.23, which indicated a dominant covalent bonds.

The phonon dispersion curve and the phonon partial density of states (PPDOS) for PtAs₂, PtAsS (CE) and Pd₂As had no negative frequencies (soft modes) along the gamma direction, this suggested stability.

CHAPTER 4

4. Surface modelling of PtAs₂, PtAsS and Pd₂As

In this chapter we discussed the DFT results of the surface model relaxation and their surface properties for PtAs₂, PtAsS and Pd₂As models. Firstly, the k-point variation for the surfaces were performed. Secondly, the computational details are then given for the surfaces. We determined the stable surface termination and vary the slab thickness for the surfaces. The supercell surfaces are then constructed and the most stable surfaces for all the models were used to calculate the equilibrium morphologies. We also compared the three low index surfaces, ((100), (110) and (111)) for surface stability. The bulk systems and working surfaces are analysed and their electronic structures were presented. Lastly, we discussed the density of states (DOS) and Bader analysis for PtAs₂, PtAsS and Pd₂As structures

4.1 Surface k-point convergence

In a plane-wave DFT surface calculations, a number of parameters have an effect on the overall accuracy of the calculation. The convergence of the total energy was assessed with respect to the number of k-points used to sample the Brillouin zone. We presented a set of rules regarding the choice of k-point grid, integration method to achieve numerical convergence of surface energies at minimal computational costs. The basis transformed surface slab calculation proposed in this work calculated surface energies using 4x4x1 k-point mesh for PtAs₂, PtAsS and 5x3x1 k-point mesh for Pd₂As surfaces (Figure 4.1).

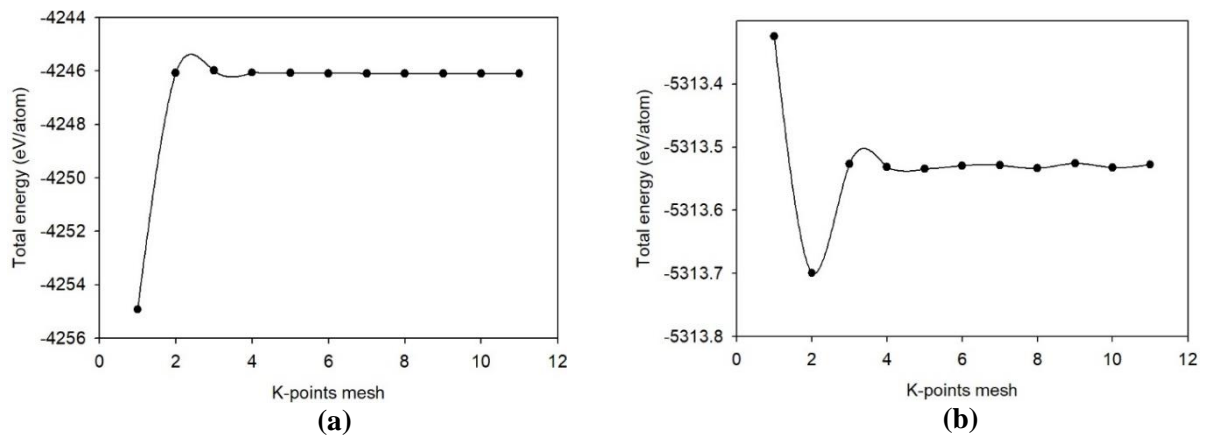


Figure 4.1: Total energy against k-points mesh (a) cubic PtAs₂ and PtAsS surfaces (b) monoclinic Pd₂As surface structures.

4.2 Surface computational methods

We have employed the VASP and CASTEP DFT codes using the plane-wave with generalized gradient approximation of Perdew-Burke-Ernzerhof (GGA-PBE) [50] exchange-correlation functional. The plane-wave basis set with an energy cut-off of 450 and 500 eV for PtAs₂, PtAsS and Pd₂As were set, which demonstrated convergence to within 0.2 meV/atom. The projector augmented wave (PAW) pseudopotentials for the electron-ion interaction [65] were employed and the electron configurations considered are: [Xe]4f¹⁴5d⁹6s¹ for Pt, [Kr]4d¹⁰ for Pd, [Ar]3d¹⁰4s²4p³ for As and [Ne]3s²3p⁴ for S atom. Most importantly, for all the geometry optimization of the surfaces, a k-point grid of 4x4x1 for PtAs₂ and PtAsS and 5x3x1 for Pd₂As surface structures were generated using the Monkhorst-Pack scheme [60]. The size of the k-point grid used for mineral represents a k-point sampling spacing 0.25 Å⁻¹. The convergence tolerances for force, ionic displacement and energy were 0.02 eVÅ⁻¹, 0.015 Å and 0.01 meV/atom, respectively. The vacuum height for all surface models in this chapter was set to 20.00 Å in order to avoid the interaction of the long adsorbate with the upper repeating slab model. Throughout this work model total energies (in J/m²) will be quoted to 3 decimal places to allow for future in-depth model comparison and optimisation by other researchers.

To ensure that the results of the calculations accurately represents an isolated surface, the vacuum regions must be wide enough. This is because the faces of adjacent crystal slabs do not interact across the vacuum region, and the crystal slab must be thick enough so that the two surfaces of each crystal do not interact through the bulk crystal. However, it is important to test the convergence of a vacuum width and slab thickness. As a compromise between computation efficiency and accuracy, (100), (110) and (111) surfaces are considered.

In the next section we investigated different surface termination and surface layers since the thickness of a surface slab is crucial during adsorption. We have constructed different terminations, slab thickness and layers for sperrylite, platarsite and palladoarsenide structures. Their surface energies were calculated and considered the most stable surface with the lowest positive surface energy (less reactive). The surface terminations for all structures were fully prepared using Material Studio software and considering all mixed and pure metal terminations.

4.3 Sperrylite (PtAs₂)

4.3.1 Surface terminations

We tested the different surface terminations for PtAs₂ model and we considered the most stable termination with the lowest positive surface energy (less reactive) as this has an effect during adsorption. This was because a very reactive surface may not give a thermodynamically behaviour of the mineral surface. In addition, we cleaved the mineral along the low-miller index planes (100), (110) and (111).

We generated the total of 11 different surface terminations on PtAs₂ mineral, 3 for (100) and (110) and 5 for (111) surface as shown in Figure 4.2. The un-relaxed surfaces are shown in Figure 4.2, Term.1 is Pt-terminated, Term.2 and Term.3 are As-terminated. Term.2 was found the most stable since it had the lowest positive surface energy of 1.171 J/m². For (110) surface, the Term.1 is a Pt and As mix termination, while Term.2 and Term.3 are As-terminated. The Term.2 was found having the lowest surface energy (2.501 J/m²), which suggested stability (see Table 4.1). The (111) surface terminations are shown in Figure 4.2, the Term.1 is Pt-terminated, while Term.2, 3, 4 and 5 are As-terminated. The Term.3 for (111) surface was observed the most stable surface termination (less reactive) since it had lowest positive surface energy (1.662 J/m²). It is clear from Table 4.1 that the (100) surface display the lowest surface energy amongst all the surfaces which indicated that it is the most stable surface. The dominant phase of the (100) PtAs₂ surface had been previously observed from crystal morphologies, computationally [108, 120].

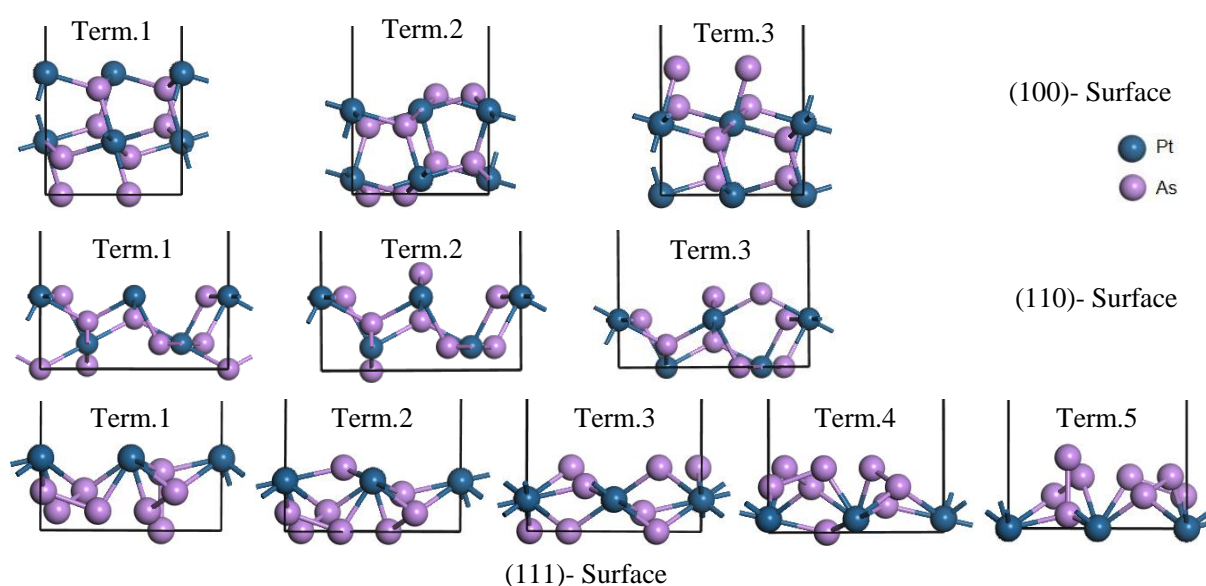


Figure 4.2: Shows 11 different surface terminations along the three low MI planes (100), (110) and (111) for PtAs₂.

Table 4.1: Different terminations, number of atoms, number of layers, total energy and surface energy for (100), (111) and (110) PtAs₂ surfaces.

(100) surface				
Terminations slab	Number of atoms on slab	Number of layers	Total energy (slab) (eV)	Surface energy (J/m ²) Unrelaxed
Term.1	12	6	-61.5319	1.397
Term.2	12	6	-62.5371	1.171
Term.3	12	6	-61.5319	1.397
(111) surface				
Term.1	12	5	-50.9329	1.891
Term.2	12	5	-52.4572	1.719
Term.3	12	5	-52.9793	1.662
Term.4	12	5	-52.4572	1.719
Term.5	12	5	-50.9329	1.891
(110) surface				
Term.1	12	5	-51.7407	2.546
Term.2	12	5	-52.0229	2.501
Term.3	12	5	-51.7407	2.546

4.3.2 Slab thickness determination

We have investigated different surface layers and slab thickness within the low-Miller index plane (100), (110) and (111). For (100) surface, we started from six layers (6L) increasing by 3 layers at a time, where 6L, 9L, 12L and 15L were varied for this surface as presented in Figure 4.4, which also present the un-relaxed surface slabs. The (110) surface had started from seven layers (7L) whereby increasing by 2 layers, thus, 7L, 9L, 11L, 13L and 15L were obtained. Lastly, the (111) surface were varied starting from ten layers (10L) increasing by 5 layers, therefore having 10L, 15L and 20L. Table 4.2 shows the surface energies of (100), (111) and (110) PtAs₂ surfaces. We observed that the surface energies increased with increasing slab thickness. The slab depth (number of layers) and the surface energies of the three low MI planes (100), (110) and (111) are shown in Table 4.2 and the plot of total energy against slab depth is shown in Figure 4.3.

Table 4.2: Surface layers convergence of (100), (111), and (110) surface slab, number of atoms per slab, total energy (eV) and surface energies (J/m^2) for PtAs_2 .

Surface slab	Number of atoms on slab	Number of layers	Total energy (slab) (eV)	Surface energy (J/m^2) Unrelaxed
(100)	12	6L	-59.5371	1.846
	18	9L	-87.6849	3.134
	24	12L	-109.2913	5.895
	30	15L	-150.6426	4.211
(111)	24	10L	-103.3057	3.619
	36	15L	-155.5796	5.361
	48	20L	-208.4783	7.030
(110)	18	7L	-76.8826	3.935
	24	9L	-103.2465	5.130
	30	11L	-129.4995	6.342
	36	13L	-155.9845	7.518
	42	15L	-182.4699	8.692

Previously, Boettger [121] reported that the surface energies will diverge for increasing slab depths unless the energy of the bulk is exactly equals the difference in total energies between a slab of depth N and a slab of depth $N-1$. This is the total energy gain by adding extra layer is equivalent to the energy of the bulk, normalised for the number of atoms gained per layer. The total energy of the bulk which was calculated to be -67.7415 eV never matches the energy difference in Table 4.2. This imply that there is an increasing linear divergence of the surface energies. The (100) surface had the lowest surface energy amongst all the surfaces, thus most stable. For all surfaces, the fifteen layers (15L) slab thickness were considered as thick enough for adsorption. All the number of atoms on the slabs, number of layers, total energies and surface energies for each of these three surfaces are presented in Table 4.2.

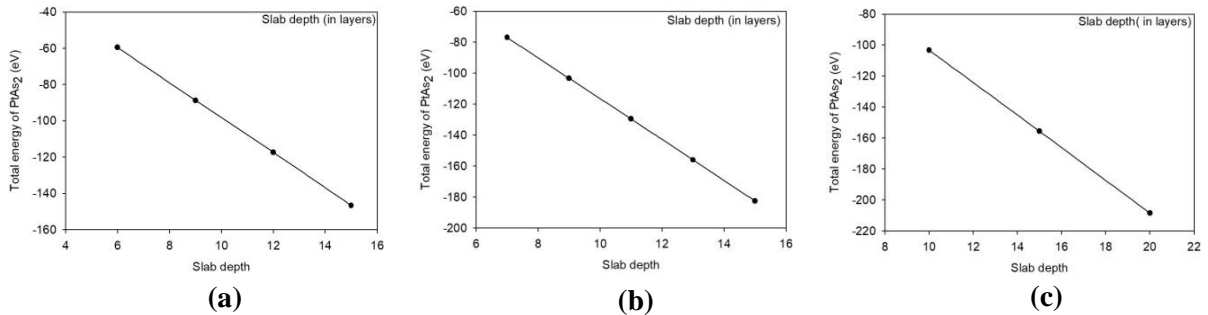


Figure 4.3: Slab depth vs total energy plot for PtAs_2 . (a) The most stable (100), (b) the least stable (110) and (c) the (111) the moderate stable surfaces.

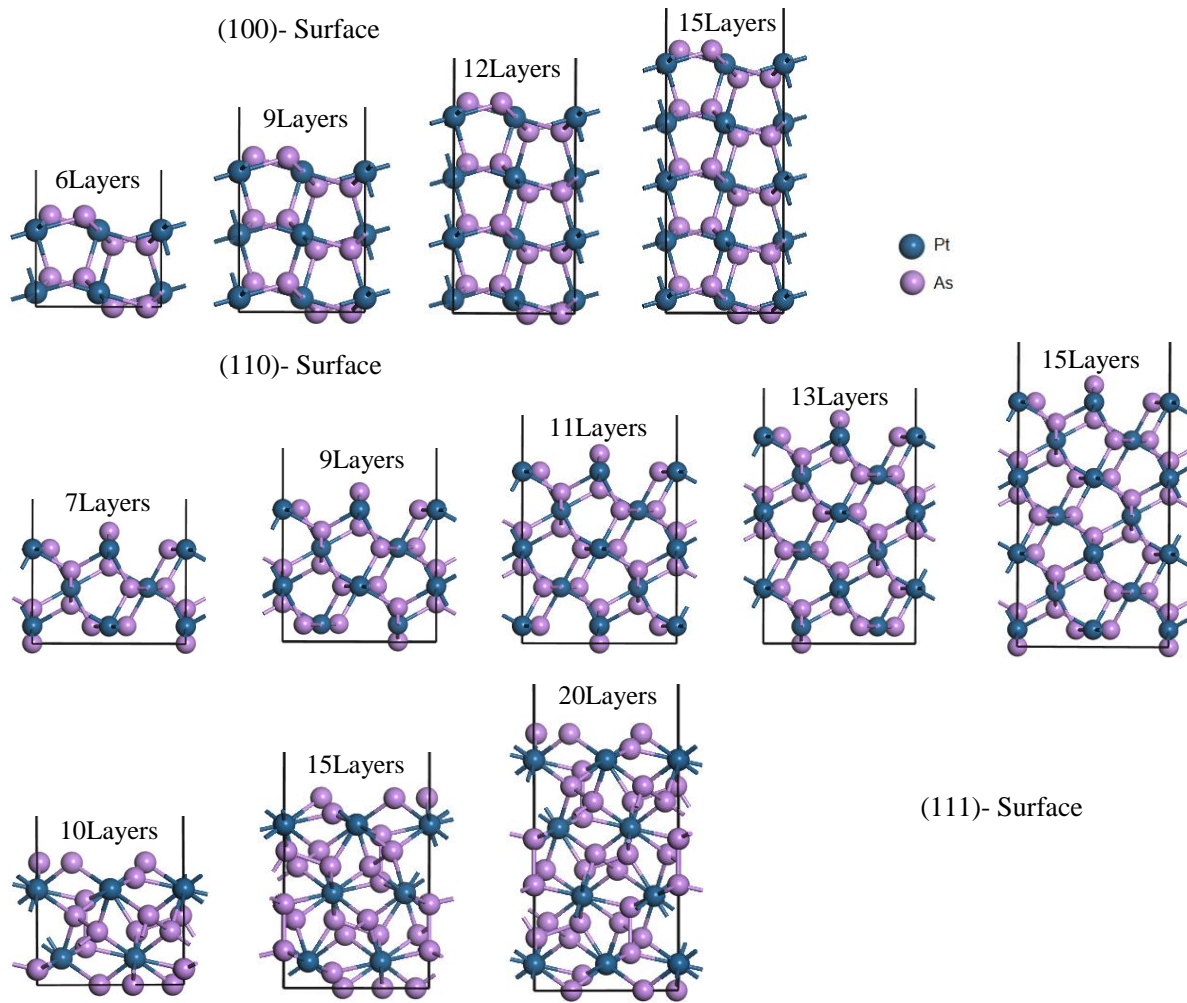


Figure 4.4: The un-relaxed structures of surface layers convergence for PtAs₂ along the low MI plane (100), (110) and (111).

Table 4.3: Supercell optimization of (100), (111), and (110) surface layers convergence, number of atoms per slab, total energy (eV) and surface energies (J/m²) for PtAs₂ system.

Surface slab	Number of atoms on slab	Number of layers	Total energy (slab) (eV)	Surface energy (J/m ²) Relaxed
(100)	120	15	-659.2347	1.045
(111)	144	15	-764.7684	1.367
(110)	168	15	-912.3929	1.453

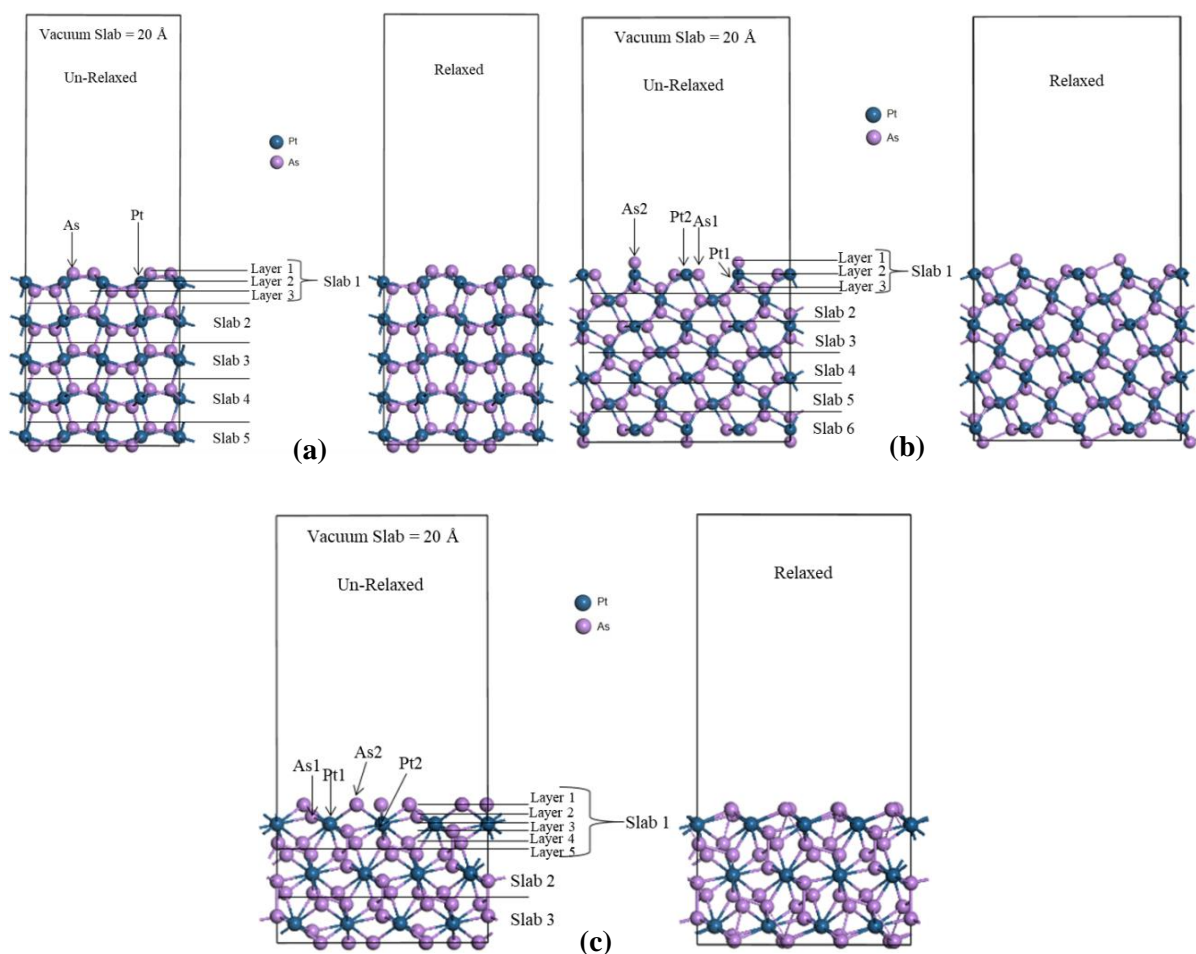


Figure 4.5: The un-relaxed and relaxed supercell structures of surface layers convergence for PtAs₂, (a) (100), (b) (110) and (c) (111) surface.

The 15L slab was used to create a 2x2 supercell structures for all the studied surfaces. The supercell surfaces were relaxed allowing the only the atomic position to relax. Furthermore, the relaxation was performed with the bottom 3 slab for (100) and (110) surfaces fixed to the bulk coordination, while for (111) the bottom slab (5L) was frozen. The (100) surface had the lowest surface energy amongst all the surfaces, thus more stable and considered working surface. Table 4.3 shows the supercell surface results after optimization. The order of surface stability followed as: (100) > (111) > (110) for PtAs₂ structure. Figure 4.5(a), 4.5(b) and 4.5(c) showed all the un-relaxed and relaxed supercell structures for (100), (110) and (111) surfaces.

4.3.3 Analysis of the working surfaces

A thorough appreciation of the mineral surface is required in order to understand the collector binding environment. The exposed sperrylite working surface consists of ridges of As atoms, with Pt atoms inhabiting the clefts between ridges, as shown in Figure 4.6. Most importantly, when considering the binding of bridging ligands such as xanthates, which can

interact with two surface metals simultaneously is the distance between the metal sites. In the sperrylite working surface, the surface inter-platinum distance is 4.289 Å as shown in Figure 4.6. Considering the As lone pairs, it is unlikely that bridging ligands can interact with two Pt atoms in different clefts simultaneously, due to the implicit high steric strain. Similar surfaces has been reported by Waterson *et al.* [108].

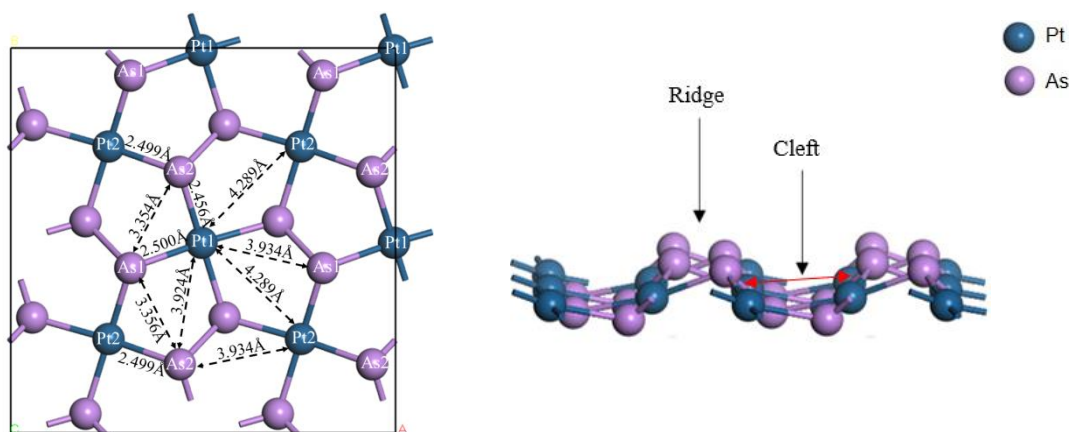


Figure 4.6: Top-view (left) and side view (Right) of the top three layers (3L) on 2x2 supercell working surface of (100) sperrylite surface. Showing raised As ridges and Pt atoms inhabiting the clefts between ridges (Right), with the resulting bond distances (Left).

4.4 Platarsite (PtAsS) cluster expansion

4.4.1 Surface terminations

Different surface terminations of PtAsS (CE) structure were fully discussed. We cleaved the minerals along the three low MI planes (100), (110) and (111). Cleaving along the low MI planes and generated one model apiece for each possible terminations produces the total of 11 different surface terminations on PtAsS (CE) mineral, 3 for (100) and (110) surface and 5 for (111) surface as shown in Figure 4.7.

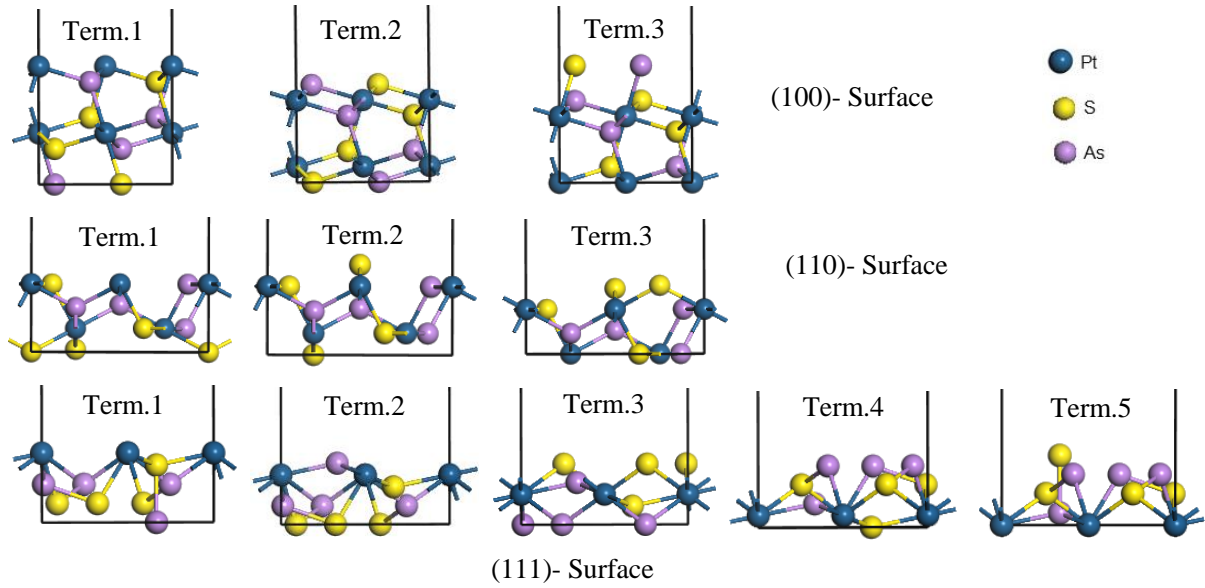


Figure 4.7: Shows 11 different surface terminations along the three low MI planes (100), (110) and (111) for PtAsS (CE) structure.

For (100) surface, Term.1 is Pt-terminated while, Term.2 and Term.3 are As/S mix termination. Term.2 showed the most stability since it has the lowest positive surface energy of 0.580 J/m^2 . For (110) surface, Term.1 is Pt/As/S mix termination while, Term.2 and Term.3 are S-terminated. The Term.2 was found having the lowest surface energy (0.925 J/m^2) which suggested stability (see Table 4.4).

Table 4.4: Different terminations, number of atoms, number of layers, total energy and surface energy for (100), (111) and (110) surfaces for the structure PtAsS (CE).

(100) surface				
Terminations slab	Number of atoms on slab	Number of layers	Total energy (slab) (eV)	Surface energy (J/m^2) Unrelaxed
Term.1	12	6	-56.0186	1.716
Term.2	12	6	-61.1344	0.580
Term.3	12	6	-56.0185	1.716
(111) surface				
Term.1	12	5	-51.5871	1.349
Term.2	12	5	-55.9460	0.865
Term.3	12	5	-54.8489	0.987
Term.4	12	5	-53.8922	1.094
Term.5	12	5	-51.9825	1.306
(110) surface				
Term.1	12	5	-57.3738	0.999
Term.2	12	5	-57.8528	0.925
Term.3	12	5	-57.3738	0.999

The (111) surface terminations as shown in Figure 4.7, displayed that the Term.1 is Pt-terminated, while Term.2, Term.4 are As-terminated, with Term.3 and Term.5 being S-terminated. The Term.2 for (111) surface was found the most stable surface termination, since it had the lowest positive surface energy value of 0.865 J/m^2 . The (100) surface displayed the lowest surface energy amongst all the surfaces which indicated that it is the most stable surface.

The dominant phase of the stable (100), (111) and (110) PtAsS (CE) surfaces had been previously studied from crystal morphologies, computationally [120].

4.4.2 Slab thickness determination

We investigated different surface layers and slab thickness within the (100), (110) and (111) surfaces in a similar manner as for sperrylite. The trends for the total energy against slab thickness are shown Figure 4.8. We observed that as the slab thickness increased, the surface energy also increased. Also for this case the total energy of the bulk calculated as -63.7475 eV did not quite match the energy difference in Table 4.5. This imply that there is an increasing linear convergence of the calculated surface energies. The (100) surface had the lowest surface energy amongst the three surfaces, thus most stable. For all the surfaces, the 15L slab thickness were considered as thick enough for adsorption. For PtAsS (CE) model, the number of atoms on the slabs, number of layers, total energies and surface energies for each of these three surfaces are shown in Table 4.5.

Table 4.5: Surface layers convergence of (100), (111) and (110) surface, number of atoms per slab, total energy (eV) and surface energies (J/m^2) for PtAsS (CE) structure.

Surface slab	Number of atoms on slab	Number of layers	Total energy (slab) (eV)	Surface energy (J/m^2) Unrelaxed
(100)	12	6L	-61.1344	0.580
	18	9L	-93.7097	0.425
	24	12L	-125.9202	0.349
	30	15L	-157.9261	0.319
(111)	24	10L	-119.0567	0.936
	36	15L	-183.5603	0.852
	48	20L	-247.7453	0.804
(110)	18	7L	-88.9442	1.048
	24	9L	-122.3363	0.809
	30	11L	-153.2204	0.965
	36	13L	-186.5579	0.735
	42	15L	-217.3293	0.908

A 2x2 supercell for the PtAsS (CE) surface was required to permit ligand interactions, otherwise inter-ligand steric interactions may begin to have a significant effect. To this end, the work proceeded with the 15-layers (100), (110) and (111) surfaces. The supercell surfaces were relaxed allowing the atomic position to relax. Further relaxation was performed with the bottom 3 slabs for (100) and (110) fixed to the bulk coordination, while for (111) the bottom slab was frozen.

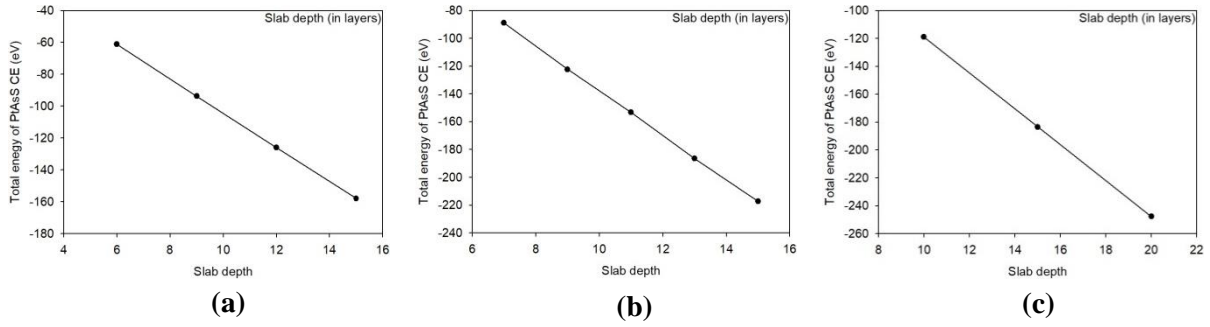


Figure 4.8: Slab depth vs total energy plot for PtAsS (CE). The most stable (100), (b) the least stable (110) and (c) the moderate stable (111) surfaces.

Table 4.6: Supercell optimization of (100), (111), and (110) surface layers convergence, number of atoms per slab, total energy (eV) and surface energies (J/m^2) for PtAsS (CE).

Surface slab	Number of atoms on slab	Number of layers	Total energy (slab) (eV)	Surface energy (J/m^2) Relaxed
(100)	120	15	-631.7399	0.559
(111)	144	15	-734.2505	0.998
(110)	168	15	-869.2976	1.149

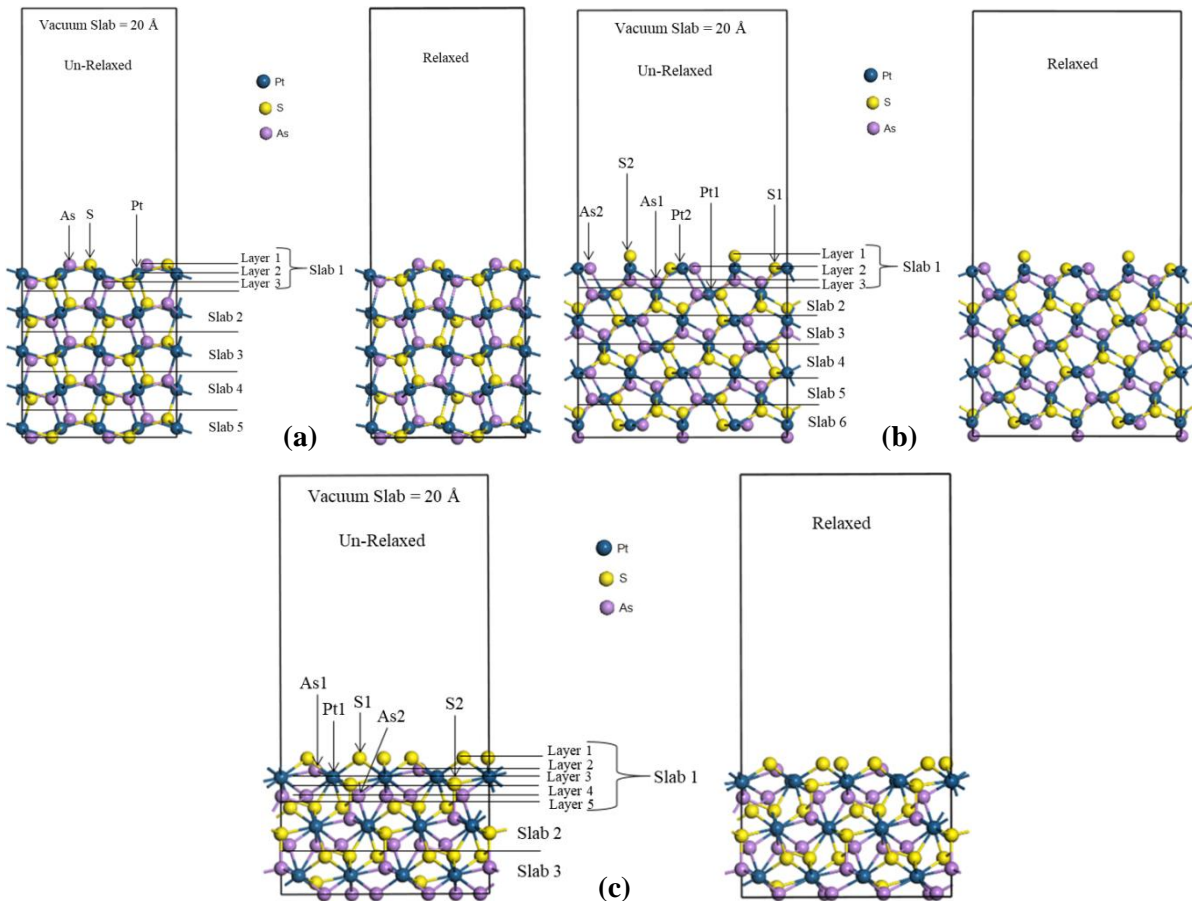


Figure 4.9: The un-relaxed and relaxed supercell structures of surface layers convergence for PtAsS (CE), (a) (100), (b) (110) and (c) (111) surface.

The (100) surface had the lowest surface energy amongst all the surfaces, thus more stable.

Table 4.6 shows the supercell surface results after surface optimization. The order of surface

stability followed as: (100) > (111) > (110) for PtAsS (CE) model. All the un-relaxed and relaxed supercell PtAsS (CE) structures for (100), (110) and (111) surfaces are shown in Figure 4.9(a), 4.9(b) and 4.9(c), respectively.

4.4.3 Analysis of the working surfaces

A thorough appreciation of the mineral surface is required in order to understand the collector binding environment. Similar to the sperrylite, the exposed platarsite (CE) working surface consisted of ridges of S and As atoms, with Pt atoms inhabiting the clefts between ridges, as presented in Figure 4.10. Furthermore, considering the binding of bridging ligands, which can interact with two surface metals simultaneously regarded is the distance between the metal sites. For the PtAsS (CE) working surface, the surface inter-platinum distance is 4.311 Å as shown in Figure 4.10. As such, the As and S lone pairs may cause unlikely bridging of the ligands on the two Pt atoms in different clefts simultaneously, due to the implicit high steric strain.

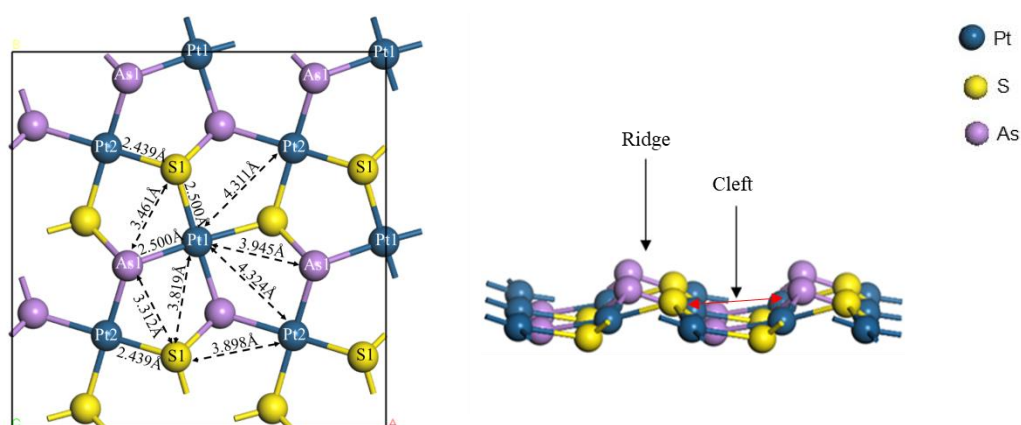


Figure 4.10: Top-view (left) and side view (Right) of the top three layers (3L) on 2x2 supercell working surface of (100) PtAsS (CE) surface. Showing raised As and S ridges and Pt atoms inhabiting the clefts between ridges (Right), with the resulting bond distances (Left).

4.5 Platarsite (PtAsS) VCA

4.5.1 Surface terminations

In this section we discussed the different surface terminations and slab thickness for PtAsS (VCA) model, which are similar to the sperrylite and platarsite (CE). We have tested different surface terminations and considered the most stable termination with the lowest positive surface energy (less reactive). In addition, we cleaved the minerals along the low-miller index

planes (100), (110) and (111). The total of 11 different surface terminations on PtAsS (VCA) were generated, 3 for (100) and (110) surface and 5 for (111) surface. It is clear from Table 4.7 that the (100) surface display the lowest surface energy amongst all the surfaces which indicated that it was the most stable surface.

Table 4.7: Different terminations, number of atoms, number of layers, total energy and surface energy for (100), (111) and (110) surfaces for PtAsS (VCA).

(100) surface				
Terminations slab	Number of atoms on slab	Number of layers	Total energy (slab) (eV)	Surface energy (J/m ²) Unrelaxed
Term.1	12	6	-51.5566	1.452
Term.2	12	6	-57.2345	0.167
Term.3	12	6	-51.5566	1.452
(111) surface				
Term.1	12	5	-48.2910	1.096
Term.2	12	5	-51.9092	0.686
Term.3	12	5	-52.5021	0.618
Term.4	12	5	-51.9092	0.686
Term.5	12	5	-48.2911	1.096
(110) surface				
Term.1	12	5	-53.3247	0.743
Term.2	12	5	-53.2670	0.751
Term.3	12	5	-53.3247	0.743

4.5.2 Slab thickness determination

The PtAsS (VCA) surfaces for different slab thickness were carried out for all the low-Miller index (100), (110) and (111) in a similar manner as the sperrylite and platarsite (CE) structures. We observed that as the slab thickness increased, the surface energy increased as displayed by the total energy against slab thickness in Figure 4.11.

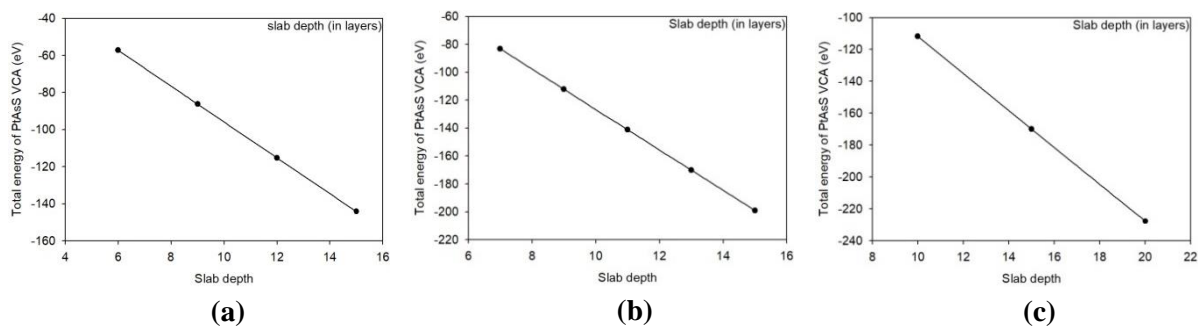


Figure 4.11: Slab depth vs total energy plot for PtAsS (VCA). (a) The most stable (100), (b) the least stable (110) and (c) the moderate stable (111) surfaces.

The total energy of the bulk which was calculated to be -57.9682 eV matched the energy difference and this implies the increasing of linear convergence of the surface energies. The (100) surface had the lowest surface energy amongst the three surfaces, thus most stable and it is a working surface.

Table 4.8: Surface layers convergence of (100), (111) and (110) surfaces, number of atoms per slab, total energy (eV) and surface energies (J/m²) for PtAsS (VCA) mineral.

Surface slab	Number of atoms on slab	Number of layers	Total energy (slab) (eV)	Surface energy (J/m ²) Unrelaxed
(100)	12	6L	-57.2345	0.167
	18	9L	-86.2706	0.154
	24	12L	-115.2644	0.152
	30	15L	-144.1509	0.175
(111)	24	10L	-111.8121	0.466
	36	15L	-169.9296	0.450
	48	20L	-227.7447	0.466
(110)	18	7L	-83.2285	0.596
	24	9L	-112.2228	0.596
	30	11L	-141.1908	0.596
	36	13L	-170.1228	0.606
	42	15L	-199.1089	0.606

For all surfaces, the 15L slab thicknesses were considered as thick enough for adsorption. All the number of atoms on the slabs, number of layers, total energies and surface energies for each of these three surfaces are presented in Table 4.8. The fifteen layer (15L) slab was used to create 2x2 supercell structures. The supercell surfaces were relaxed allowing only the atomic position to relax.

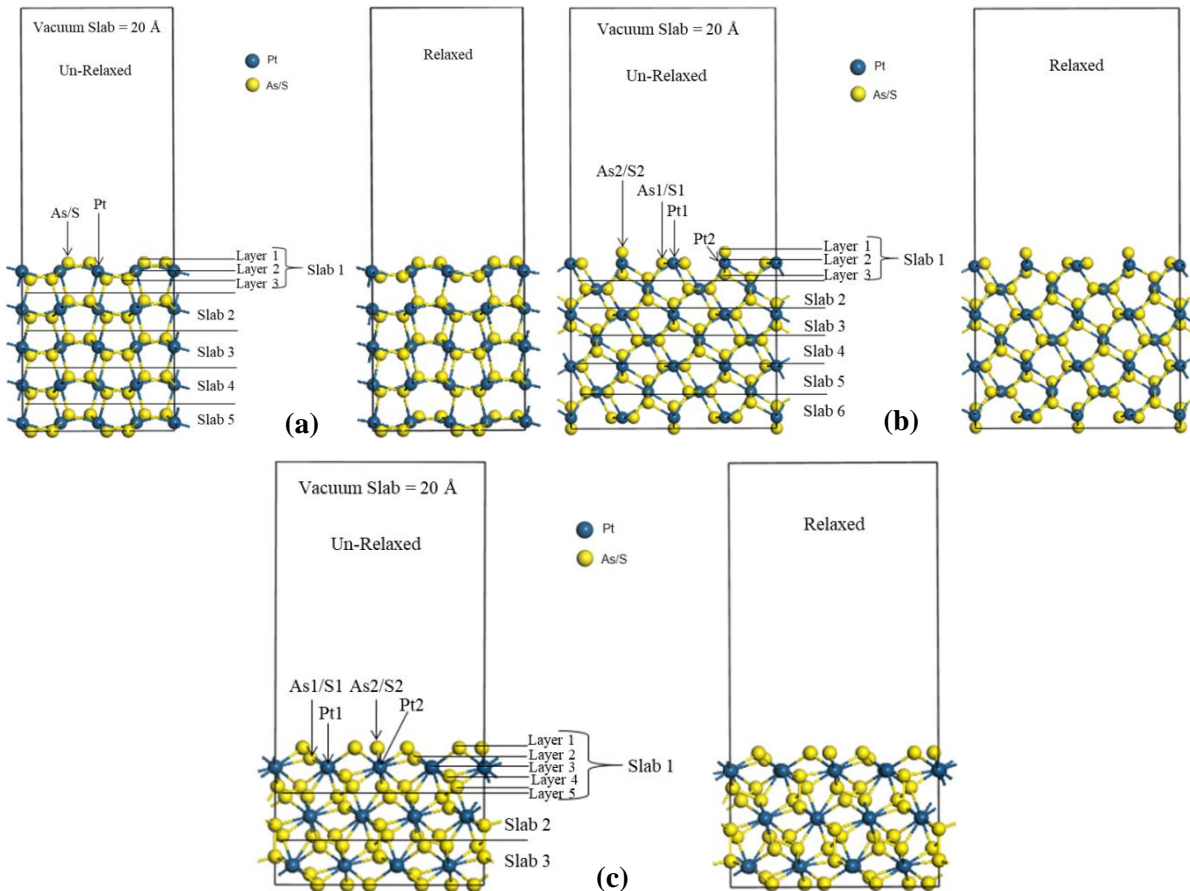


Figure 4.12: The un-relaxed and relaxed supercell structures of surface layers convergence for PtAsS (VCA), (a) (100), (b) (110) and (c) (111) surface.

Further relaxation was performed with the bottom 3 slabs for (100) and (110) fixed to the bulk coordination, while for (111) the bottom slab was frozen. The (100) surface had the lowest surface energy amongst all the surfaces, thus more stable. Table 4.9 shows the supercell surface results after relaxation. The order of surface stability followed as: (100) > (111) > (110) for PtAsS (VCA) mineral. The un-relaxed and relaxed supercell structures for PtAsS (VCA) (100), (110) and (111) surfaces are shown (Figure 4.12(a), 4.12(b) and 4.12(c), respectively).

Table 4.9: Supercell optimization of (100), (111), and (110) surface layers convergence, number of atoms per slab, total energy (eV) and surface energies (J/m²) for PtAsS (VCA) mineral.

Surface slab	Number of atoms on slab	Number of layers	Total energy (slab) (eV)	Surface energy (J/m ²) Relaxed
(100)	120	15	-576.9868	0.213
(111)	144	15	-688.6159	0.236
(110)	168	15	-801.6499	0.457

4.5.3 Analysis of the working surfaces

The PtAsS (VCA) working surface also consisted of ridges of As/S atoms, with Pt atoms inhabiting the clefts between ridges, as shown in Figure 4.13. Considering the binding of bridging ligands, which can interact with two surface metals simultaneously we found that the inter-platinum distance is 4.280 Å. The bridging ligands can interact with Pt atoms in different clefts simultaneously when considering the As/S lone pairs due to the implicit high steric strain.

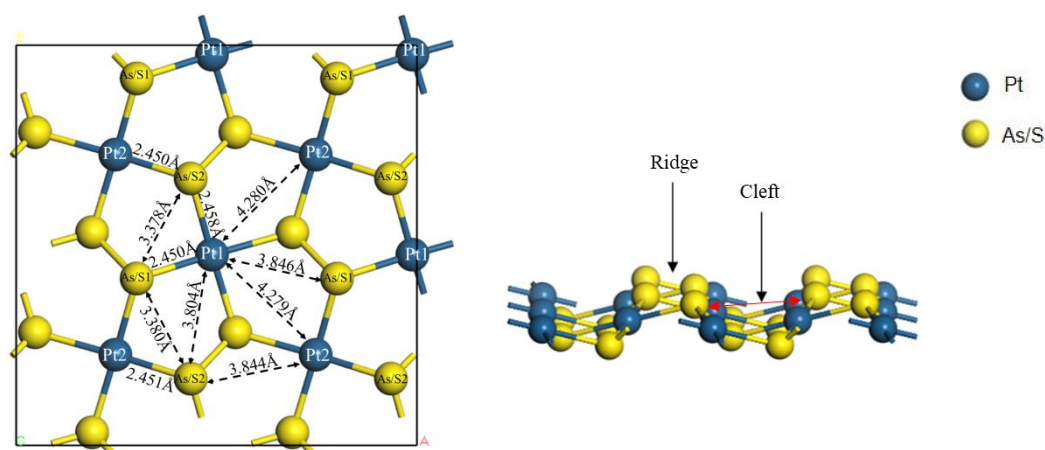


Figure 4.13: Top-view (left) and side view (Right) of the top three layers (3L) on 2x2 supercell working surface of (100) PtAsS (VCA) surface. Showing raised As/S ridges and Pt atoms inhabiting the clefts between ridges (Right), with the resulting bond distances (Left).

4.6 Determination of working surfaces for platarsite (PtAsS)

Table 4.10 shows the bulk and surface coordination and surface energies for the three low Miller index of the PtAsS model i.e. CE and VCA. Comparison of surface energies revealed that the PtAsS (VCA) model gave the lowest surface energies, suggesting that it was more stable than the PtAsS (CE) model.

Table 4.10: Bulk and surface coordination, supercell optimization of (100), (111) and (110) surfaces showing number of atoms per slab and surface energies (J/m^2) for PtAsS systems.

Models	#atoms	Coordination				Surface energies (J/m^2)	
		Pt	As	S	As/S	PtAsS (CE)	PtAsS (VCA)
Bulk	12	6	4	4	4	–	–
(100)	120	5	3	3	3	0.559	0.213
(111)	144	6, 5	3	2	3, 2	0.998	0.236
(110)	168	4	3, 2	3, 2	3, 2	1.149	0.457

The coordination for various atoms changed after cleaving the surface. The Pt atom for the bulk PtAsS was 6-coordinated and after surface cleavage it reduced to 5-coordination for (100) surface and reduced to 6 and 5-coordination for (111) and to 4-coordination for (110) surface. For the As and S atoms, the bulk structure was 4-coordinated, while the (100) and (111) surfaces reduced to 3 and 2-coordination, and for (110) reduced to 3, 2-coordinated for all PtAsS.

4.7 Palladoarsenide (Pd_2As)

4.7.1 Surface terminations

We have cleaved the mineral along the low-miller index planes (100), (110) and (111) and different surface terminations were tested for Pd_2As model and we considered the most stable surface termination with the lowest positive surface energy (less reactive). The surface terminations for Pd_2As structure were prepared by considering all mixed and pure metal terminations. We generated the total of 18 different surface terminations for Pd_2As mineral, that is 7 for (100), 5 for (110) surface and 6 for (111) surface as shown in Figure 4.14. The case of (100) surface, showed that the Term.1 is Pd/As mix terminated, while Term.2,4,5,7 are Pd-terminated and Term.3 and Term.6 are As-terminated. The Term.1 displayed the lowest positive surface energy of 0.833 J/m^2 thus most stability. For (110) surface, Term.1 is As-terminated, while Term.2,3,4 and 5 are Pd-terminated. The Term.4 was found having the lowest surface energy of 1.019 J/m^2 , which suggested stability as presented in Table 4.11. Considering

the (111) surface terminations as shown in Figure 4.14, Term.1 and Term.3 are Pd/As mix terminated, while Term.2 is As-terminated and Term.4,5 and 6 are Pd-terminated. Term.1 for (111) surface was observed the most stable surface termination (less reactive) since it had the lowest positive surface energy of 0.891 J/m².

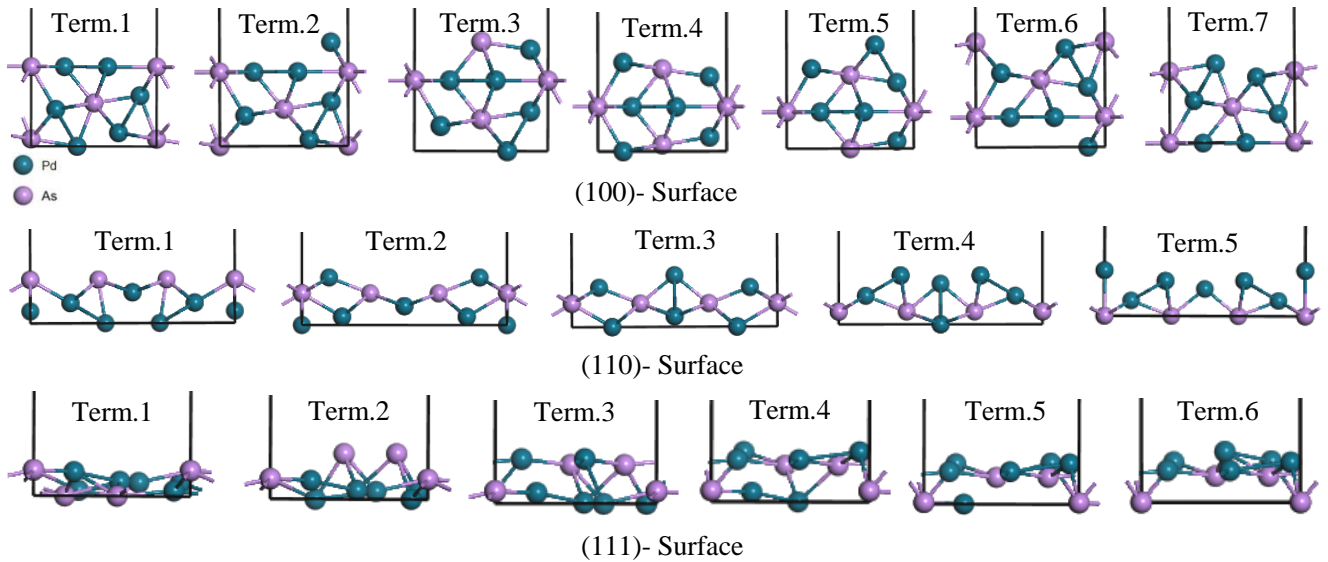


Figure 4.14: Shows 18 different surface terminations along the three low MI planes (100), (110) and (111) for Pd₂As model.

Table 4.11: Different terminations, number of atoms, number of layers, total energy and surface energy for (100), (111) and (110) surfaces for Pd₂As.

(100) surface				
Terminations slab	Number of atoms on slab	Number of layers	Total energy (slab) (eV)	Surface energy (J/m ²) Unrelaxed
Term.1	9	7	-45.8641	0.833
Term.2	9	7	-45.2482	1.038
Term.3	9	7	-45.0574	1.102
Term.4	9	7	-45.8625	0.833
Term.5	9	7	-45.0574	1.102
Term.6	9	7	-45.2483	1.038
Term.7	9	7	-45.8640	0.833
(111) surface				
Term.1	9	5	-41.9887	0.891
Term.2	9	5	-38.8707	1.328
Term.3	9	5	-37.9993	1.452
Term.4	9	5	-38.6185	1.365
Term.5	9	5	-39.7694	1.203
Term.6	9	5	-40.3219	1.125
(110) surface				
Term.1	9	5	-42.6202	1.110
Term.2	9	5	-42.8164	1.072
Term.3	9	5	-42.6035	1.110
Term.4	9	5	-43.0849	1.019
Term.5	9	5	-42.4706	1.139

The Pd₂As was found to have most surface terminations slabs, having dipole. We observed that only the (100) surface (Term.4) and (110) surface (Term.3) had Type 1 and Type 2 combined to give a zero net charge on the surface. Figure 4.15 show the Term.4 for (100) surface and Term.3 for (110 surface) on how the charges cancel and as such these were considered as the working surface terminations. The (111) surface had all the terminations surface slab having dipole. Thus, all surface with dipole require reconstruction.

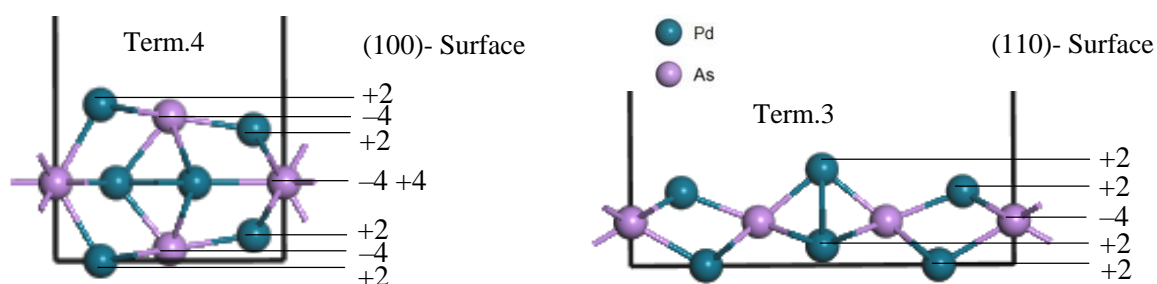


Figure 4.15: Shows surface terminations Type 1 and Type 2 along (100) and (110) surfaces for Pd₂As model.

4.7.2 Slab thickness determination

The Pd₂As different surface slab thickness were carried out for all the low-Miller index (100), (110) and (111). For (100) surface, we started from seven layers (7L) and increase by 7 layers, where 7L, 14L, 21L and 28L were varied as shown in Figure 4.16, (un-relaxed). The (110) surface were varied starting from ten layers (10L), whereby increasing by 5 layers, thus 10L, 15L and 20L for (110) surface as shown in Figure 4.16. Lastly, the (111) surface were varied starting from five layers (5L) increasing by 5 layers, therefore having 5L, 10L, 15L and 20L (Figure 4.16). Table 4.12 shows the surface energies for (100), (111) and (110) Pd₂As surfaces. We observed that the surface energies increased as the slab thickness increased. The total energy against slab thicknesses are shown in Figure 4.17 as depicted in Table 4.12. The total energy of the bulk was calculated to be -48.3383 eV, which matched the energy difference of the first layers. However, the increasing of linear convergence of the surface energies were noted and the number of optimized 2x2 supercell working surfaces with increasing layers were calculated. The (100) surface had the lowest surface energy amongst the three low Miller index, thus most stable and it is considered a working surface. The 21L slab thickness for (100) surface and 15L slab thickness for (110) and (111) surface were considered as thick enough for adsorption.

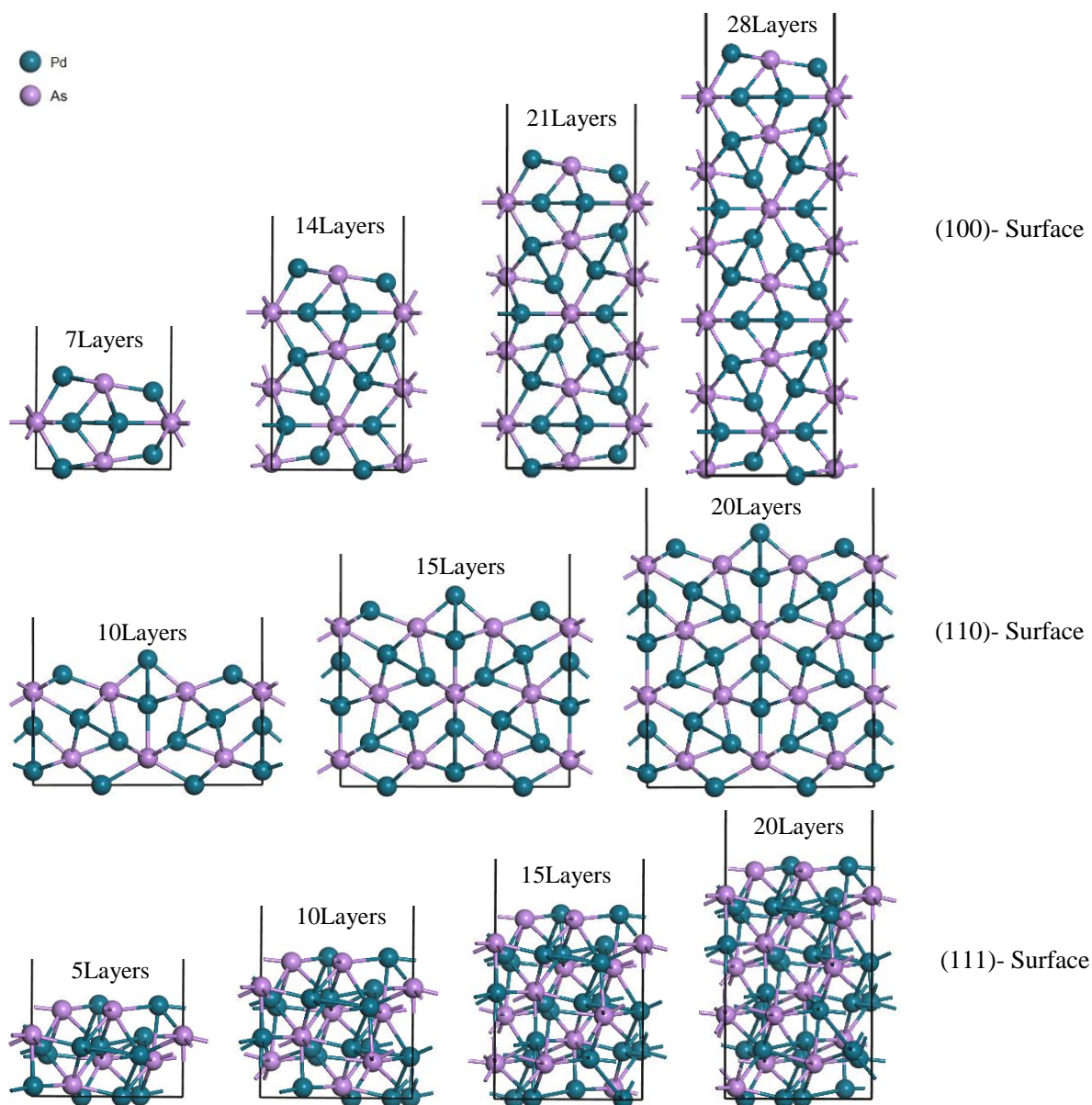


Figure 4.16: The un-relaxed structures of surface layers convergence for Pd₂As along the low MI plane (100), (110) and (111).

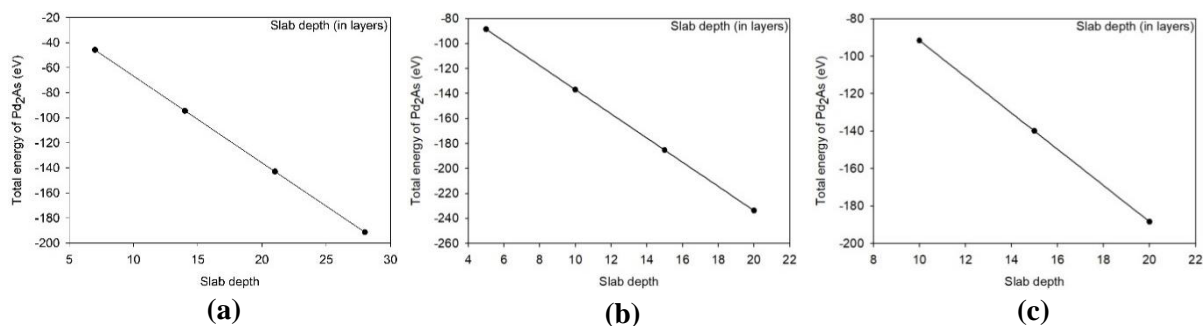


Figure 4.17: Slab depth vs total energy plot for Pd₂As. (a) The most stable (100), (b) the moderate stable (110) and (c) the least stable (111) surfaces.

Table 4.12: Surface layer convergence of (100), (111) and (110) surfaces, number of atoms per slab, total energy (eV) and surface energies (J/m²) for Pd₂As system.

Surface slab	Number of atoms on slab	Number of layers	Total energy (slab) (eV)	Surface energy (J/m ²) Unrelaxed
(100)	9	7L	-45.8625	0.832
	18	14L	-94.3861	0.771
	27	21L	-142.8463	0.729
	36	28L	-191.2873	0.694
(111)	18	5L	-88.5347	1.142
	27	10L	-136.9446	1.142
	36	15L	-185.3089	1.129
	45	20L	-233.7017	1.129
(110)	18	10L	-91.2006	1.062
	27	15L	-139.4895	1.072
	36	20L	-187.7882	1.079

The twenty one layer (21) slab for (100) surface and the fifteen layer (15L) slab for (110) and (111) surface were used to create 2x2 supercell structures. The supercell surfaces were relaxed allowing the atomic position to relax. Further relaxation were performed with the bottom 2 slabs fixed to the bulk coordination and the top slab was allowed to relax for (100) surface.

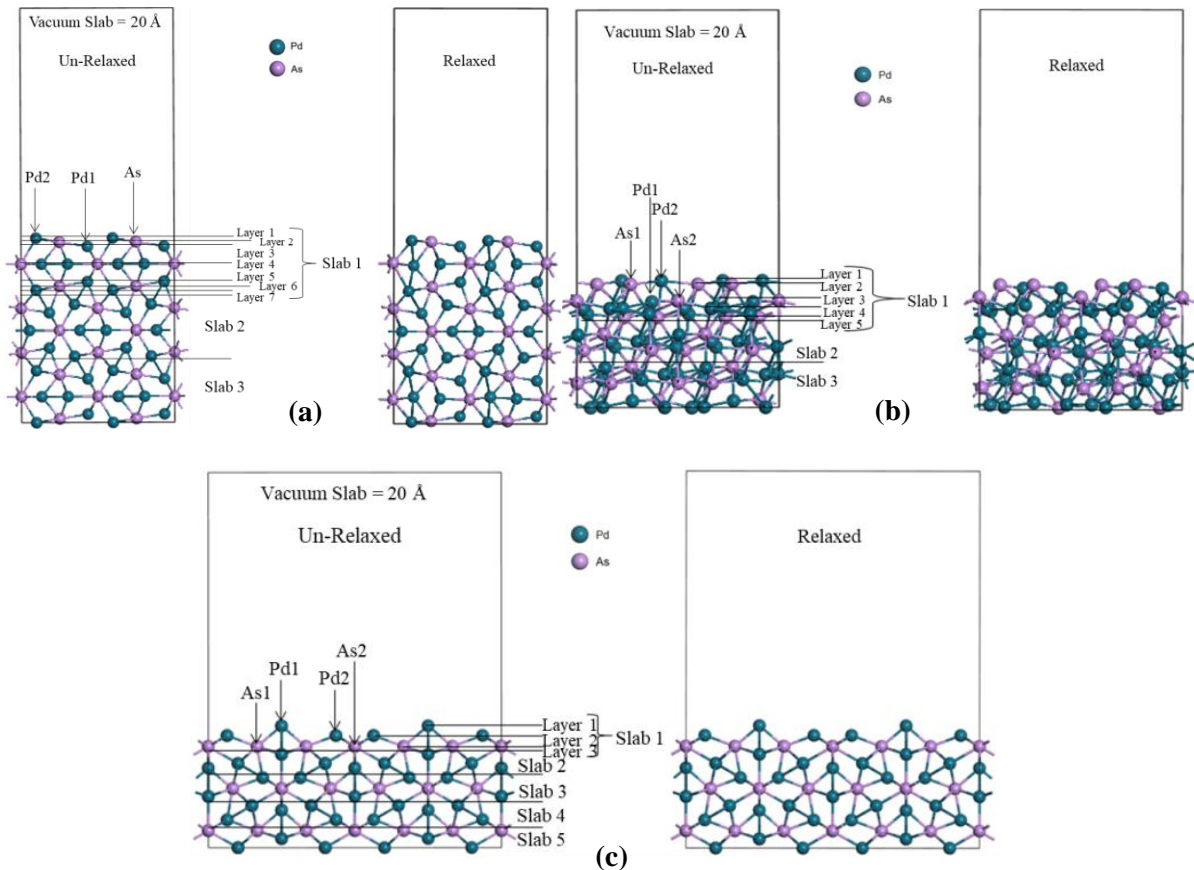


Figure 4.18: The un-relaxed and relaxed supercell structures of surface layers convergence for Pd₂As, (a) (100), (b) (111) and (c) (110) surface.

The slabs for (100) surface are not identical due to stacking configuration [108]. For (110) surface, the relaxation was performed with the bottom 3 slabs fixed to the bulk coordination,

while for (111) the bottom slab (5L) was frozen. Table 4.13 shows the supercell surface results after relaxation. The order of surface stability followed as: (100) > (110) > (111) for Pd₂As model. The (100) surface had the lowest surface energy amongst all the surfaces, thus more stable and it was considered a working surface. Moreover, the un-relaxed and relaxed supercell structures for the model Pd₂As (100), (110) and (111) surfaces are shown on the Figure 4.18(a), 4.18(b) and 4.18(c), respectively.

Table 4.13: Supercell optimization of (100), (111) and (110) surface layers convergence, number of atoms per slab, total energy (eV) and surface energies (J/m²) for Pd₂As system.

Surface slab	Number of atoms on slab	Number of layers	Total energy (slab) (eV)	Surface energy (J/m ²) Relaxed
(100)	108	21	-583.0595	1.128
(111)	144	15	-745.6482	1.743
(110)	108	15	-563.6283	1.594

4.7.3 Analysis of the working surfaces

Also for the Pd₂As a thorough appreciation of the mineral surface was required in order to understand the collector binding environment. The palladoarsenide working surface consisted of ridges of As atoms, with Pd atoms inhabiting the clefts between ridges, as shown in Figure 4.19. When considering the binding of bridging ligands, which can interact with two surface metals simultaneously regarded is the distance between the metal sites. For Pd₂As working surface, the surface inter-palladium distance was 3.655 Å and the distance for the Pd between the cleft was 3.133 Å as shown in Figure 4.19. As such the As lone pairs, causes unlikely bridging of the ligands on the two Pd atoms in different clefts simultaneously, due to the implicit high steric strain.

Table 4.14 shows the bulk and surface coordination and surface energy of (100) surface of Pd₂As. The coordination for various atoms changed after cleaving the surface. The Pd atom for the bulk Pd₂As was 4 and 5-coordinated and after surface cleavage it reduced to 3-coordination for (100) surface. For the As atom, the bulk structure was 9-coordinated, while the (100) surface reduced to 6-coordination. The Pd-Pd atoms for the bulk structure and (100) surface were 2-coordinated.

Table 4.14: Bulk and surface coordination, supercell optimization of (100) surface showing number of atoms per slab and surface energies (J/m^2) for Pd_2As system.

Model	#atoms	Coordination			Surface energy (J/m^2)	
		Pd	As	Pd-Pd		
Pd_2As	Bulk	9	4,5	9	2	–
	(100)	108	3	6	2	1.128

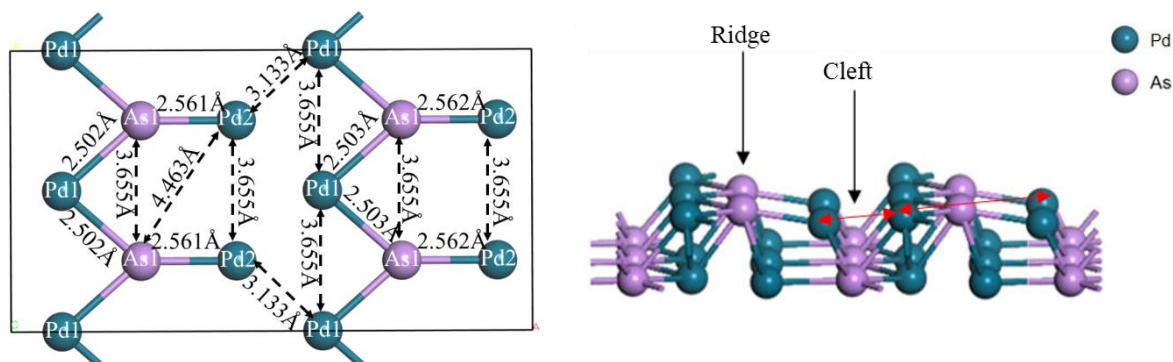


Figure 4.19: Top-view (left) and side view (Right) of the top three layers (3L) on 2×2 supercell working surface of (100) palladoarsenide surface. Showing raised As ridges and Pd atoms inhabiting the clefts between ridges (Right), with the resulting bond distances (Left).

4.8 Surface morphologies of PtAs_2 , PtAsS and Pd_2As surface structures

The morphology of PtAs_2 , PtAsS and Pd_2As structures from crystal structure can be predicted by using calculated surface energies within METADISE code [122]. The calculated thermodynamically equilibrium morphologies of the relaxed (100), (110) and (111) PtAs_2 , PtAsS and Pd_2As surfaces are presented in Figure 4.20. Our results indicated that (100) surface was the most dominant surface as expressed by the calculated surface morphologies, followed by (111) and (110) surface for PtAs_2 and PtAsS (VCA) models. For Pd_2As , the (100) surface was the dominant surface as expressed by surface morphologies, followed by (110) and lastly, the (111) surface. We observed that for PtAsS (CE), only the (100) surface appeared on the morphology, suggesting that the PtAsS mineral may not cleave along the (110) and (111) surfaces. However, for PtAsS (VCA), the (100) and (111) surfaces appeared on the morphology, suggesting that the PtAsS (VCA) model may not cleave along the (110) surface. However, in this case the (110) and (111) were also exposed largely, suggesting that these planes may cleave during mineral crushing.

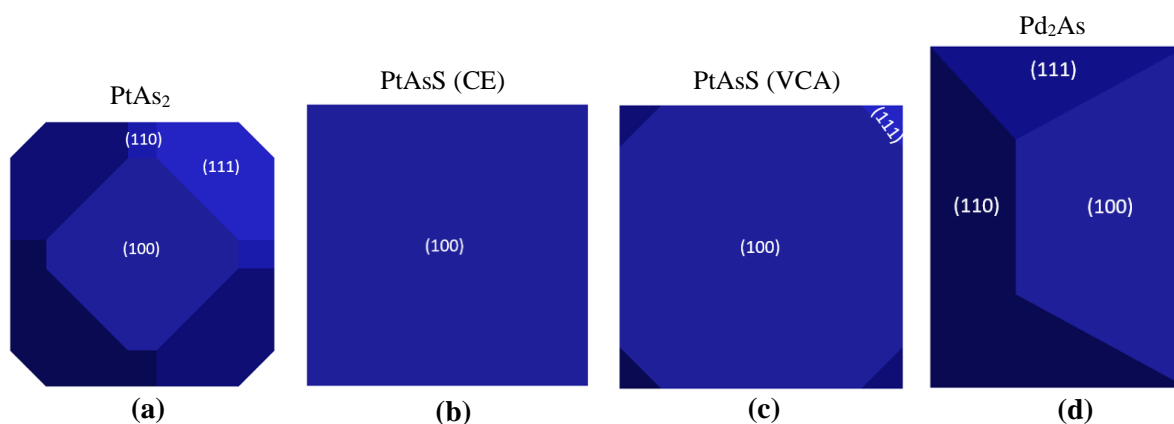


Figure 4.20: The calculated equilibrium surface morphologies: (a) PtAs₂, (b) PtAsS (CE), (c) PtAsS (VCA) and (d) Pd₂As surface structures.

4.9 Electronic structures of the bulk and clean (100) surface for PtAs₂, PtAsS and Pd₂As systems

In this section we discussed the density of states (DOS) of the bulk structures and the most stable (100) surface of PtAs₂, PtAsS and Pd₂As. The atomic charges from Bader analysis for all the structures are discussed. These are important for depicting the nature of bonding behaviour of the bulk and surface. The plots showed both the total density of states (TDOS) and partial density of states (PDOS) of platinum, palladium, arsenic and sulphur atoms in their respective structures.

4.9.1 Total density of states for PtAs₂, PtAsS and Pd₂As structures

In order to correlate the structural and mechanical stability of PtAs₂, PtAsS and Pd₂As systems, we compare their total density of states plots in the Figure 4.21 below. From the literature, it is reported that the density of states of structures of the same composition can show the stability trend with respect to their behaviour at the Fermi level [95]. The structure with the lowest and highest DOS at the Fermi energy is considered the most and least stable, respectively [94, 95]. A sharp peak was noted for the PtAsS (VCA) near the Fermi energy.

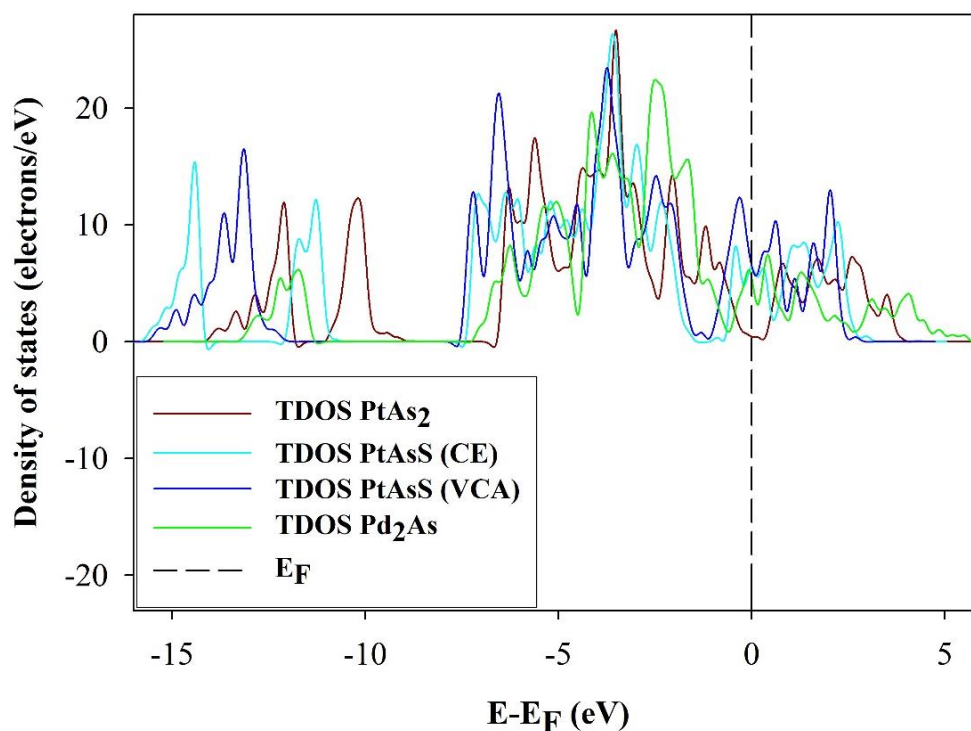


Figure 4.21: Comparison of the total density of states for PtAs₂, PtAsS and Pd₂As structures.

Most importantly, it was clear that PtAs₂ structure had the lower states at the E_F. This indicated that PtAs₂ was the most stable structure. However, the PtAsS (CE) displayed the highest number of states at the E_F which confirms that it was the least stable structure. The PtAsS (VCA) and Pd₂As structures were intermediately stable. Interestingly, our density of states analyses were consistent with the stability trend as predicted by the heats of formation. The predicted phase stability trend using DOS is as follows: PtAs₂ > Pd₂As > PtAsS (VCA) > PtAsS (CE).

4.9.2 Density of states and Bader analysis

Figure 4.22(a) displayed the DOS for PtAs₂ and we found that the Pt 5d-orbital had little (almost zero states) contribution at the Fermi energy (E_F) and low states at the conduction band (CB), with a highest states sharp peak at the valence band (VB). The As 4p-orbitals were observed to have little contribution at the E_F. Moreover, the arsenic 4s-orbitals dominated more at and below -10.0 eV, while the p-orbital contributes significantly at around -6.0 eV and above. Note that we observed two character of the As atoms designated as As1 and As2 atoms. The total density of states (TDOS) showed a pseudo gap forming a band gap of 0.104 eV at the E_F. In addition, the system was suggested to be a semiconductor. Thus, PtAs₂ was more stable because the elements Pt and As have the lowest density of states at the E_F.

Figure 4.22(b) shows the TDOS and the PDOS of the top Pt and As on PtAs₂ (100) surface. We observed that the TDOS display a metallic behaviour with no band gap, which changed from the semiconductor band gap on the bulk structure. Interestingly, we observed that the E_F fell deep into the pseudo gap suggesting stability. We found that the Pt (Pt1 and Pt2) 5d-orbital have a significant contribution at the E_F and at the conduction band with a highest state sharp peak at the valence band. The As (As1 and As2) 4p-orbital were observed to have a contribution at the E_F. The arsenic s-orbital dominated at around -10.0 eV, while the p-orbital contributed significantly at around -2.0 eV. These observations suggested that both Pt and As are equally active on the surface and may both interact strongly with adsorbate.

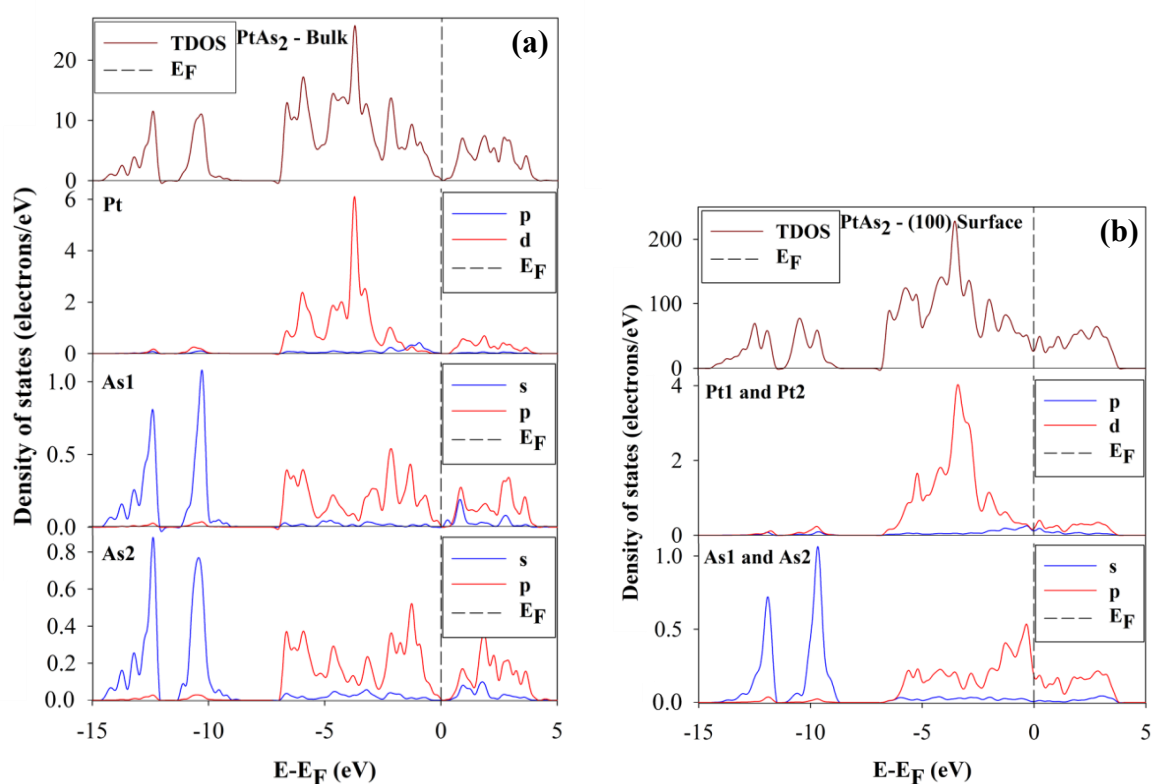


Figure 4.22: TDOS and PDOS of the bulk structure and top most platinum and arsenic atoms: (a) Bulk PtAs₂ and (b) PtAs₂ (100) surface.

In a case of the PtAsS (CE) structure (Figure 4.23(a)), the Pt 5d-orbital showed a greater contribution at the Fermi energy and at the conduction band, with a highest states sharp peak at the valence band. The As 4p-orbitals had greater contribution at the E_F, but lower than those of S 3p-orbital. Moreover, the arsenic s-orbital dominated more below -10.0 eV, while the p-orbital contributes significantly at around 3.0 eV, with a sharp peak at the conduction band. The sulphur 3s-orbital dominated more at around -15.0 eV, while the 3p-orbital contributes significantly at around -2.0 eV as shown in Figure 4.5(b). The system showed a metallic

behaviour because of the absence of band gap, which showed the nature of platarsite. Thus, PtAsS (CE) was less stable since it had the highest density of states at the E_F .

The TDOS and PDOS of the top Pt, As and S atoms on PtAsS (CE) are shown in Figure 4.23(b). The TDOS displayed similar behaviour as that of PtAsS (VCA) in particular at the E_F , where the E_F almost fell deep into the pseudo gap. We found that the Pt (Pt1 and Pt2) 5d-orbital have a significant contribution at the E_F and the valence band and the character of the sharp broad peak is similar to that of PtAsS (VCA). The As and S p-orbital had little contribution at the E_F and we noted that behaviour of the S 3p-orbital is similar to that observed on PtAsS (VCA), which indicated that the S 3p-orbital dominated more than As 4p-orbital between -1.0 and -6.0 eV. We observed that the As 4s-orbital dominated more at -11.0 eV, while the S 3s-orbital contributed significantly at around -14.0 eV, with a sharp peak at the valence band. This also explains the contribution of the s-orbital peaks below -10.0 eV on PtAsS (VCA). This indicated that both VCA and CE gave similar character of platarsite.

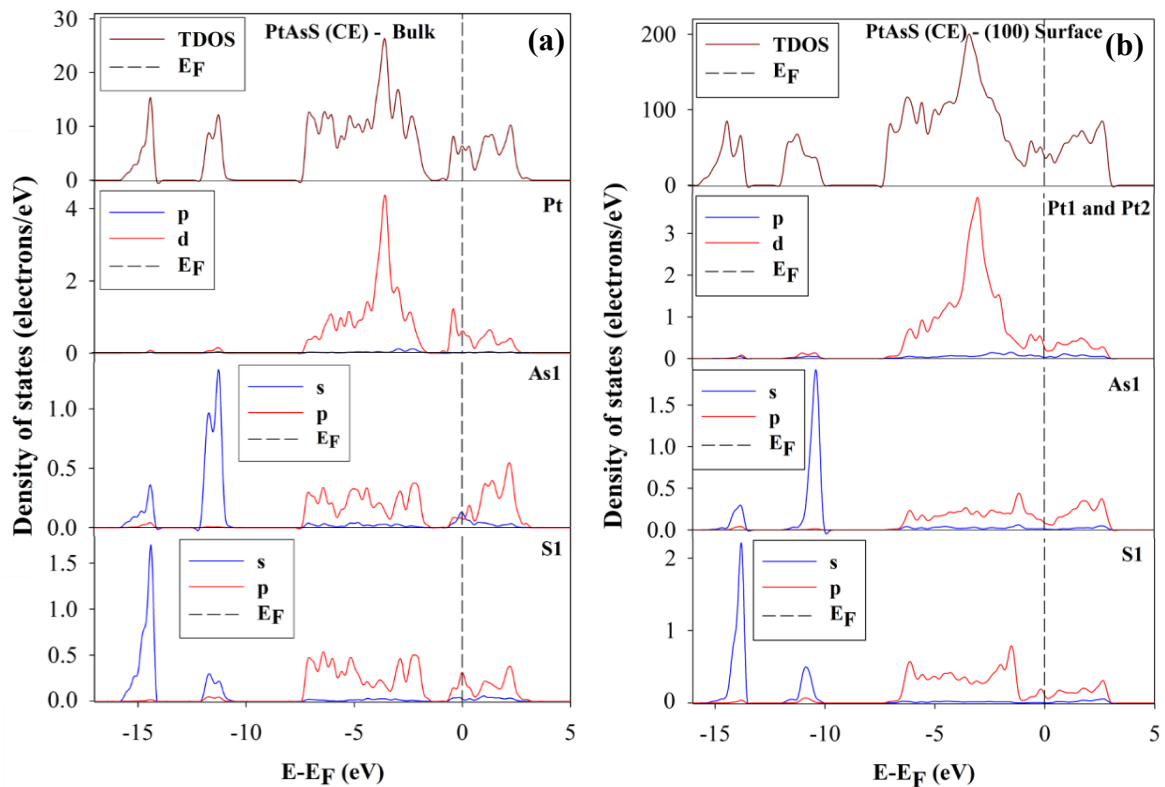


Figure 4.23: TDOS and PDOS of the bulk structure and top most platinum, arsenic and sulphur atoms on (a) PtAsS (CE) and (b) PtAsS (CE) (100) surface.

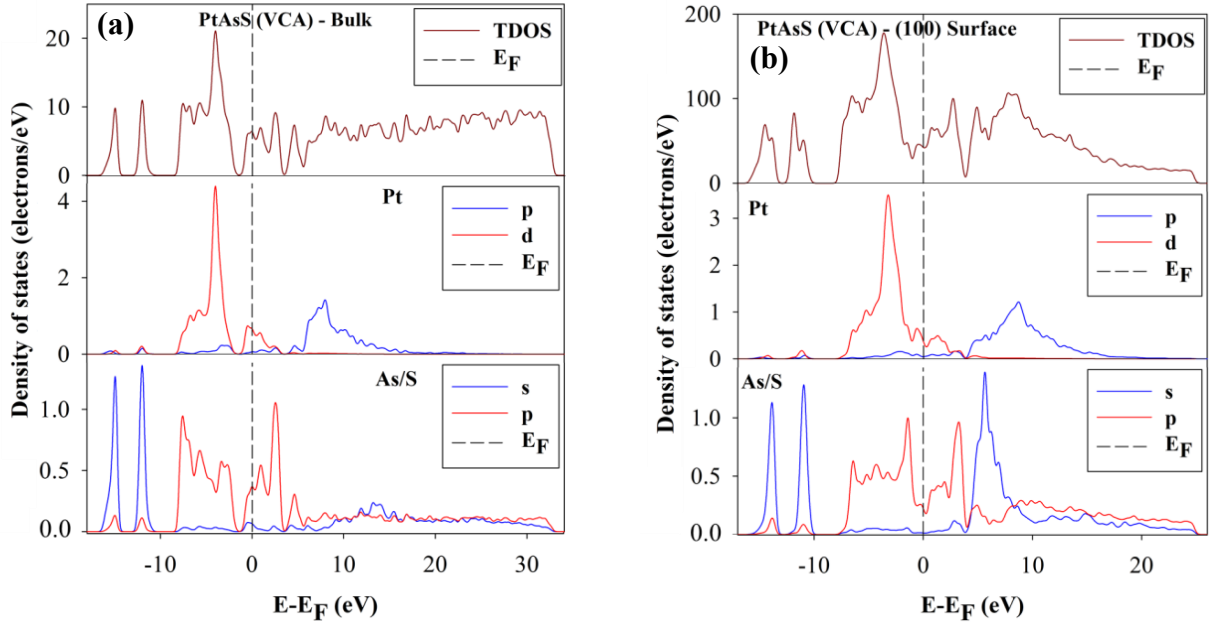


Figure 4.24: TDOS and PDOS of the bulk structure and top most platinum, arsenic and sulphur atoms on (a) PtAsS (VCA) and (b) PtAsS (VCA) (100) surface.

The TDOS for the PtAsS (VCA) was metallic, since there was no band gap observed at the E_F (Figure 4.24(a)). The Pt 5d-orbital showed a greater contribution at the Fermi energy and at the conduction band, with a highest state sharp peak at the valence band. The As 4p-orbitals and S 3p-orbitals (As/S 4p-3p hybrid) were observed to have greater contribution at the E_F , moreover, the arsenic and sulphur s-orbitals dominated more below -10.0 eV, while the p-orbital contributed significantly below 10.0 eV.

The PtAsS (VCA) DOS in Figure 4.24(b), we noted that the E_F shifts into the pseudo gap for the (100) surface suggesting stability, which was not the case for the bulk. The TDOS showed a metallic behaviour since there was no band gap observed at the E_F . We found that the Pt 5d-orbital had a greater contribution at the E_F and at the conduction band with a highest state sharp peak at the valence band. The As/S p-orbital were observed to have a contribution at the E_F . It has been observed that for As/S PDOS, the s-orbital increased in states at the conduction band. This indicated that there was electron loss from the s-orbital to the p-orbital. The As/S s-orbitals dominated more below -10.0 eV and above 0.0 eV, while the p-orbital contributed significantly below 5.0 eV.

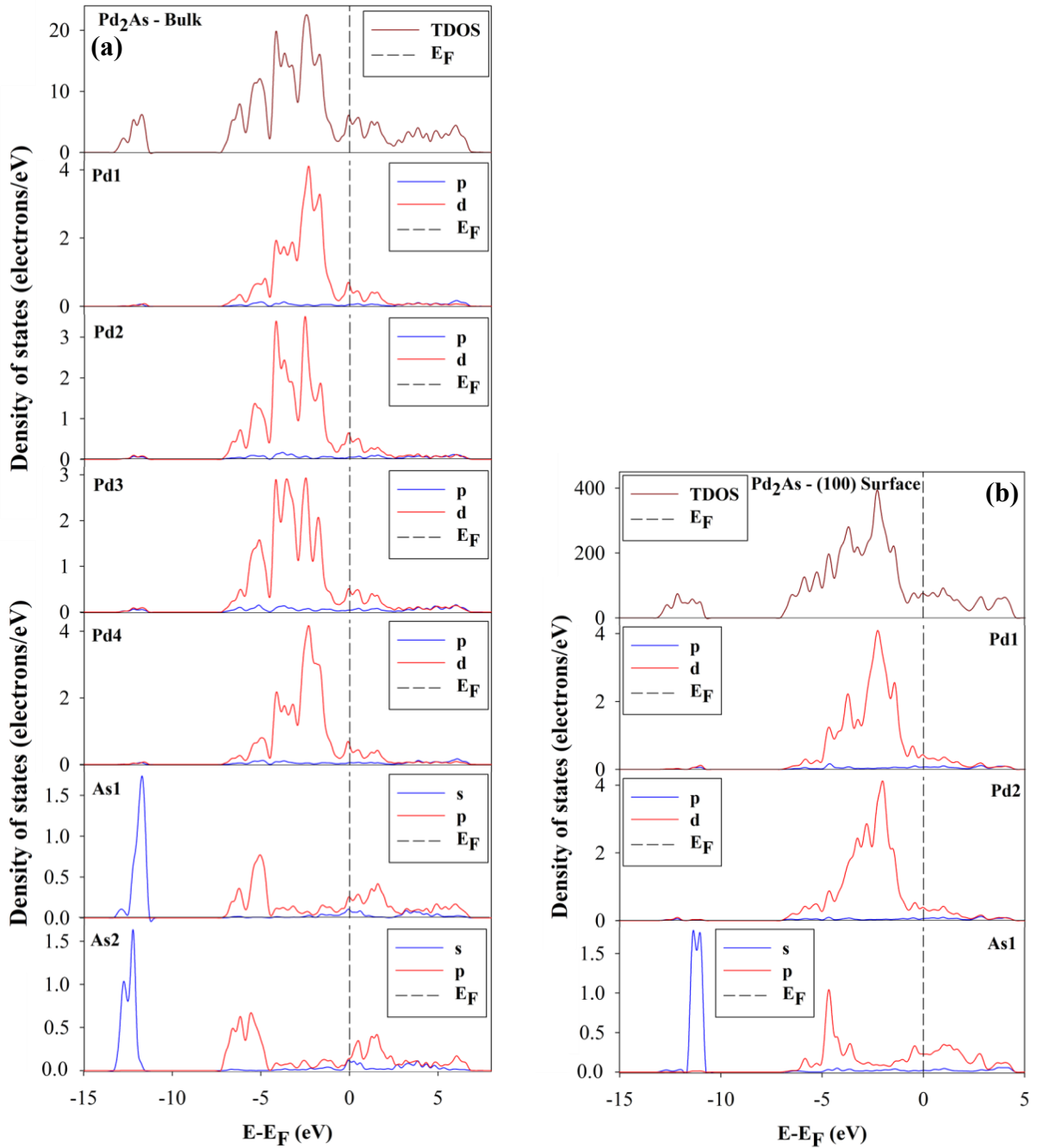


Figure 4.25: TDOS and PDOS of the bulk structure and top most palladium and arsenic atoms on (a) Pd₂As and (b) Pd₂As (100) surface.

The total density of states (TDOS) for Pd₂As showed a metallic behaviour since there was no band gap observed at the E_F (Figure 4.25(a)). The Pd₂As bulk structure has four sites occupied by Pd and two sites occupied by As atoms, these were found to display different DOS character. We found that the Pd 4d-orbital have much contribution at the E_F than the As. We observed that between -2.0 eV and -5.0 eV the Pd had the greater contribution while the As had almost zero states. Furthermore, we observed that Pd1 and Pd4 have similar PDOS

behaviour. The As 4p-orbitals were observed to have little contribution at the E_F . Moreover, the arsenic (As1) and (As2) 4s-orbitals dominates more at around -13.0 eV, while the 4p-orbital contributed significantly at around -6.0 eV (Figure 4.6(b)). Moreover, the states were low at the E_F with the E_F cutting the peak at its highest point.

Figure 4.25(b) display the DOS for Pd_2As (100) surface and we found that the TDOS showed a metallic behaviour since there was no band gap observed at the E_F . The PDOS showed two Pd atoms and one As atom character. We observed that the palladium (Pd1 and Pd2) 4d-orbital atoms have greater contribution between -1.0 and -5.0 eV with a sharp broad peak and very little contribution at the E_F . The As 4p-orbital had low states at the E_F , with As 4s-orbital being very low. The arsenic 4s-orbital dominated at around -12.0 eV, while the 4p-orbital contributed significantly at around -5.0 eV, with a sharp peak at the valence band.

Table 4.15: The calculated Bader analyses for the bulk and relaxed (100) surface of $PtAs_2$, $PtAsS$ (CE) and Pd_2As .

Model	Atom	Bader Charge ($ e^- $)	
		Bulk	(100) Surfaces
$PtAs_2$	Pt	-0.46	-0.45
	As1	+0.21	+0.12
	As2	+0.25	+0.12
$PtAsS$ -CE	Pt1	-0.12	-0.19
	Pt2		-0.08
	As1	+0.58	+0.45
	S1	-0.46	-0.40
Pd_2As	Pd1	-0.02	-0.13
	Pd2	-0.10	-0.10
	Pd3	-0.09	-
	Pd4	-0.01	-
	As1	+0.10	+0.11
	As2	+0.12	-

Table 4.15 summarizes the Bader charges of (100) surface of $PtAs_2$, $PtAsS$ (CE) and Pd_2As in comparison with the Bader charges of the bulk structures. Note that the $PtAsS$ (VCA) model could not produce population charges due to the complexity of the virtual As/S atoms mixed and occupying the same lattice position. The focus was more on the charges of the top two layers atoms. The charges for Pt, Pd and S atoms adopted negative charges, while the As atoms adopted positive charges for $PtAs_2$, $PtAsS$ (CE) and Pd_2As models. We noted that the bulk $PtAs_2$ structure possess a charge of $-0.46|e^-|$ on Pt atom and positive charges of $+0.21|e^-|$ and $+0.25|e^-|$ on As atoms and for $PtAs_2$ (100) surface, the Pt and As atoms adopted $-0.45|e^-|$ and $+0.12|e^-|$ charges, respectively. In comparison of $PtAs_2$ bulk structure with (100) surface, we noted that Pt atom lost $0.01|e^-|$ charge, while As atom gained charges and both As1 and As2 and adopted same charges on the surface. The Bader charges for $PtAsS$ (CE) were $-0.12|e^-|$, $+0.58|e^-|$

| and $-0.46|e^-|$ for Pt, As and S atoms, respectively. For PtAsS (CE) (100) surface, we noted charges of $-0.19|e^-|$, $-0.08|e^-|$, $+0.45|e^-|$ and $-0.40|e^-|$ for Pt1, Pt2, As1 and S1 atoms, respectively. This indicated that the Pt atom resulted in two different character, where Pt1 gained $0.07|e^-|$, while Pt2 lost $0.04|e^-|$, with the As atom gaining $0.13|e^-|$ and S atom losing $0.06|e^-|$ charges. Furthermore, Pd₂As bulk structure adopted charges of $-0.02|e^-|$, $-0.10|e^-|$, $-0.09|e^-|$ and $-0.01|e^-|$ for Pd1, Pd2, Pd3 and Pd4 atoms, while As1 and As2 atoms adopted charges of $+0.10|e^-|$ and $+0.12|e^-|$, respectively. Since the Pd1 and Pd4 had similar PDOS character, we noted that their Bader charges were almost equal. The Pd₂As (100) surface was found to possess $-0.13|e^-|$, $-0.10|e^-|$ and $+0.11|e^-|$ charges for Pd1, Pd2 and As1 atoms, respectively. This showed that Pd1 gained $0.11|e^-|$, while Pd2 remained unchanged, with the As1 atom losing only $0.01|e^-|$ charge. All the charges showed different behaviour for PtAs₂, PtAsS and Pd₂As structures. Since the surface cleavage resulted in change of the coordination, thus the charges of the surface atoms changed.

These are complimented by the density of states, where we observed a decrease in Pt d-orbital states at the valence band for PtAs₂ (100) surface, which suggested electron loss. The PtAs₂ As p-orbital states on the bulk were low at the E_F and we noted an increase in states at the E_F for PtAs₂ (100) surface, this indicated electron gain. The case of PtAsS (VCA) showed two character of Pt atoms on the Bader charges, but the Pt d-orbital PDOS were the same, as such the difference on charges was due to the coordination of the Pt atoms on the surface. We noted that Pt1 is coordinated to two S atoms in layer 1, two As atoms in layer 3 and one As atom in the first layer of slab 2, while Pt2 is coordinated to two As atom in layer 1, two S atoms in layer 3 and one S atom in the first layer of slab 2. As such this indicated that Pt1 is coordinated to three As atoms, while Pt2 is coordinated to three S atoms on the PtAsS (VCA) (100) surface. Since we noted that S atoms gain charges, while As atoms loses charges, this suggested that Pt1 gain charges from As atoms, while Pt2 lost charges to S atoms. This is the reason the PDOS could not clear show the difference on Pt and as well on the As and S atoms PDOS. However, we noted that the s-orbital on As atom was reduced at the E_F to zero states on the PtAsS (VCA) (100) surface, while it dominated the E_F on the PtAsS (VCA) bulk. This suggested greater electron loss from s-orbital to the As atom. Comparison of the Pd₂As bulk and (100) surface, it was observed that Pd1, Pd2 and As1 reduced states at the E_F . However, since Pd2 did not change in Bader charges, we noted that the splitting peaks were merged into a broad splitting peak. Interestingly, we noted that the s-orbital on As1 atom was reduced to zero states on the surface compared to the bulk, suggesting that the $0.01|e^-|$ charge was depleted from the s-orbital.

4.10 Summary

In this chapter we have cleaved the PtAs₂, PtAsS and Pd₂As surface and performed surface structural relaxations. The results obtained were achieved by the use of sufficient number of plane-waves. The cut-off energy suitable to converge the total energy of the surface systems were found to be 450 for PtAs₂, PtAsS and 500 eV for Pd₂As. We also employed k-points for all the geometry optimization of the surfaces, the 4x4x1 for PtAs₂, PtAsS and 5x3x1 k-point mesh for Pd₂As surfaces were used. The three low-Miller index (100), (110) and (111) surfaces were considered and cleaved from the relaxed bulk structures. Different surface termination and surface layers were investigated and considered the termination and slab thickness that is favorable with the lowest surface energy. The Term.2 for (100) and (110) surface and Term.3 for (111) were the most stable surface terminations for PtAs₂. For PtAsS (CE) model, the Term.2 for all the (100), (111) and (110) surfaces were found the most stable. The PtAsS (VCA) showed that Term.2 for (100) and Term.3 for (111) and Term.1 for (110) surface were found the most stable. Lastly, the Term.1 for (100) and (111) and Term.4 for (110) surface indicated that they were the most stable terminations for Pd₂As model. The fifteen layer (15L) slab and twenty one layer (21L) slab were chosen for the three low Miller index planes for all surface structures and used to create 2x2 supercell structures. From the data, it was readily apparent that the (100) surface was the most stable (working) surface for all the minerals. The order of surface stability followed as: (100) > (111) > (110) for PtAsS and PtAs₂ structures. In addition, Pd₂As structure showed the surface stability order as: (100) > (110) > (111).

The density of states for PtAs₂ showed that the system was a semiconductor with a band gap of 0.104 eV. The total density of states showed a metallic behaviour for PtAsS (CE), PtAsS (VCA) and Pd₂As since there was no band gap observed and there were states at the E_F. Most importantly, it was clear that PtAs₂ had lower number of states at the E_F as compared to the PtAsS and Pd₂As structures. This indicated that PtAs₂ was the most stable structure. The Pt, Pd and S atoms showed negative Bader charges, while As atom showed a positive charge for PtAs₂, PtAsS (CE) and Pd₂As.

The density of states for (100) surface of PtAs₂, PtAsS (CE), PtAsS (VCA) and Pd₂As showed a metallic behaviour since no band gap was observed at the E_F. The surface structure, PtAsS (CE) was found the most stable because of the lowest density of states contribution at the E_F and although it had similar character to that of VCA. The Bader charges indicated that the cleavage of the surfaces results in change in atomic charges, either gain or lose which is as a result of change of the coordination.

CHAPTER 5

Summary and conclusions

The dissertation gave an overall perspective of the structural, thermodynamic, elastic, mechanical, vibrational, electronic and surface properties of PtAs₂, PtAsS and Pd₂As minerals structures using density functional theory VASP and CASTEP codes. The results were achieved by the use of sufficient number of plane-waves. We have determined the cut-off energy suitable to converge the total energy of the systems to be 500 eV for the bulk PtAs₂, PtAsS and 450 eV for the bulk Pd₂As. The number of k-points of 6x6x6 for PtAs₂ and PtAsS and 7x7x14 for Pd₂As were found sufficient to converge the bulk structures. The geometry optimizations for all the structures were performed to compare their structural properties. The lattice parameters for these systems were allowed to vary, thereby minimizing the structures to their stable form. We found that the lattice parameters were in good agreement with the experimental lattice parameters which was acceptable for density functional theory. The binary ground state diagram for the cluster expansion showed that all structures have negative heats of formation, hence they were thermodynamically stable (miscible constituents). Moreover, the cluster expansion showed a greater stability at 50/50 (x = 0.5) percentage, where As and S atoms were equally distributed in the structure with a S–As dimer bond formed at the centre. The heats of formation divulged that all the structures had negative heats of formation. In addition, the heats of formation values suggested that the PtAs₂ structure was the most stable (i.e. energetically favourable). The PtAsS (CE) was found the least stable, while the PtAsS (VCA) and Pd₂As structures were intermediately metastable.

The elastic constants for the cubic structures, PtAs₂ and PtAsS (VCA ad CE) and a monoclinic structure Pd₂As and the bulk modulus (*B*), tetragonal shear modulus (*C'*), isotropic shear modulus (*G*) and Young's modulus (*E*) were calculated. In addition, the anisotropic factor (*A*), Poisson's ratio (*ν*), the bulk to shear (*B/G*) and the Cauchy pressures *C*₁₂ – *C*₄₄ were also calculated. The cubic systems PtAs₂ and PtAsS (CE) were mechanically stable since their values of *C*₁₁, *C*₁₂ and *C*₄₄ were all positive and greater than zero. The cubic stability conditions were also satisfied. However, the PtAsS (VCA) structure did not satisfy the necessary conditions of a cubic structure, since *C*₁₁ was much lesser than *C*₁₂ and *C*₄₄ and *C'* being negative, which suggested instability. Furthermore, the Pd₂As structure was mechanically stable since all the mechanical stability criteria for a monoclinic structure were satisfied. A ratio

of bulk to shear was introduced, where a high B/G value of greater than 1.75 is associated with ductility, while a lower value represented brittleness. Our results showed that the structures PtAsS (CE) and Pd₂As were all ductile due to high values of B/G , whereas the PtAsS (VCA) and PtAs₂ were brittle since they had a lower B/G values than 1.75. The calculated Young's modulus indicated that PtAs₂ was much stiffer, since it had the largest value of elastic constant. This suggested that PtAs₂ structure was mechanically stronger compared to the PtAsS structures. The types of bonding in a solid were predicted from the sign of a Cauchy pressure ($C_{12} - C_{44}$). The PtAs₂ was dominantly covalent bonded compound since the Cauchy pressure ($C_{12} - C_{44} < 0$) was negative, while the PtAsS structures and Pd₂As were ionic bonded because the Cauchy pressure ($C_{12} - C_{44} > 0$) were positive. Moreover, this was also determined from the bond sorting using Poisson's ratio, where a covalently bonded compounds has a Poisson's ratio value lower than 0.25, while the typical ionic compounds is nearly 0.25 or higher. The Poisson's ratio values for PtAsS (VCA), Pd₂As and PtAsS (CE) structures exhibited ionic bonding. However, it was noticeable that the Poisson's ratio of PtAs₂ phase was 0.23 which indicated a dominant covalent bonding.

The phonon dispersion curves and the phonon partial density of states (PPDOS) for PtAs₂, PtAsS (CE) and Pd₂As had no negative frequencies (soft modes) along the gamma direction, which suggested vibrational stability. The density of states for PtAs₂ bulk structure showed that the system was a semiconductor with a band gap of 0.104 eV. The total density of states showed a metallic behaviour for PtAsS (CE), PtAsS (VCA) and Pd₂As structures since there was no band gap observed at the E_F . Most importantly, it was clear that PtAs₂ had lower number of states at the E_F as compared to PtAsS structures. This indicated that PtAs₂ was the most stable structure. The Pt and Pd species showed negative Bader charges, while As species showed a positive charge on both PtAs₂ and Pd₂As structures. The PtAsS (CE) showed a negative charge for Pt and S species and a positive charge for As species, while the PtAsS (VCA) structure showed a negative and positive Mulliken populations atomic charges for Pt and As/S species. The As atom gained charges from the top layers of Pt and again from the sub layers of Pt atoms, while the Pt top layer atoms lost charges. The charge loss and gain for all atoms on the surface were very small, thus there would be no change in oxidation states.

For surface study, we have employed the same cut-off energy as for the bulk structures and determined the suitable k-points of the surfaces as 4x4x1 for PtAs₂, PtAsS and 5x3x1 k-point mesh for Pd₂As surfaces. The three low-miller index (100), (111) and (110) were considered and cleaved from the relaxed bulk structures. Different surface layers were investigated and considered the slab thickness that was favorable with the lowest surface energy. The Term.2

for (100) and (110) and Term.3 for (111) were the most stable surface terminations for PtAs₂ and PtAsS (CE). The case of PtAsS (VCA) mineral showed that the Term.2 for (100) and the Term.3 for (111) and Term.1 for (110) surface were the most stable terminations. However, the Term.2 for (110) surface was considered due to the non-dipole within the structure. The Pd₂As showed that Term.1 for (100) and (111) and Term.4 for (110) surface were the most stable terminations. The fifteen layer slab and twenty one layer slab were chosen for the three low Miller index planes for all the structures and were used to create 2x2 supercell structures and their surface energies order in stability decreases as: (100) > (111) > (110) for PtAs₂ and PtAsS (VCA and CE), while for Pd₂As decreases as (100) > (110) > (111). From the data, it is readily apparent that the (100) surface was the most stable surface for all the minerals PtAs₂, PtAsS (VCA and CE) and Pd₂As structures. The calculated thermodynamically equilibrium morphologies of the relaxed surface structures indicated that the (100) surface was the most dominant surface for all the surface structures.

The density of states for (100) surface of PtAs₂ and Pd₂As structures showed a metallic behaviour since no band gap was observed at the E_F, while PtAsS structures showed a semiconductor behaviour with an indirect band gaps of 0.142 eV for PtAsS (CE) and 0.551 eV for PtAsS (VCA). This showed a transformation change from bulk (metallic) to surface (semiconductor) for PtAsS (CE and VCA), which could be explored for its flotation behaviour compared to the other minerals. We have found that the PtAsS (VCA) was the most stable because of the lowest DOS contribution at the E_F. These findings gave more insights on the stability of these minerals and their surface stabilities which demonstrated the preferred plane cleavage of these minerals and may be applicable in their recovery.

Recommendation and future work

In this dissertation an investigation of structural, thermodynamic, elastic, mechanical, vibrational, electronic and surface stabilities of sperrylite (PtAs₂), platarsite (PtAsS) and palladoarsenide (Pd₂As) has been undertaken using density functional theory on which further research would be beneficial.

The areas where information is lacking were highlighted in the literature review. Whilst some of these were addressed by the research in this dissertation, others remain. In particular, the design of novel collector reagents that plays a role in rendering these minerals hydrophobic and thus improving the floatability of these slow floating arsenide minerals. Furthermore, the reactivity chemistry of the collectors with the surfaces of these systems, that would describe

their recovery during flotation. The future studies could investigate and compare the nitrogen and oxygen based collectors into finding the best binding ligands that will ultimately promote recovery separation of these minerals from the gangue minerals. In addition the experimental micro-flotation and calorimetry approach would be beneficial in attaining the actual outcomes of those collectors that would have predicted strong binding onto the surface. Although the oxidation and hydration have been investigated previously, particularly for PtAs₂, it would be beneficial to explore these for the other structures (i.e. PtAsS and Pd₂As). In addition the investigation of water-collector adsorption on the surfaces would be paramount in attempting to emulate the actual flotation process.

There are areas for further research that have been highlighted by the studies undertaken for this dissertation. These include the further exploring of the surface reconstruction of dipole unstable surfaces and introduction of impurities onto the surface. These impose questions of how realistic are those surfaces stabilities and would these reconstructed surfaces exhibit the thermodynamically stable surface models that would determine the experimental cleavage of these minerals during crushing/grinding?. How would the impurities substitution in the bulk structures affect or improve the structures in their stabilities?. These would help to confirm and possibly identify the behaviour of the bulk and surfaces that are contaminated and thus establish what could be possible cause to flotation decrease of the arsenide minerals. Furthermore, describe how the reconstructed surface interacts with collectors.

This study has investigated the stability of PtAs₂, PtAsS and Pd₂As from heats of formations, mechanical, density of states, phonon dispersion curves and surface stability that are directly important in describing and predicting the stability of structures. This has demonstrated the importance of such approach where their stabilities have been established and proposed stable and less reactive (100) surfaces have been identified for all structures. Similar approaches have been employed previously and it has been pointed out that these may be implemented in other studies in order to predict, particularly the preferred surface cleavage of minerals that require fundamental insights that will be translated to their reactivity and giving direction into experimental tests for surface-ligands.

The computational approach employed in this research to establish and demonstrate the bulk and structural stability of PtAs₂, PtAsS and Pd₂As that predicts their formation and cleavages that are paramount for the recovery of the minerals. This may be usefully applied to other systems and has laid a foundation in describing preferred surface cleavages and determining the lowest ground states of PtAsS system from CE and VCA. Some indication of how reliable the prediction of these stabilities properties are based on the outcomes of each property, for

example the heats of formation gave the same prediction as those from density of states and vibrational stabilities indicated similar behaviour from mechanical stabilities.

References

- [1] Waterson C.N., Tasker P.A., Farinato R., Nagaraj D.R., Shacklenton N. and Morrison C.A. (2016). A computational and experimental study on the binding of dithioligands to sperrylite, pentlandite and platinum. *Journal of Physical Chemistry*, 120, 22476-22488.
- [2] Schouwstra R.P., Kinloch E.D. and Lee C.A. (2000). Platinum excavation on the UG-2 reef in South Africa. *Platinum Metals Review*, 44, 33-39.
- [3] Shaik K. and Petersen J. (2017). An investigation of the leaching Pt and Pd from cooperite, sperrylite and column bioleached concentrates in thiocyanate-cyanide systems. *Hydrometallurgy*, 173, 210-217.
- [4] Jones R.T. (2005). An overview of Southern African PGM smelting. *Annual Conference of Metallurgists*, 40, 147-178.
- [5] Cawthorn S.G. (1999). The platinum and palladium resources of the Bushveld Complex. *South African Journal of Science*, 95, 481-489.
- [6] Vaughan D.J. and Craig J.R. (1978). Mineral chemistry of metal sulphides, Cambridge University Press, Cambridge. *Transaction of the Institution of Mining and Metallurgy*, 23, 149-167.
- [7] Osbahr I., Klemd R., Oberthür T., Brätz H. and Schouwstra R.P. (2013). Platinum-group element distribution in base metal sulphides of the Merensky reef from the Eastern and Western Bushveld complex, South Africa. *Mineralogy Deposita*, 48, 211-232.
- [8] Gronvold F. and Rost E. (1956). On the sulphides, selenides and tellurides of palladium. *Acta Chemica Scandinavica*, 10, 1620-1634.
- [9] Buckley A.N. and Walker W. (1988). The surface composition of arsenopyrite exposed to oxidizing environments. *Applied Surface Science*, 35, 227-240.

- [10] Buckley A.N. and Woods R. (1991). Surface composition of sulphide minerals under flotation related condition. *Surface and Interface Analysis*, 17, 675-680.
- [11] Legrand D.L., Bancroft G.M. and Nesbitt H.W. (2005). Oxidation/alteration of pentlandite and pyrrhotite surfaces at pH 9.3: Part 1. Assignment of XPS spectra and chemical trends. *American Mineralogist*, 90, 1042-1054.
- [12] Godel B., Barnes J.S. and Maier W.D. (2007). Platinum-group elements in sulphide minerals, platinum-group minerals, and whole-rocks of the Merensky reef (Bushveld complex, South Africa): Implications for the formation of the reef. *Journal of Petrology*, 48, 1569-1604.
- [13] Cabri L.J. (1992). The distribution of trace precious metals in minerals and mineral products. *Mineralogical Magazine*, 56, 289-306.
- [14] Finkelstein N.P. and Allison S.A. (1997). The activation of of sulphide minerals for flotation. *International Journal of Mineral Processing*, 52, 81-120.
- [15] Hung A., Yarovsky I. and Russo S.P. (2003). Density functional theory studies of xanthate adsorption on the pyrite FeS₂ (110) and (111) surfaces. *The Journal of Chemical Physics*, 118, 6022-6029.
- [16] Hung A., Muscat J., Yarovsky I. and Russo S.P. (2002). Density functional theory studies of pyrite FeS₂ (111) and (210) surfaces. *Surface Science*, 520, 111-119.
- [17] Chen J., Lan L. and Chen Y. (2013). Computational simulation of adsorption and thermodynamic study of xanthate, dithiophosphate and dithiocarbamate on galena and pyrite surfaces. *Minerals Engineering*, 46, 136-143.
- [18] Wang Q. and Heiskanen K. (1990). Separation of pentlandite and nickel arsenides mineral by aeration flotation condition. *International Journal of Mineral Processing*, 29, 99-109.
- [19] Fuerstenau M.C., Jameson G. and Yoon R. (2007). Froth flotation. *A Century of Innovation*, 7, 128-132.

- [20] Fuerstenau D.W. (1995). International mineral processing congress. *San Francisco*, 7, 132-135.
- [21] Walker G.W., Walters C.P. and Richardson P.E. (1986). Hydrophobic effects of sulfur and xanthate on metal and mineral surfaces. *International Journal of Mineral Processing*, 18, 119-137.
- [22] Zouboulis A.I., Kydros K.A. and Matis K.A. (1992). Adsorbing flotation of copper hydroxo precipitates by pyrite fines. *Separation Science Technology*, 27, 2143-2155.
- [23] Loewenberg M. and Davis R.H. (1994). Flotation rates of fine, spherical particles and droplets. *Chemical Engineering Science*, 29, 3923-3941.
- [24] Hatton D.R. and Hatfield D.P. (2012). Flotation processes. *Minerals Engineering*, 36, 12-21.
- [25] Muzenda E., Afolabi A.S., Abdulkareem A.S. and Ntuli F. (2011). Effect of pH on the recovery and grade of base-metal sulphides by flotation. *Proceedings of the World Congress on Engineering and Computer Science*, 2, 609-612.
- [26] Carvalho T. (2010). Separation of packaging plastics by froth flotation process.
- [27] Nickel H.E. (1995). International mineralogical association, commission on new minerals and mineral names: Definition of a mineral. *Mineralogy and Petrology*, 53, 323-326.
- [28] Nickel E.H. and Grice J.D. (1998). The IMA commission on new minerals and mineral names: Procedures and guidelines on mineral nomenclature. *The Canadian Mineralogist*, 36, 3-4.
- [29] Goghil B.M., and Wilson A.H. (1993). Platinum-group minerals in the Selukwe Subchamber, Great Dyke, Zimbabwe: Implications for PGE collection mechanisms and post-formational redistribution. *Mineralogical Magazine*, 57, 613-633.
- [30] Szymański J.T. (1979). The crystal structure of platarsite, Pt (As, S)₂, and a comparison with sperrylite, PtAs₂. *Canadian Mineralogist*, 17, 117-123.

- [31] Nguyen-Mahn D., Ntoahae P.S., Pettifor D.G. and Ngoepe P.E. (1999). Electronic structure of platinum-group minerals: Prediction of semiconductor band gaps. *Journal of Molecular Simulation*, 22, 23-30.
- [32] Bai L., Barnes S.J. and Barker D.R. (2017). Sperrylite saturation in magmatic sulfide melts: Implications for formation of PGE-bearing arsenides and sulfarsenides. *American Mineralogist*, 102, 966-974.
- [33] Powell H.M., Prout C.K. and Wallwork S.C. (1964). Crystallography. *Annual Reports on the Progress of Chemistry*, 61, 567-615.
- [34] Wells H.H. (1889). Sperrylite, a new mineral. *American Journal of Science*, 37, 67-70.
- [35] Cabri L.J., Laflamme J.H.G. and Stewart J.M. (1977). Platinum group minerals from onverwacht. Platarsite, a new sulfarsenide platinum. *Canadian Mineralogist*, 15, 385-388.
- [36] Begizov V.D., Meshchinkina V.I. and Dubakina L.S. (1974). Palladoarsenide, Pd₂As, a new natural palladium arsenide from copper-nickel ores of the Oktyabr deposits. *International Geology Review*, 16, 1294-1297.
- [37] Cabri L.J., Laflamme J.H.G., Stewart J.M., Rowland J.F. and Chen T.T. (1975). New data on some palladium arsenides and antimonides. *Canadian Mineralogist*, 13, 321-335.
- [38] Segall M.D., Lindan P.J.D., Probert M.J., Pickard C.J., Hasnip P.J., Clark S.J. and Payne M.C. (2002). First principle simulations: Ideas, illustrations and the CASTEP code. *Physical Review B*, 14, 2717-2744.
- [39] Vignale R.G. (1979). DFT in magnetic fields. *Physical Review Letters*, 59, 2360-2363.
- [40] Dft.https://en.wikipedia.org/wiki/Density_functional_theory.
- [41] Hohenberg P. and Kohn W. (1964). Inhomogeneous electron gas. *Physical Review B*, 136, 864-871.
- [42] Kohn W. and Sham L.J. (1965). Self-consistent equations including exchange and correlation effects. *Physical Review A*, 140, 1133-1138.

- [43] Slater J. and Verma H.C. (1929). The Theory of Complex Spectra. *Physical Review*, 34, 1293-1322.
- [44] Payne M.C., Teter M.P., Allan D.C., Arias T.A. and Joannopoulos J.D. (1992). Iterative minimization techniques for ab-initio total-energy calculations: molecular dynamics and conjugate gradients. *Reviews of Modern Physics*, 64, 1045-1097.
- [45] Sherrill C.D. (2004). Introduction to density functional theory. *Physical Chemistry*, 22, 134-145.
- [46] Kudoh Y. and Takeda A.H. (1986). Local density approximation for the exchange-correlation energy of an electronic system. *Physical and Chemistry of Minerals*, 13, 233-237.
- [47] Perdew J.P. and Wang Y. (1991). Generalized gradient approximation for the exchange-correlation hole of a many-electron system. *Physical Review B*, 45, 13244-13249.
- [48] Cuevas J.C. (1964). Introduction to density functional theory. 1-29.
- [49] Perdew J.P. and Wang Y. (1986). Generalized gradient approximations for the exchange-correlation hole of a many-electron system. *Physical Review B*, 33, 8800-8822.
- [50] Perdew J., Burke K. and Ernzerhof M. (1996). Generalized gradient approximation made simple. *Physical Review Letters*, 77, 3865-3868.
- [51] Segall M.D. (1997). Ab initio study of biological system. *Journal of Physics*, 23, 283-289.
- [52] Ashcroft N.W. and Mermin N.D. (1976). Solid state physics. *Physical Review B*, 13, 27-32.
- [53] Perdew J.P. and Wang Y. (1992). Generalized gradient approximation for the exchange-correlation hole of a many-electron system. *Physical Review B*, 45, 244-249.
- [54] Cohen M.L. and Heine V. (1970). Solid state physics. *Physical Review B*, 24, 627-629.

- [55] Vanderbilt D. (1990). Soft self-consistent pseudopotentials in a generalized eigenvalue formalism. *Physical Review B*, 41, 7892-7895.
- [56] Clark S.J., Segall M.D., Pickard C.J., Hasnip P.J., Probert M., Refson K. and Payne M.C. (2005). First principles methods using CASTEP. *Zeitschrift fur Kristallograhie*, 220, 567-570.
- [57] Kresse G. and Furthmüller J. (1996). Efficient iterative schemes for ab-initio total-energy calculations using a plane-wave basis set. *Physical Review B*, 54, 11169-11186.
- [58] Hammann D.H., Schluter M. and Chiang C. (1979). Norm-conserving pseudopotentials. *Physical Review Letters*, 43, 1494-1497.
- [59] Chadi D.J. and Cohen M.L. (1973). Special points in the Brillouin zone. *Physical Review B*, 8, 5747-5753.
- [60] Monkhorst H.F. and Park J.D. (1976). Special points for Brillouin-zone integrations. *Physical Review B*, 13, 5188-5192.
- [61] Ramer N.J. and Rappe A.M. (2000). Application of a new virtual crystal approach for the study of disorders perovskites. *Journal of Physics and Chemistry of Solids*, 61, 315-320.
- [62] Bellaiche L. and Vanderbilt D. (2000). Virtual crystal approximation revisited: Application to dielectric and piezoelectric properties of perovskites. *Physical Review B*, 61, pp. 7877-7782.
- [63] Sanchez J.M., Ducastelle F. and Gratias D. (1984). Generalized cluster description of multicomponent systems. *Physica A: Statistical Mechanics and its Applications*, 128, 334-350.
- [64] Müller S. (2003). Bulk and surface ordering phenomena in binary metal alloys. *Journal of Physics Condensed Matter*, 34, 1429-1500.
- [65] Blöchl P.E. (1994). Projector augmented-wave method. *Physical Review B*, 50, 17953-17979.

- [66] Kresse G. (2011). VASP group, theoretical physics departments, Vienn. *Physical Review B*, 84, 2780-2785.
- [67] Zhou Z. and Joos B. (1996). Stability criteria for homogeneously stressed materials and the calculation of elastic constants. *Physical Review B*, 54, 3841-3850.
- [68] Beckstein O., Klepeis J.E., Hart G.L.W. and Pankratov O. (2001). First-principles elastic constants and electronic structure of α -Pt₂Si and PtSi. *Physical Review B*, 63, 134112-134123.
- [69] Born M. and Huang K. (1956). Dynamical theory of crystal lattices. *Acta Crystallographica*, 9, 837-838.
- [70] Hill R., Hopkins H.G. and Sewell M.J. (1982). Mechanics of solids 1st edition, Oxford: Pergamon Press Ltd.
- [71] Wang J., Li J., Yip S., Phillpot S.R. and Wolf D. (1995). Mechanical instabilities of homogeneous crystals. *Physical Review B*, 52, 12627-12635.
- [72] Barron T.H.K. and Klein M.L. (1965). Second-order elastic constants of a solid under stress. *Proceedings of the Physical Society*, 85, 523-532.
- [73] At-Amant A., Cornell W.D., Kollman P.A. and Halgren T.A. (1995). A study of geometries, conformational energies, dipole moments and electrostatic potential fitted charges using density functional theory. *Journal of Computational Chemistry*, 16, 1483-1506.
- [74] Chen X.Q., Niu H.Y., Li D.Z. and Li Y.Y. (2011). Modelling hardness of polycrystalline materials and bulk metallic glasses. *Intermetallics*, 19, 1275-1281.
- [75] Wu Z., Chen X.J., Struzhkin V.V. and Cohen R.E. (2005). Trends in elasticity and electronic structure of transition metal nitrides and carbides from first principles. *Physical Review B*, 71, 1-5.
- [76] Kittel C. (1976). Introduction to solid state physics 5th edition. New York: John Wiley & Sons.

- [77] Cohen M.L. (1985). Calculation of bulk Moduli of diamond and zinc-blende solids. *Physical Review B*, 32, 7988-7991.
- [78] Pugh S.F. (1954). Relationship between the elastic moduli and the plastic properties of a polycrystalline pure metals. *Philosophical Magazine*, 45, 823-843.
- [79] Saxe P. and Le Page Y. (2011). Ab-initio vs literature stiffness values for Ga: a caveat about crystal settings. *Physica B*, 191, 57-63.
- [80] Kamran S., Chen K. and Chen L. (2009). Ab-initio examination of ductility features of fcc metals. *Physical Review B*, 79, 379-393.
- [81] Mehl M.J., Klein B.M. and Papaconstantopoulos D.A. (1994). Intermetallic compounds, principles. Edited by Westbrook J.H. and Fleischer R.L. 1, John Wiley & Sons Ltd.
- [82] Goumri-Said S. and Kanoun M.B. (2007). Theoretical investigations of structural, elastic, electronic and thermal properties of Damiaoite PtIn₂. *Computational Materials Science*, 43, 243-250.
- [83] Mayer B., Anton H., Bott E., Methfessel M., Sticht J. and Schmidt P.C. (2003). Ab-initio calculation of the elastic constants and thermal expansion coefficients of laves phases. *Intermetallics*, 11, 23-32.
- [84] Bao G., Duan D., Zhou D., Jin X., Liu B. and Cui T. (2010). Structural, electronic and optical properties of crystalline iodoform under high pressure: A first-principles study. *Journal of Physical Chemistry B*, 114, 3999-4004.
- [85] Kaner R.B., Gilman J.J. and Tolbert S.H. (2005). Designing superhard materials. *Science*, 308, 1268-1269.
- [86] Hill R. (1952). The elastic behavior of a crystalline aggregate. *Proceedings of the Physical Society*, 65, 349-364.
- [87] Mattsson A.E., Schultz P.A., Desjarlais M.P., Mattsson T.R. and Leung K. (2005). Designing meaningful density functional theory calculations in material science, modelling simulation. *Materials Science and Engineering*, 13, 1-31.

- [88] Tvergaard V. and Hutchinson J.W. (1988). Microcracking in ceramics induced by thermal expansion or elastic anisotropy. *Journal of the American Chemical Society*, 71, 157-165.
- [89] Perdew J.P. and Zunger A. (1981). Self-interaction correction to density-functional approximations for many-electron systems. *Physical Review B*, 23, 5048-5079.
- [90] Blundell S.J. and Blundell K.M. (2010). Concepts in thermal physics, 2nd edition, New York: Oxford University Press.
- [91] Kittel C. (2004). Introduction to solid-state physics, 8th edition, New York. Wiley.
- [92] Pierce F.S., Basov D.N., Volkov P., Poon S.J. and Timusk T. (1994). Optical conductivity of insulating Al-based alloys: Comparison of quasiperiodic and periodic systems. *Physical Review Letters*, 73, 1865-1868.
- [93] Matsuda A., Sugita S., Fujii T. and Watanabe T. (2001). Study of pseudogap phenomena by STM and other probes. *Journal of Physics and Chemistry of Solids*, 62, 65-68.
- [94] Gornostyrev Y.N., Kontsevoi O.Y., Maksyutov A.F., Freeman A.J., Katsnelson M.I., Trefilo, A.V. and Lichtenstein A.I. (2004). Negative yield stress temperature anomaly and structural instability of Pt₃Al. *Physical Review B*, 70, 014102-1-014102-5.
- [95] Pankhurst D.A., Nguyen-Manh D. and Pettifor D.G. (2004). Electronic origin of structural trends across early transition-metal disilicides: Anomalous behaviour of CrSi₂. *Physical Review B*, 69, 075113-1-075113-8.
- [96] Bader R. (1990). Atoms in molecules: A quantum theory. New York: Oxford University Press.
- [97] Proft F.D., Alsenoy C.V., Peeters A., Langenaeker W. and Geerlings P. (2002). Atomic charges, dipole moments and Fukui functions using the Hirshfeld partitioning of the electron density. *Computational Journal of Chemistry*, 23, 1198-1209.
- [98] Popelier P.L.A. (2001). A fast algorithm to compute atomic charges based on the topology of the electron density. *Theoretical Chemistry Accounts*, 105, 393-399.

- [99] Popelier P.L.A. (1998). MORPHY98, a program written by P.L.A. Popelier with a contribution from R.G.A. Bone. UMIST, Manchester, England.
- [100] Stefanov B.B. and Cioslowski J. (1995). An efficient approach to calculation of zero-flux atomic surfaces and generation of atomic integration data. *Journal of Computational Chemistry*, 16, 1394-1404.
- [101] Popelier P.L.A. (1994). An analytical expression for interatomic surfaces in the theory of atoms in molecules. *Theoretical Chemistry Accounts*, 87, 465-476.
- [102] Malcolm N.O.J. and Popelier P.L.A. (2003). An improved algorithm to locate critical points in a 3D scalar field as implemented in the program MORPHY. *Journal of Computational Chemistry*, 24, 437-442.
- [103] Noury S., Krokidis X., Fuster F. and Silvi B. (1997). Computational tools for the electron localization function topological analysis. *Computers and Chemistry*, 23, 597-604.
- [104] Silvi B. and Gatti C. (2000). Direct space representation of the metallic bond. *Journal of Physics and Chemistry A*, 104, 947-953.
- [105] Henkelman G., Arnaldsson A. and Jonsson H. (2006). A fast and robust algorithm for Bader decomposition of charge density. *Computational Materials Science*, 36, 354-360.
- [106] Sanville E., Kenny S.D., Smith R. and Henkelman G. (2009). Improved grid-based algorithm for Bader charge allocation. *Journal Computational Chemistry*, 28, 899-908.
- [107] Tang W., Sanville E. and Henkelman G. (2009). A grid-based Bader analysis algorithm without lattice bias. *Journal of Physics: Condensed Matter*, 21, 1-7.
- [108] Waterson C.N., Tasker P.A. and Morrison C.A. (2015). Design, synthesis and testing of reagents for high-value mineral collection. The University of Edinburgh, Edinburgh.
- [109] Gibbs J.W. (1928). The collected works of J. Willard Gibbs. Longmans.
- [110] Joannopoulos D.J. and Cohen M.L. (1973). Special points in the Brillouin zone. *Physical Review B*, 8, 5747-5757.

- [111] Joannopoulos J.D. and Cohen M.L. (1973). Electronic charge densities for ZnS in the wurtzite and zincblende structures. *Journal of Physics C*, 6, 1572-1585.
- [112] Ngoepe P.E., Ntoahae P.S., Mangwejane S.S., Sithole H.M., Partker S.C., Wright K.V. and de Leeuw N.H. (2005). Atomistic simulation studies of iron sulphide, platinum antimonide and platinum arsenide. *Journal of Science*, 101, 480-483.
- [113] Olowolafe J.O., Ho P.S., Hovel H.J., Lewis J.E. and Woodall J.M. (1979). Contact reactions in Pd/GaAs junctions. *Journal of Applied Physics*, 50, 955-962.
- [114] Born M. and Huang K. (1956). Theory of crystal lattices. Oxford: Clarendon.
- [115] Ravindran P., Fast L., Korzhavyi P.A. and Johansson B. (1998). Density functional theory for calculations of elastic properties of orthorombic crystals: Application to TiSi₂. *Journal of Applied Physics*, 84, 4891-4904.
- [116] Hao X., Xu Y., Wu Z., Zhou D., Liu X. and Meng J. (2008). Elastic anisotropy of OsB₂ and RuB₂ from first-principles study. *Journal of Alloys and Compounds*, 453, 413-417.
- [117] Peng F., Peng W.M., Fu H.Z. and Yang X.D. (2009). Elasticity and thermodynamic properties of RuB₂ under pressure. *Physica B*, 404, 3363-3367.
- [118] Yildirim A., Koc H. and Deligoz E. (2012). First principles-study of the structural, elastic, electronic, optical and vibrational properties of intermetallic Pd₂Ga. *Chinese Physics B*, 21, 037101-1-037101-8.
- [119] Parlinski K., Li Z.Q. and Kawazoe Y. (1997). First-principles determination of the soft mode in cubic ZrO₂. *Physical Reviews Letters*, 78, 4063-4066.
- [120] Ntoahae P.S., Pettifor D.G. and Ngoepe P.E. (2005). Application of computer simulation methods to the study of platinum group minerals. University of Limpopo, Polokwane.
- [121] Boettger J.C. (1994). Non-convergence of surface energies obtained from thin-film calculations. *Physical Review B*, 49, 16798-16800.

[122] Watson G.W., Kesley E.T., de Leeuw N.H., Harris D.J and Parker S.C. (1996). Atomistic simulation of dislocations, surfaces and interfaces in MgO. *Journal of the Chemical Society-Faraday Transactions*, 92, 433-438.

Appendix A: Explanation data of the project

- Project – Computational modelling studies of PtAs₂, PtAsS and Pd₂As minerals and their stability done from structural, thermodynamic, elastic, mechanical, vibrational, electronic and surface properties.
- DFT (VASP) – Density functional theory method implemented in Vienna *Ab-initio* Simulation Package (VASP) code used to study all the properties for PtAs₂, PtAsS (CE) and Pd₂As structures.
- DFT (CASTEP) – Density functional theory method implemented in Cambridge Serial Total Energy Package (CASTEP) code used to study all the properties for PtAsS (VCA) structure.
- Bulk structures – PtAs₂, PtAsS and Pd₂As bulk structures were used to study and investigate structural, thermodynamic, elastic, mechanical, vibrational, electronic and surface properties.
- The cluster expansion used to investigate and generate new stable PtAsS systems. The bulk structures PtAs₂, PtAsS and Pd₂As were used to study the low Miller index (100), (110) and (111).
- Low Miller index surfaces – The investigation of the studied surfaces are done from testing different terminations, convergence of surface layers and slabs and creation of supercell structures. Their electronic structures were presented for all the three surfaces.

Appendix B: Tables

Table B1.1 – B1.4 shows the atomic position (X, Y, Z) for the systems PtAs₂, PtAsS (CE), PtAsS (VCA) and Pd₂As. Table B1.5 showed 102 stable structures generated by cluster expansion.

Table B1.1: The atomic positions (Wyckoff notation) in sperrylite (PtAs₂) crystal structure [66].

Property		Value		
Formula		PtAs ₂		
Z		4		
Unit cell length (a=b=c)		5.967 Å		
Cell angles ($\alpha=\beta=\gamma$)		90°		
Space-group		Pa-3 (#205)		
Atoms	Position	X	Y	Z
Pt1	(4a)	0.000	0.000	0.000
As1	(8c)	0.383	0.383	0.383

Pt1 denote the octahedral M(O) and As1 denote the arsenic forming dimer.

Table B1.2: The atomic positions (Wyckoff notation) in platarsite (PtAsS) CE structure [66].

Property		Value		
Formula		PtAsS		
Z		4		
Unit cell length (a=b=c)		5.428 Å		
Cell angles ($\alpha=\beta=\gamma$)		90°		
Space-group		Pa-3 (#205)		
Atoms	Position	X	Y	Z
Pt1	(1a)	0.000	0.000	0.000
Pt2	(1a)	0.500	0.000	0.500
Pt3	(1a)	0.000	0.500	0.500
Pt4	(1a)	0.500	0.500	0.500
As1	(1a)	0.385	0.385	0.385
As2	(1a)	0.115	0.615	0.885
As3	(1a)	0.385	0.115	0.885
As4	(1a)	0.115	0.885	0.385
S1	(1a)	0.615	0.885	0.115
S2	(1a)	0.885	0.115	0.615
S3	(1a)	0.615	0.615	0.615
S4	(1a)	0.885	0.385	0.115

Table B1.3: The atomic positions (Wyckoff notation) in platarsite (PtAsS) VCA structure [66].

Property		Value		
Formula		PtAsS		
Z		4		
Unit cell length (a=b=c)		5.428 Å		
Cell angles ($\alpha=\beta=\gamma$)		90°		
Space-group		Pa-3 (#205)		
Atoms	Position	X	Y	Z
Pt1	(1a)	0.000	0.000	0.000
Pt2	(1a)	0.500	0.000	0.500
Pt3	(1a)	0.000	0.500	0.500
Pt4	(1a)	0.500	0.500	0.500
As1/S1	(1a)	0.385	0.385	0.385
As2/S2	(1a)	0.115	0.615	0.885
As3/S3	(1a)	0.385	0.115	0.885
As4/S4	(1a)	0.115	0.885	0.385
As5/S5	(1a)	0.615	0.885	0.115
As6/S6	(1a)	0.885	0.115	0.615
As7/S7	(1a)	0.615	0.615	0.615
As8/S8	(1a)	0.885	0.385	0.115

Pt1, Pt2, Pt3 and Pt4 denote the octahedral M(O) and tetrahedral M(T), respectively and As1/S1, As2/S2, As3/S3, As4/S4, As5/S5, As6/S6, As7/S7 and As8/S8 denote the dimers and linked arsenic/sulphurs, respectively.

Table B1.4: The atomic positions (Wyckoff notation) in palladoarsenide (Pd_2As) crystal structure [66].

Property		Value		
Formula		Pd_2As		
Z		3		
Unit cell length (a=b) (c)		6.650 and 3.583 Å		
Cell angles ($\alpha=\beta$) (γ)		90° and 120°		
Space-group		P-62m (#189)		
Atoms	Position	X	Y	Z
Pd1	(3g)	0.257	0.000	0.500
Pd2	(3f)	0.595	0.000	0.000
As1	(2d)	0.333	0.667	0.500
As2	(1a)	0.000	0.000	0.000

Pd1 denote the octahedral M(O), Pd2 denote tetrahedral M(T), respectively and As1 denote the face-capping As(*f*), As2 denote linked As(*l*) arsenic, respectively.

Table B1.5: The ground state enthalpies of formation as derived by DFT and CE in eV/atom at the final iteration for Pt-S system.

Comparison of energies E and formation energies DHF in eV (counted per active atom position) as predicted by the cluster expansion (CE) and as calculated by the computational engine (DFT). Energy differences to the structure at the ground state line (GSL) for each composition x are listed.

# no.	x(1:k,1:nC)	E_DFT	D(E_DFT,E_CE)	E_CE	DHF_DFT	DHF_CE	Dist to GSL DFT	title	cell formula	space group
1	0.00000	1.00000	-7.2195495000	0.0000001000	-7.2195494000	0.0000000000	0.0000000000	ce22	Pt4S8	Pa-3
2	0.04167	0.95833	-7.2818900000	-0.0004879703	-7.2823779703	-0.0092971979	-0.0097852598	ce3045133	Pt12As523	P1
3	0.04167	0.95833	-7.2824452917	-0.0003880429	-7.282833346	-0.0098524896	-0.0102406241	ce711426	Pt12As523	P1
4	0.06250	0.93750	-7.3137890625	-0.0002130477	-7.3140021102	-0.0146746094	-0.0148877446	ce9836	Pt8As515	R3
5	0.06250	0.93750	-7.3140040000	-0.0004713018	-7.3144753018	-0.0148895469	-0.0153609362	ce4252	Pt8As515	P1
6	0.08333	0.91667	-7.3464324167	0.0014332556	-7.3449991610	-0.0207963125	-0.0193631402	ce710142	Pt12As2522	P2_1
7	0.12500	0.87500	-7.4099841875	0.0001171539	-7.4098670336	-0.0313047812	-0.0311877023	ce4228	Pt8As2514	P2_1
8	0.12500	0.87500	-7.4108664167	-0.0007290814	-7.4107954980	-0.0313870104	-0.0321161668	ce710136	Pt12As3521	P1
9	0.16667	0.83333	-7.4726341250	-0.0005315705	-7.4731656955	-0.0409114167	-0.0414430538	ce711351	Pt12As4520	P1
10	0.16667	0.83333	-7.4735178333	-0.0010574229	-7.4724604104	-0.0417951250	-0.0407377687	ce2050374	Pt12As4520	P2_1
11	0.16667	0.83333	-7.4746892917	-0.0008289205	-7.4755182121	-0.0429665833	-0.0437955785	ce711387	Pt12As4520	P1
12	0.16667	0.83333	-7.4751515000	-0.0016151606	-7.4767666066	-0.0434287917	-0.0450440189	ce711321	Pt12As4520	Pca2_1
13	0.18750	0.81250	-7.5053398750	0.0006956585	-7.5046433065	-0.0470955156	-0.0463990096	ce8399	Pt8As3513	P1
14	0.18750	0.81250	-7.5055135000	0.0009313885	-7.5045821115	-0.0472691406	-0.0463378146	ce4227	Pt8As3513	P1
15	0.18750	0.81250	-7.5059788125	-0.0006356506	-7.5066153731	-0.0477344531	-0.0483710763	ce4149	Pt8As3513	P1
16	0.18750	0.81250	-7.5059958125	-0.0004384890	-7.5064343015	-0.0477514531	-0.0481900047	ce4199	Pt8As3513	P1
17	0.20833	0.79167	-7.5251830000	-0.0005078682	-7.5256908682	-0.0440169896	-0.0409249161	ce3035143	Pt12As5519	P3
18	0.20833	0.79167	-7.5388504167	0.0019568939	-7.5368935227	-0.0540844063	-0.0521275706	ce3024686	Pt12As5519	P1
19	0.20833	0.79167	-7.5391272917	-0.0005726967	-7.5396998884	-0.0543612813	-0.0549340363	ce632546	Pt12As5519	P1
20	0.20833	0.79167	-7.5392535000	-0.0030762550	-7.5423297550	-0.0544874896	-0.0575638030	ce090731875	Pt12As5519	P1
21	0.20833	0.79167	-7.5393286667	-0.0006050181	-7.5399336847	-0.0546265652	-0.0551677327	ce089808208	Pt12As5519	P1
22	0.25000	0.75000	-7.6006174375	-0.000010569	-7.6006184944	-0.0548081250	-0.0528092319	ce8374	Pt8As512	Cc
23	0.25000	0.75000	-7.6014530000	0.0008909943	-7.6023439943	-0.0636436875	-0.0645347318	ce1479445	Pt12As6518	P2_1
24	0.25000	0.75000	-7.6034040000	-0.0001718545	-7.6037585845	-0.0655946875	-0.0657665920	ce0106781250	Pt12As6518	P1
25	0.25000	0.75000	-7.6039892917	0.0002283810	-7.6037609107	-0.0661799792	-0.0659916482	ce1827040	Pt12As6518	P1
26	0.25000	0.75000	-7.6048011667	0.0012925903	-7.6035085764	-0.0669918542	-0.0656993133	ce3030270	Pt12As6518	P1
27	0.25000	0.75000	-7.6053523333	-0.0011733468	-7.6065256801	-0.0675430208	-0.0687164176	ce515932	Pt12As6518	P2_1
28	0.25000	0.75000	-7.6064850000	-0.0001113311	-7.6065963311	-0.0676785675	-0.0687870686	ce4224	Pt8As512	Pca2_1
29	0.29167	0.70833	-7.6488725417	0.0002786936	-7.6485938481	-0.0580192921	-0.0577412752	ce010853	Pt12As7517	P1
30	0.29167	0.70833	-7.6564092917	-0.0001605234	-7.6565698151	-0.0565566771	-0.0571724222	ce3035270	Pt12As7517	P3
31	0.29167	0.70833	-7.6704909167	0.0010680090	-7.6694229076	-0.0796383021	-0.0785703347	ce461214	Pt12As7517	P1
32	0.29167	0.70833	-7.6711899583	-0.0008906489	-7.6720806072	-0.0803373438	-0.0812280343	ce414774	Pt12As7517	P1
33	0.29167	0.70833	-7.6713277917	-0.0012682977	-7.6725968093	-0.0804751771	-0.0817435164	ce0085097708	Pt12As7517	P1
34	0.29167	0.70833	-7.6715570833	0.0005515786	-7.6710055047	-0.0807044688	-0.0801529318	ce0082804792	Pt12As7517	P1
35	0.31250	0.68750	-7.6927493750	-0.0002789559	-7.6930283309	-0.0753751094	-0.0756541028	ce6413	Pt8As5511	P1
36	0.31250	0.68750	-7.7022582500	-0.0004963789	-7.7027546289	-0.0848398444	-0.0853804008	ce3404	Pt8As5511	P1
37	0.31250	0.68750	-7.7028081875	-0.0002105640	-7.7030907515	-0.0855059219	-0.0857165234	ce2556	Pt8As5511	P1
38	0.31250	0.68750	-7.7039828750	0.0017640480	-7.7022188270	-0.0866860994	-0.0848445988	ce6234	Pt8As5511	P1
39	0.31250	0.68750	-7.7053460000	0.0010496391	-7.7042963609	-0.0879171344	-0.0869221327	ce917	Pt8As5511	P1
40	0.31250	0.68750	-7.7056460000	0.0008394332	-7.7048065668	-0.0882717344	-0.0874323387	ce2868	Pt8As5511	P1
41	0.33333	0.66667	-7.7351210000	0.0006687763	-7.7344522237	-0.0912250833	-0.0905563404	ce695233	Pt12As8516	P3
42	0.33333	0.66667	-7.7356230833	0.0000115733	-7.7356115100	-0.0917271667	-0.0917156267	ce2693643	Pt12As8516	Pc
43	0.33333	0.66667	-7.7359133333	-0.0012207733	-7.7371341066	-0.0920174167	-0.0932382233	ce526834	Pt12As8516	P1
44	0.37500	0.62500	-7.7950869717	0.0004719450	-7.7946148467	-0.0981475729	-0.0976756530	ce651526	Pt12As9515	P1
45	0.37500	0.62500	-7.8020210833	0.0008525222	-7.8019358312	-0.1050818646	-0.1049966374	ce463520	Pt12As9515	P1
46	0.37500	0.62500	-7.8048905833	0.0004484243	-7.8044421590	-0.1079513646	-0.1075029652	ce166686	Pt12As9515	P1
47	0.41667	0.58333	-7.8714133333	-0.0023572224	-7.8734985557	-0.1211588125	-0.1235160515	ce1646419	Pt12As10514	P2_1
48	0.41667	0.58333	-7.8721121250	-0.0005758349	-7.8726696959	-0.1221386042	-0.1227144557	ce183805	Pt12As10514	P1
49	0.41667	0.58333	-7.8725077083	0.0004281013	-7.8720796070	-0.1225251875	-0.1220971028	ce23863	Pt12As10514	P2_1
50	0.43750	0.56250	-7.880670625	-0.0005417036	-7.8812187661	-0.1041728906	-0.1047146067	ce6750	Pt8As759	P1
51	0.43750	0.56250	-7.9043411875	-0.0000131067	-7.9043542942	-0.1278370156	-0.1278501348	ce428	Pt8As759	P1
52	0.43750	0.56250	-7.9061260625	-0.0001851288	-7.9063111913	-0.1296218906	-0.1298070319	ce3312	Pt8As759	P1
53	0.45833	0.54167	-7.8757952500	-0.0005480953	-7.8763437203	-0.0727690021	-0.0733179058	ce382778	Pt12As11513	P1
54	0.45833	0.54167	-7.8788722917	0.0006264563	-7.8782458354	-0.0752464688	-0.0752002088	ce1675835	Pt12As11513	P1
55	0.45833	0.54167	-7.9400905833	0.0000817301	-7.9399278532	-0.1369837604	-0.1369020386	ce14304	Pt12As11513	P1
56	0.45833	0.54167	-7.9401997083	-0.0001429932	-7.9403427016	-0.1371738854	-0.1373168870	ce2113765	Pt12As11513	P3
57	0.50000	0.50000	-7.8644284583	0.0003568390	-7.8640716193	-0.0083593333	-0.0080024943	ce1859586	Pt12As12512	P1
58	0.50000	0.50000	-7.9245919583	-0.0003658082	-7.9249577666	-0.0685228333	-0.0688864616	ce179212917	Pt12As12512	P1
59	0.50000	0.50000	-8.0086147500	0.0014535729	-8.0071611717	-0.1525456250	-0.1510920521	ce5	Pt4As454	P2_13
60	0.54167	0.45833	-8.0058662083	0.0005587725	-8.0053074359	-0.0967537813	-0.0961950004	ce25726	Pt12As13511	P1
61	0.54167	0.45833	-8.0066937917	0.0000682155	-8.0062652571	-0.0975813646	-0.0975131407	ce2698233	Pt12As13511	P1
62	0.54167	0.45833	-8.0077997083	0.0004361615	-8.0073635468	-0.0986872813	-0.0982511114	ce2902869	Pt12As13511	P1
63	0.54167	0.45833	-8.0449187333	0.0014066192	-8.0435112142	-0.1358054063	-0.1343987787	ce10211	Pt12As13511	P1
64	0.56250	0.43750	-8.0628200000	0.0011422673	-8.0616862327	-0.1271944219	-0.1260521420	ce58	Pt8As957	P1
65	0.58333	0.41667	-8.0644758750	0.0003780978	-8.0637377772	-0.1023201458	-0.1015820314	ce596364	Pt12As14510	Pc
66	0.58333	0.41667	-8.0753976667	0.0004019379	-8.0749957288	-0.1132419375	-0.1128399830	ce632877	Pt12As14510	P2_1
67	0.58333	0.41667	-8.0826825000	0.0004412152	-8.0822470348	-0.1205325208	-0.1200912890	ce10191	Pt12As14510	P1
68	0.58333	0.41667	-8.0827508333	0.0007010615	-8.0820497719	-0.1205951042	-0.1198940260	ce10206	Pt12As14510	P1
69	0.62500	0.37500	-8.1184884583	0.0008701948	-8.1176182635	-0.1032894271	-0.1024192073	ce21737	Pt12As1559	P1
70	0.62500	0.37500	-8.1191102917	-0.00024004971	-8.1215107888	-0.1039112604	-0.1063117325	ce11964	Pt12As1559	P1
71	0.62500	0.37500	-8.1207883750	0.0004420974	-8.1203462776	-0.1055893438	-0.1051472213	ce18090	Pt12As1559	P1
72	0.62500	0.37500	-8.1214421667	0.0001146104	-8.1213275563	-0.1062431354	-0.1061285900	ce10190	Pt12As1559	P1
73	0.62500	0.37500	-8.1218550417	-0.0009320592	-8.1227871009	-0.1066560194	-0.1075880446	ce10185	Pt12As1559	P1
74	0.66667	0.33333	-8.13570876250	-0.0011052301	-8.1358192851	-0.0888452917	-0.0899504884	ce723456	Pt12As1658	P2_1
75	0.66667	0.33333	-8.1614598750	-0.0006878071	-8.1621476821	-0.0932175417	-0.0939053154	ce102454811	Pt12As1658	P1
76	0.66667	0.33333	-8.1632689583	0.0003945699	-8.1636635282	-0.0950266250	-0.0954211616	ce632866	Pt12As1658	Pca
77	0.66667	0.33333	-8.1640755417	0.0015960942	-8.1624794475	-0.0958332083	-0.0942370808	ce270550	Pt12As1658	Pca2_1
78	0.68750	0.31250	-8.1777967500	-0.0006292317	-8.1784259817	-0.0830276556	-0.0836619898	ce4732	Pt8As1155	P1
79	0.70833	0.29167	-8.1980549167	-0.0006685614	-8.1987234781	-0.0767692813	-0.0774370510	ce749344	Pt12As1757	P1
80	0.70833	0.29167	-8.1994652917	0.0006382031	-8.1988270885	-0.0781796563	-0.077541			

Appendix C: Papers presented at conferences

1. University of Limpopo Faculty of Science and Agriculture (FSA) post-graduate research day held at Fusion Boutique in Polokwane (2018) “Investigation of the structural, elastic, mechanical and electronic properties of PtAs₂, PtAsS and Pd₂As minerals”.
2. Centre for High Performance Computing (CHPC) conference held at Century City Hotel in Cape Town (2018) “*Ab-initio* study of the structural, mechanical and electronic properties of PtAs₂, PtAsS and Pd₂As minerals”.
3. South African Institute of Physics (SAIP) conference held at Protea Hotel Ranch Resort (2019) “*Ab-initio* studies of sperrylite, platarsite and palladoarsenide phase stability and surfaces”.
4. University of Limpopo Faculty of Science and Agriculture (FSA) post-graduate research day held at Protea Hotel Ranch Resort (2019) “First-principle study of hydroxide and new novel collector adsorptions on sperrylite (100) surface”.